Spatio-temporal study of glacier mass balance using observations and modeling in the Chandra Basin, Western Himalaya

A Thesis submitted in partial fulfilment for the Degree of

DOCTOR OF PHILOSOPHY

IN THE SCHOOL OF EARTH, OCEAN, AND ATMOSPHERIC SCIENCES

GOA UNIVERSITY

By

SUNIL NAMDEV OULKAR

National Centre for Polar and Ocean Research
Headland Sada, Vasco da Gama,
Goa, India-403804

November 2024

DECLARATION

I, Sunil Namdev Oulkar, hereby declare that this thesis represents work which has been carried out by me and that it has not been submitted, either in part or full, to any other University or Institution for the award of any research degree.

Place: Goa University

Date: 19/11/2024

Sunil Namdev Oulkar

CERTIFICATE

I/we hereby certify that the above Declaration of the candidate, Sunil Namdev Oulkar is true and the work was carried out under my/our supervision.

Dr. Thamban Meloth
Research Supervisor:
Director
National Centre for Polar & Ocean Research
Vasco-da-Gama, Goa 403 804

R. Rengarajan 19/11/2024
Examiner

डॉ. एम. रविचंद्रन / Dr. M. Ravichandran
सचिव / Secretary
भारत सरकार / Government of India
पृथ्वी विज्ञान मंत्रालय / Ministry of Earth Sciences
पृथ्वी भवन, लोधी रोड, नई दिल्ली–110003
Prithvi Bhawan, Lodhi Road, New Delhi-110003

Dr. M. Ravichandran
Research co-supervisor
Secretary
Ministry of Earth Sciences, Government of India,
Prithvi Bhawan, Lodhi Road, New Delhi 110003

ACKNOWLEDGMENTS

First and foremost, I would like to thank my supervisor, **Dr. Thamban Meloth**, Director, National Centre for Polar and Ocean Research (NCPOR), for his guidance, support, and faith in me throughout my PhD research. I would also like to thank my co-supervisor, former Director of NCPOR, **Dr. M. Ravichandran,** Secretary, Ministry of Earth Sciences (MoES), whose continuous guidance has been important during this journey. Thank you for the trust, ideas and the opportunity to work in such an excellent working environment both in NCPOR and the field in the Himalaya.

I want to extend gratitude to my DRC members **Dr. Parmanand Sharma**, NCPOR, and **Prof. Anthony A. Viegas**, Goa University, for their constructive comments and feedback that improved my scientific knowledge and skills. I would like to thank **Dr. Rahul Mohan**, Group Director, Polar Science Division, NCPOR, for his support and encouragement during this journey. I am greatly thankful to **Dr. Argha Banerjee,** Indian Institute of Science Education and Research (IISER), Pune for his suggestions in my research journey.

I acknowledge the **National Centre for Polar and Ocean Research** for providing academic and administrative support. **Ministry of Earth Sciences** (MoES), Government of India, sincerely acknowledged for funding through the project “PACER-Cryosphere and Climate”. On the same note, I would also like to thank the Dean and office members of the School of Earth, Ocean, and Atmospheric Sciences, Goa University, for their support during this period. My sincerest thanks to every member of the NCPOR family who helped my research directly or indirectly.

During the last years, many people supported me in their own way. I am thankful to **Dr. Bhanu Pratap** and **Dr. Ajit Singh** for introducing me to the nuts and bolts of glaciological research and being mentor/friends from day one. I thank my friends and colleagues, Vikram Goel, Sourav Laha, Lavkush Patel, Ankit Pramanik, Tariq Ejaz, Sourav Chatterjee, Subeesh M P, Aritri Sanyal, Kamini Meshram, Sibin Simon, Pallavi Choudhari, Gayathri Eledath, Alok Kumar Sinha, Ashutosh Acharya, Riya Naik, Trupti Naik, and Aniket Naik, for enriching discussions and great support throughout the years, without their friendship and support, life in the institute and the field would have been boring. I am grateful for all the helping hands in the Himalayas, especially all my friends from Nepal, without whom the logistic activities would not have been possible.

Finally, I would like to thank my parents, Shri Namdev and Smt. Shalan Oulkar and my siblings Sagar, Sangita and Sheetal who truly inspired me to follow my dreams. I am deeply grateful to my wife, Ankita, for her unwavering support and faith in me throughout this journey. Her encouragement has been instrumental to my accomplishments, and I could not have reached this point without her by my side. Also, I would like to thank all my teachers, mentors and rest of the family for their motivation and encouragement.

Sunil Namdev Oulkar

To my wife Ankita, for instilling faith in me

Abstract

Over the last few decades, elevation-dependent warming has become more prominent in the Himalayan region, contributing to increased warming trends and affecting regional climate and freshwater availability by impacting glacier ice and seasonal snow. However, there are significant knowledge gaps regarding glacier-atmosphere interactions, energy and mass balance processes in the data-scarce Himalaya. Therefore, this thesis is aimed to advance understanding of spatio-temporal variability in temperature lapse rate, surface energy balance and mass balance of glaciers in the Chandra Basin, western Himalaya, using an integrated approach combining in-situ observations and physically-based modeling.

The results reveal significant spatio-temporal variability in air temperature lapse rates, deviating from the standard environmental lapse rate, with implications for temperature extrapolation and glacio-hydrological modeling. Over the Chandra Basin, the estimated mean annual temperature lapse rate is 3.8 ± 0.3 °C km^{-1} with a strong seasonal variability. We found substantial seasonal variability in each temperature lapse rate time series. The maximum temperature lapse rate is 5.8 ± 0.2 °C km^{-1} during the summer, and the minimum is -1.6 ± 0.1 °C km^{-1} during winter, comparing all the meteorological stations. Further, we observe strong diurnal fluctuations of temperature lapse rate, which has maximum and minimum values during 10:00 to 18:00 hrs and 20:00 to 09:00 hrs, respectively. The study highlights that the temporal variability of temperature lapse rate is site-specific and strongly correlated with wind speed, relative humidity, and radiation fluxes. Furthermore, a temperature-index model is used to assess the implications of temperature lapse rate by estimating glacier mass balance. This study highlights the importance of considering observed temperature lapse rate to accurately model surface mass balance over the glacierised Himalayan region.

The surface energy and mass balance simulations for Sutri Dhaka Glacier show good agreement with field observations. The modeled energy flux showed that net shortwave radiation contributed 56% to the total surface energy fluxes, followed by net longwave radiation (27%), sensible heat (8%), latent heat (5%), and ground heat flux (4%). The model-derived Sutri Dhaka Glacier mean annual mass balances of -1.09 ± 0.31 and -0.62 ± 0.19 m w.e. for 2015/16 and 2016/17 are similar to the measured values of -1.16 ± 0.33 and -0.67 ± 0.33 m w.e., respectively. The sensitivity analysis shows that the mass balance is affected by air temperature (-0.21 m w.e. a^{-1} $°C^{-1}$) and precipitation (0.19 m w.e. a^{-1} $(10\%)^{-1}$) changes. This study suggests that, the mass balance of the Sutri Dhaka Glacier is less sensitive to changes in the partitioning of precipitation into snow and rain because the majority of precipitation falls as snow during the winter when the temperature is well below 0 °C.

The distributed mass balance analysis for the upper Chandra Basin glaciers indicates a negative mean annual mass balance of -0.51 ± 0.28 m w.e. a^{-1} for seven hydrological years from 2015 to 2022, with high sensitivity to both air temperature and precipitation variations. The study reveals that a 42% increase in precipitation is necessary to counteract the additional mass loss resulting from a 1 °C increase in air temperature for the glaciers. We find that the geographical settings like aspect, slope, size and elevation of the glacier contribute towards the spatial variability of mass balance within the selected region. This study provides valuable insights into the glacier-atmosphere interactions, energy fluxes, and mass balance dynamics of glaciers in the Western Himalaya region, contributing to a better understanding of the impacts of climate change.

Keywords: Air Temperature Lapse Rate; Energy Balance Modeling, Mass Balance, Climate Sensitivity, Chandra Basin, Western Himalaya

Table of Contents

List of Abbreviations and Acronyms

ELA	Equilibrium Line Altitude
A1	AWS at Himansh Base Camp
A2	AWS near Gepang Gath Glacier
A3	AWS near Samudra Tapu Glacier
A4	AWS at Sutri Dhaka Glacier
A5	AWS near Baralacha Pass
AAR	Accumulation Area Ratio
ASTER	Advanced Spaceborne Thermal Emission and Reflection Radiometer
AWS	Automatic Weather Station
COSIMA	COupled Snowpack and Ice surface energy and MAss balance
COSIPY	COupled Snowpack and Ice surface energy and mass balance model in Python
DDF	Degree-Day Factor
DEM	Digital Elevation Model
ECMWF	European Centre for Medium-Range Weather Forecasts
EDW	Elevation-Dependent Warming
ERA	European Reanalysis
ERSDAC	Earth Remote Sensing Data Analysis Centre

GDEM	Global Digital Elevation Model
GPR	Ground Penetrating Radar
GPS	Global Positioning System
IISER	Indian Institute of Science Education and Research
ISM	Indian Summer Monsoon
MoES	Ministry of Earth Sciences
NCPOR	National Centre for Polar and Ocean Research
RMSE	Root Mean Square Error
TLR	Temperature Lapse Rate
WD	Western Disturbance
WGMS	World Glacier Monitoring Service

List of Figures

List of Tables

Chapter 1

1 Introduction

1.1 Overview

The cryosphere is the part of Earth system where water is in the frozen form. It comprises of snow, ice, glaciers, ice caps, ice sheets, ice shelves, icebergs, lake ice, river ice, sea ice, permafrost, frozen ground, etc. The cryosphere is one of the crucial components of the climate system, containing a majority of the planet's freshwater (Cuffey and Paterson 2010). It influences energy budget, moisture fluxes, clouds cover, precipitation, hydrology, atmosphere and global circulation (Cuffey and Paterson 2010). Glaciers account for a small fraction of the total ice volume of all the cryosphere components, but serve as a sensitive indicator of climate change on different timescales spanning from diurnal to muti-decadal (Oerlemans 2005; Benn and Evans 2010). Also, they are essential elements of landscape and environment in high mountain and polar regions. Despite their relatively small size, glaciers profoundly impact global sea levels, regional water resources, geomorphology, agriculture, industries and natural hazards (Meier et al. 2007; Biemans et al. 2019; Zemp et al. 2019; Immerzeel etss al. 2020; Hugonnet et al. 2021; Ravindra et al. 2024). Therefore, studying glacier evolution is crucial for understanding climate change impacts and mitigating water resource challenges in glacier-fed river basins (HockRasul et al. 2019; Rasul and Molden 2019; Ravindra et al. 2024). However, only a small fraction of the world's glaciers have been studied through ground observations (Mayewski et al. 2020). The existing in-situ glacier observations hold significant potential for enhancing our knowledge of glacier dynamics, validating remote sensing data, and facilitating the development of more precise models predicting glacier responses to climate change. Despite the availability of data, challenges remain in representing glacio-hydrological processes due to remoteness and non-availability of long-term in-situ data (Figure 1.1) (Azam et al. 2021; Vishwakarma et al. 2022). Improved monitoring is therefore needed to understand better linkages between glaciers and other earth system components across spatio-temporal scales. This will support more accurate predictions of cryospheric changes and their diverse impacts.

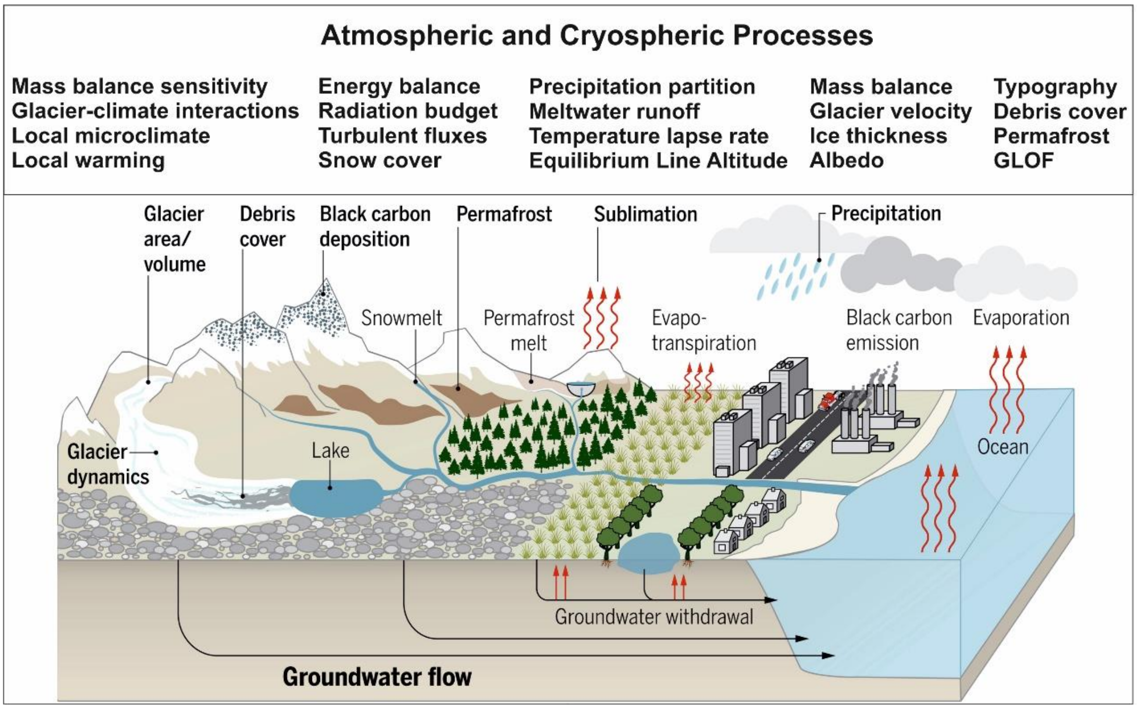

Figure 1.1. A schematic representation of the hydrological cycle, atmospheric and cryospheric processes and major challenges in the field of glacio-hydrology. Adapted from Azam et al. (2021) and Vishwakarma et al. (2022).

1.2 Scientific background

1.2.1 Glaciers

Glaciers are large masses of ice that slowly moves down the mountains or valleys. They are formed from snow that builds up year after year and is compressed into ice over time (Cuffey and Paterson 2010). As more snow falls and compresses, the glacier mass grows and flows downhill due to their own weight and gravity, shaping landscapes as they flow downslope along the slope of the terrain. The rate of glacier ice formation from the snowpack is dependent on climatic and non-climatic factors. The climatic factors are temperature, precipitation, wind, relative humidity, radiations, pressure and cloud cover among others. The non-climatic factors are snow crystal structure, melt-freeze cycles, topography (slope, aspect, elevation), dynamics, shading effects from surrounding terrain, debris cover, avalanche, geothermal heat flux, surface characteristics etc. Climatic factors primarily control the accumulation and melting processes, while non-climatic factors can modulate the energy budget and metamorphism of the snowpack, influencing its transformation into glacier ice. The balance between accumulation and melting of snow/ice defines the mass balance of a glacier.

1.2.2 Glacier surface mass balance

Mass balance is a measure of a glacier state, representing the difference between the mass gained through accumulation processes and the mass lost through ablation processes over a specific time period, generally in a hydrological year (Cogley et al. 2011). The area of a glacier can be separated into two distinct zones: the accumulation zone where mass is gained, and the ablation zone where mass is lost. The accumulation zone receives mass through snowfall, avalanches, and wind-blown snow, among other smaller factors (Figure 1.2). The ablation zone loses mass through surface melt, subsurface melt, sublimation, surface meltwater runoff, evaporation, calving, among other processes (Figure 1.2). If a glacier loses mass more than it gains, it will have a negative mass balance, causing the glacier to retreat and thinning. Conversely, if a glacier gains more mass than it loses, it will have a positive mass balance, leading the glacier to advance or grow larger. The altitude where the losses from ablation are balanced by the gains from accumulation, resulting in zero net mass balance, is known as the Equilibrium Line Altitude (ELA). Mass balance is determined by the interplay of accumulation and ablation processes, which are influenced by various components of the Earth system, such as the atmosphere, ocean, rivers, and surface characteristics, among others. The meltwater from glaciers contributes to river runoff and sea level rise (Benn and Evans 2010).

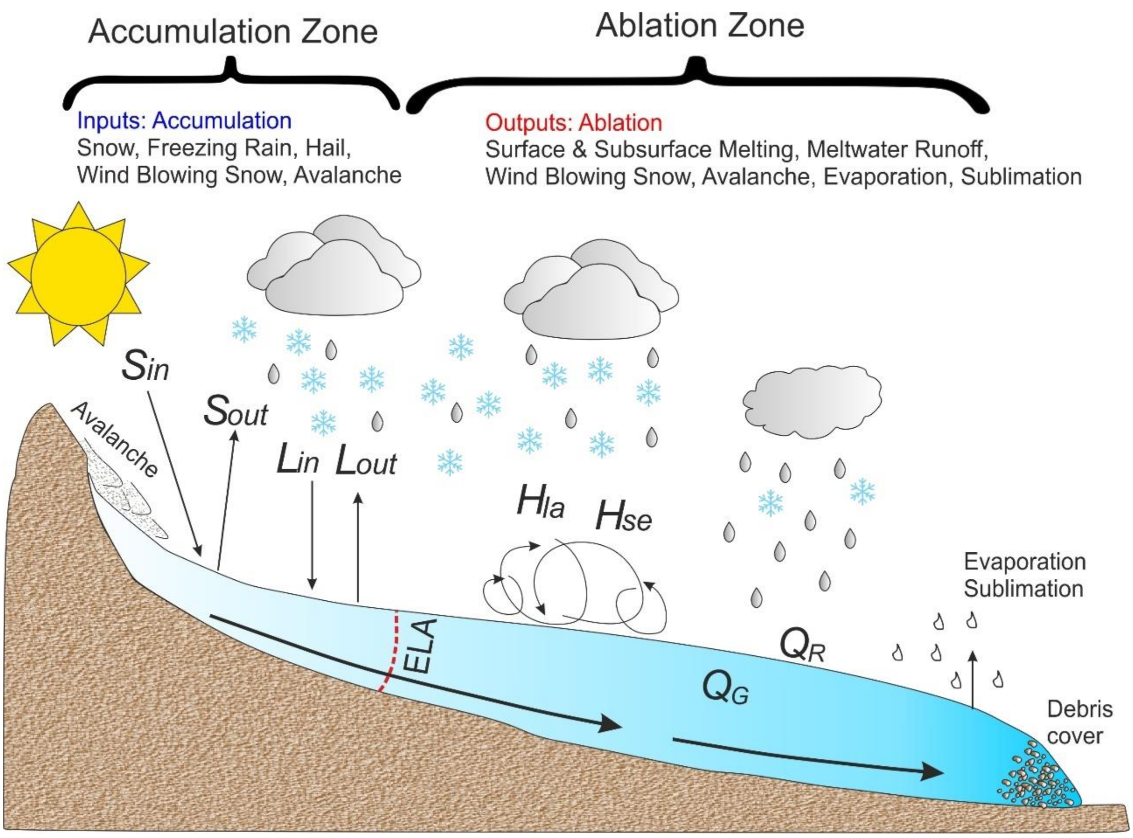

Figure 1.2. Schematic representation of glacier system and glacier surface energy balance components. Here, incoming shortwave radiation (S_{in}), outgoing shortwave radiation (S_{out}), incoming longwave radiation (L_{in}), outgoing longwave radiation (L_{out}), sensible heat flux (H_{se}), latent heat flux (H_{la}), ground heat flux (Q_{G}), rain heat flux (Q_{R}) and equilibrium line altitude (ELA).

The glacier mass balance can be estimated using various methods. These are (i) Glaciological method or direct measurements; accumulation and ablation are measured using stakes and pits placed at representative points across the glacier surface (Østrem and Stanley 1966; Østrem and Brugman 1991; Cogley et al. 2011). Stakes are inserted into the glacier surface to measure ablation and pits are excavated to measure the snow/firn thickness and density over a year for accumulation measurements. (ii)

Geodetic method; satellites or aerial images are used to compare glacier area and thickness changes over different timescale (Bamber and Rivera 2007; Cogley 2009). Also, high-resolution topographic maps or Digital Elevation Model (DEM) measured at different times are differenced to quantify volume/mass changes. Ice thickness changes can also be measured using Ground Penetrating Radar (GPR). (iii) Hydrological method; indirect estimations of annual accumulation and ablation from discharge and hydro-meteorological data is generally employed for confined drainage basins (Braithwaite 2002). This method uses a water balance equation to compute glacier mass balance. (iv) AAR/ELA method; changes in glacier Accumulation-Area Ratio (AAR) and ELA are used to estimate mass balance changes (Braithwaite 1984; Kulkarni 1992). A decrease in AAR or an increase in ELA suggests a negative mass balance, as the area of accumulation has decreased compared to the area of ablation, while an increase in AAR or a decrease in ELA indicates a positive mass balance, as the accumulation area has expanded relative to the ablation area. (v) Modeling from climate records; the mass balance of a glacier results from climate. If non-climate processes can be excluded (e.g., dynamics, avalanches, etc.) the mass balance can be derived from climate records (Oerlemans 2001; Klok and Oerlemans 2002; Hock 2005; Oerlemans 2005). Depending on the accuracy and availability of climate data a variety of models can be applied. Most models focus on the ablation season using simple degree-day approaches or more sophisticated energy balance methods. The choice of method depends on data availability, glacier size, accessibility, cost, and information required.

1.2.3 Glacier surface energy balance

The glacier surface energy balance is the balance between all energy inputs and outputs to the surface over a specific time. It is controlled by the physical properties of the glacier surface and meteorological conditions. The primary components are net radiation, turbulent sensible and latent heat fluxes, heat conduction into the glacier, and heat supplied by rain (Figure 1.2). The surface energy balance is the sum of all energy fluxes (Wm^{-2}) at the glacier surface, and is represented as:

$$Q_{melt} = (S_{in} - S_{out}) + (L_{in} - L_{out}) + H_{se} + H_{la} + Q_R + Q_G + \dots \qquad (1)$$

Where, Q_{melt} is the energy available for melting a glacier, which comes from various sources (Figure 1.2). The S_{in} is incoming shortwave and S_{out} is outgoing shortwave radiation, thus $S_{net} = S_{in} - S_{out}$ is net shortwave radiation at a wavelength of 0.2 to 4 µm that is the energy from solar and reflected radiation (Hock and Holmgren 2005). The L_{in} is incoming longwave and L_{out} is outgoing longwave radiation, thus $L_{net} = L_{in} - L_{out}$ is net longwave radiation at a wavelength of 4 to 120 µm which is the energy emitted from the Earth surface and atmosphere (Hock and Holmgren 2005). H_{se} is turbulent sensible heat flux, corresponding to the energy transferred through temperature changes in the air and surface. H_{la} is turbulent latent heat flux which is the energy released or absorbed during phase changes like condensation or evaporation on the glacier surface. Q_R is the rain heat flux that is the energy released when rain cools down to the glacier temperature and freezes, contributing to melting. Q_G is the ground heat flux which is the energy transferred through heat conduction and penetrating solar radiation from the ground beneath the glacier.

Snow or ice requires sufficient energy to reach the melting point of 0 °C before it can transition from a solid to a liquid state. Even with air temperatures at or above 0 °C, melting may not occur unless the snow or ice surface temperature reaches the melting point (Hock and Holmgren 2005). Conversely, when there is an energy deficit at the glacier surface, it can either cool the snow/ice further or facilitate the formation of new ice through freezing of surface water or condensation of water vapor (Hock and Holmgren 2005; Benn and Evans 2010).

1.3 Literature review

1.3.1 Glacier mass balance

The World Glacier Monitoring Service (WGMS) data shows that most of the glaciers around the world have been experiencing retreat with the rate of decline increasing substantially since the 1980s (Figure 1.3) (WGMS 2019). The recent studies show significant glacier decline globally, with the main drivers being rising temperature that increase melt rates and changing precipitation patterns that reduces accumulation (HockRasul et al. 2019). If current warming trends continue, some glaciers may disappear over the coming decades or centuries (Radic et al. 2014). Consequences of glacier retreat include sea level rise, changes in water supply, increased risk of glacial lake outburst floods, and habitat loss (HockBliss et al. 2019). Model projections indicate rapid reduction in glacier volume within this century, even if warming is limited to 1.5 °C above pre-industrial levels as per the Paris Agreement (HockBliss et al. 2019).

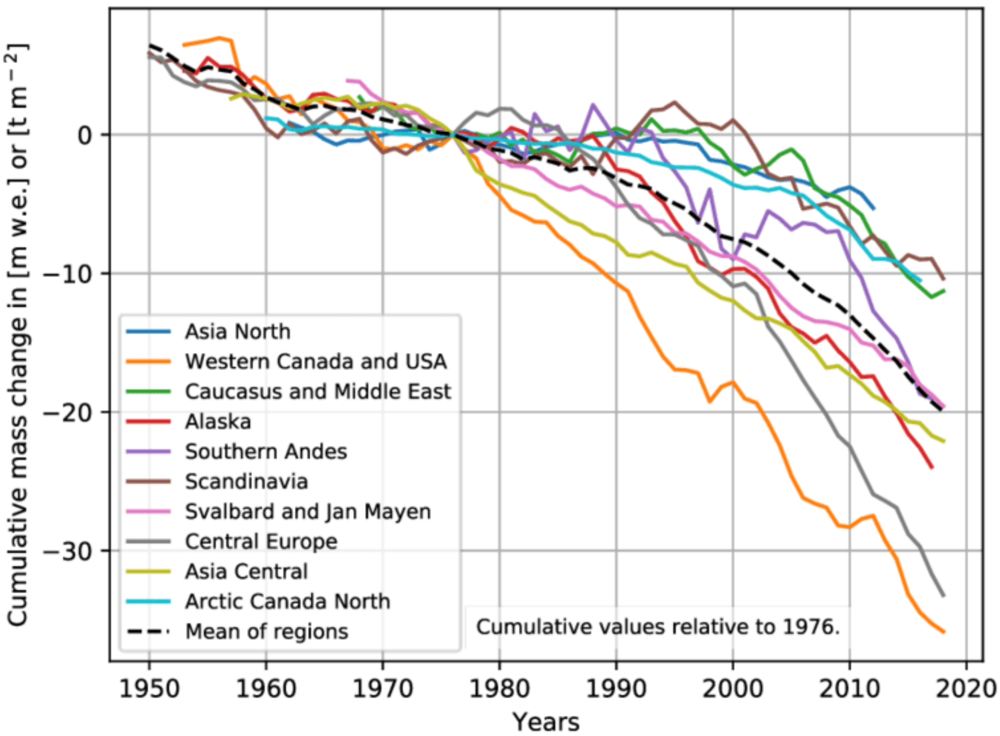

Figure 1.3. The cumulative mass balance (m w.e.) of reference glaciers worldwide shows substantial ice loss over recent decades, source: WGMS (2019).

The mass balance studies reveal that the specific mass balance vary depending on the climatic and the geographic conditions of the glaciers. Significant glacier retreat has been documented in recent decades across many different regions and mountain ranges including the Himalayas (Bolch et al. 2012; Huss 2012; Björnsson et al. 2013; Clarke et al. 2015; Brun et al. 2017; HockRasul et al. 2019; Zemp et al. 2019; Immerzeel et al. 2020; Shean et al. 2020; Hugonnet et al. 2021; Kulkarni et al. 2021; Miles et al. 2021). Figure 1.4 depicts the distributed mass balance of Himalayan glaciers from 2000 to 2016, indicating a regional mass balance of -0.28 ± 0.03 m w.e. a^{-1} and highlighting an anomaly in the Karakoram region (Miles et al. 2021). The mass balance reported by Brun et al. (2017) between 2000 and 2016 was -0.18 ± 0.04 m w.e. a^{-1}, which is comparatively less negative than the majority of other studies. SH Wang et al. (2023) found that in the west Nyainqentanglha Range, Tibetan Plateau, the glacier areal retreat accelerated from -0.26 ± 0.09 to -0.37 ± 0.15 m w.e. a^{-1} between the periods 1976-2000 and 2000-2020 over 44 years. Rajesh Kumar et al. (2021) observed an average annual specific mass balance of -0.85 m w.e. a^{-1} on Naradu Glacier (Baspa Basin, western Himalaya) from 2012 to 2018. Maurer et al. (2019) reported an average rate of ice loss of -0.43 ± 0.14 m w.e. a^{-1} from 2000 to 2016, doubling of -0.22 ± 0.13 m w.e. a^{-1} compared to 1975-2000, across Himalaya. Pellicciotti et al. (2015) found an average mass balance of -0.32 ± 0.18 m w.e. a^{-1} for debris-covered glaciers in Langtang valley from 1974 to 1999. Tak and Keshari (2020) estimated a mean specific mass loss of -0.49 ± 0.11 m w.e. a^{-1} from 1998 to 2016 for Parvati Glacier (Beas Basin, western Himalaya). Azam and Srivastava (2020) calculated a mean annual mass balance of -0.25 ± 0.37 m w.e. a^{-1} for Dokriani Glacier (Bhagirathi Basin, central Himalaya) from 1979 to 2018. Bhattacharjee et al. (2023) recorded mass balances of -0.03 m. w.e a^{-1} for Pensilungpa and Drang Drung glaciers (Suru Basin, western Himalaya) from 2000 to 2022. Raman et al. (2022) reported negative mass balances of -1.1 ± 0.03 m. w.e a^{-1} for Alaknanda Basin (central Himalaya) and -1.01 ± 0.07 m. w.e. a^{-1} for Bhagirathi Basin (central Himalaya) from 2001 to 2013. Gurung et al. (2023) estimated a mass balance of -0.39 m. w.e a^{-1} for Rikha Samba Glacier (Langtang Valley, eastern Himalaya) from 2011 to 2021, while modeling indicated -0.56 ± 0.27 m. w.e a^{-1} from 1974 to 2021. Hayat et al. (2023) observed a heterogeneous pattern of glacier mass balance in Chitral, Astore, and Hunza Basins (western Himalaya) from 2000 to 2018, with various trends ranging from 0.17 ± 0.11 to 0.23 ± 0.09 m w.e. a^{-1}. Furthermore, Pratap et al. (2016) provided a summary of research done on Himalayan mass balance before 2015.

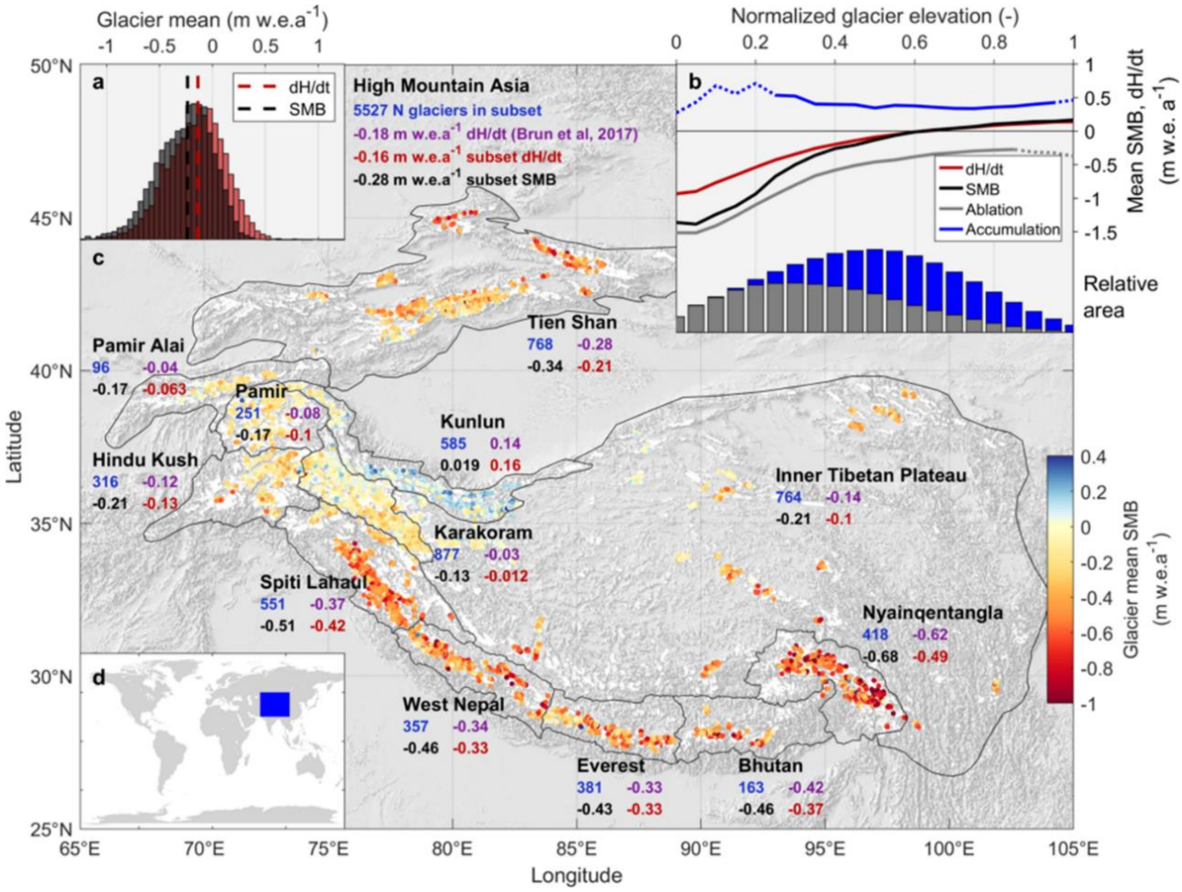

Figure 1.4. Mass balance of glaciers in the Himalaya. **a)** The mass balance across the region during 2000-2016. **b)** Area weighted mean mass balance and elevation change rate for 2000-2016 with mean accumulation and ablation rates. **c)** Distributed mass balance of glaciers. **d)** Location map of the Himalaya region. Source: Miles et al. (2021).

1.3.2 Energy balance

The initial work on the details of energy exchange between the atmosphere and a glacier surface was conducted in the early 20th century (Hock 2005). This early stage of mass balance modeling focused on snow covers and primarily aimed to provide meltwater input for watershed models. Since then, a wide range of models have been developed, ranging from simple temperature-index models (Anderson 1973; Braun 1990) to more sophisticated energy-balance models (Brun et al. 1989). Furthermore, surface energy balance studies have been carried out for glaciers in various regions globally, including the Swiss Alps (Klok and Oerlemans 2002), Andes (Pellicciotti et al. 2008), New Zealand (Alps) (Cullen and Conway 2015), Canada (Marshall 2014), Sub-Arctic (Stiegler et al. 2016), Greenland (van den Broeke et al. 2008), High Arctic (Norway) (Boike et al. 2018) and Antarctica (Reijmer and Oerlemans 2002; Van den Broeke et al. 2005; Ganju and Gusain 2017).

Catchment scale study of energy balance across Himalayan glaciers is extremely important for glacier melt (Miles et al. 2018). Table 1.1 shows surface energy flux values reported for some glaciers in the Himalaya based on the few available studies. However, in the western Himalaya region, only limited studies on surface energy balance of glaciers have been conducted. More extensive investigation of surface energy balance is needed across the diverse glacier systems in the region to better understand ablation rates and processes in this critical region. High altitude atmospheric processes and their links to energy balance need better understanding to model climate change impacts.

Table 1.1. The surface energy fluxes (Wm^{-2}) for various Himalayan glaciers. Values in square brackets are the % contribution of each energy fluxes.

Glaciers	**Period**	**Altitude (m a.s.l.)**	$S_{\mathbf{net}}$	$L_{\mathbf{net}}$	$R_{\mathbf{net}}$	$H_{\mathbf{se}}$	$H_{\mathbf{la}}$	$Q_{\mathbf{G}}$	**Reference**
Chandra Basin (WH)	10/2013-09/2019	4000-6200	64 [59]	-88 [16]	85 [75]	15 [15]	-11 [8]	- 2 [2]	Patel et al. (2021)
Leh, Ladakh (WH)	09/2015-08/2017	4727	127	-88	40	-16	-11	-1	Wani et al. (2021)
Guliya ice cap (TP)	09/2015-10/2016	5487-6650	55 [41]	−52 [40]	3	12 [9]	-11 [8]	1 [1]	Li et al. (2019)
Pindari (CH)	06/2016-07 2017	3750	[62]	[24]	[86]	[12]	[2]		N Singh et al. (2018)
Laohugou (QM)	06 to 09 2010-2015	4550	127	-46	80	6	-5	-1	Sun et al. (2018)
Zhadang (TP)	08/2010-07/2012	5665	73	-56	17	13	-11	2	Zhu et al. (2015)
Chhota Shigri (WH)	07/2013-10/2013	4670	NA	NA	87 [80]	31 [13]	11 [5]	4 [2]	Azam et al. (2014b)
Laohugou No.12 (WQ)	06/2001-09/2011	4550	NA	NA	81	7	-13	NA	Sun et al. (2014)
Zhadang (TP)	10/2009-09/2011	5660	69 [45]	-52 [37]	17 [82]	14 [10]	-9 [6]	-1 [2]	Zhang et al. (2013)
Parlung No.4 (TP)	05/2009-09/2009	4800	NA	NA	150	28	-1	-1	Yang et al. (2011)
Xixibangma (TP)	08/1991-09/1991	5700	NA	NA	28	5	-19	NA	Aizen et al. (2002)
Glacier AX010 (CH)	05/1978-09/1978	4960	NA	NA	64 [85]	8 [10]	4 [5]	Na	Kayastha et al. (1999)
	05/1978-09/1978	5080	NA	NA	55 [83]	8 [12]	3 [5]	NA	

Here: WH is Western Himalaya, TP is Tibetan Plateau, CH is Central Himalaya, QM is Qilian Mountains, WQ is Western Qilian.

1.4 Climate setting over the Himalaya

Global average surface temperatures have increased over the past century and this warming trend is predicted to continue rising unabatedly in the current century (IPCC 2023). Temperatures have increased more rapidly over mountains than the global average including in the Himalaya where warming is faster than the mainland India (Pepin et al. 2015; Sabin et al. 2020). The rate of temperature increase in the Himalaya region between 1980 and 2018 was 0.42 °C per decade, which is double the global average rate during the same period (Yao et al. 2022). In this region, mean annual air temperature increased by 0.1 °C per decade during 1901-2014, accelerating to 0.2 °C per decade in the last six decades (Kulkarni et al. 2013; Sabin et al. 2020). Furthermore, reconstructed climate data indicates accelerated warming in the Himalayan region in recent decades (Brohan et al. 2006; Morice et al. 2021). From 1991-2015, the Himalaya region experienced a 0.65 °C increase in mean temperature and decreased snowfall concurrent with increased rainfall (Negi et al. 2018), contributing to a 13% glacier area loss from 1962 to 2000 (Kulkarni and Karyakarte 2014). The Himalayan region has complex climatic conditions due to the influences of the Western Disturbance (WD) and the Indian Summer Monsoon (ISM) (Bolch et al. 2012; Maussion et al. 2014; Brun et al. 2017; Shean et al. 2020). The western Himalaya experiences higher precipitation during the winter months due to WD, whereas the central and eastern Himalaya receives more annual precipitation during the summer monsoon due to ISM (Sabin et al. 2020).

1.5 Significance of the glacier energy and mass balance study in Himalaya

Himalayan region extends over eight countries across Asia (Afghanistan, Bangladesh, Bhutan, China, India, Myanmar, Nepal and Pakistan) and is home to some of the world's largest ice volume outside the polar regions (Bolch et al. 2012). The region hosts about

95536 glaciers, covering a total area of ~97605 km^2, which accounts for 13.8% of the global glacier area (RGI6.0 2017). The total glacier volume within the region is 7070 km^3 (RJ Wang et al. 2023). These Himalayan glaciers are often called as the 'Third Pole' and the 'Water Tower of Asia', emphasizing their immense importance as a freshwater resource (Immerzeel et al. 2020). The seasonal snow and glacier ice directly affect the regional climate and freshwater availability over the Himalayan downstream region (Bolch et al. 2012; Immerzeel et al. 2020). Meltwater from the Himalayan glaciers is an essential water source for major rivers such as Indus, Ganges, and Brahmaputra, particularly during drought year or summer (Pritchard 2019). This meltwater supports hydropower generation, irrigation, and the essential needs of human populations and natural ecosystems (Pritchard 2019; Immerzeel et al. 2020; XY Li et al. 2022). However, the magnitude of runoff from the Himalayan glaciers has substantial spatio-temporal variation and is expected to vary with changing climate, affecting downstream water supply, especially for dry seasons or years (Pritchard 2019).

The elevation gradient over the Himalayan region spans a wide range, from low elevations to extremely high peaks. Over the last two decades, elevation-dependent warming (EDW) due to snow-albedo affect has become more prominent, demonstrating varying intensities across mountain regions and contributing to increased warming trends (Pepin et al. 2022; Nair et al. 2023). It shows higher temperatures over high-mountain areas than their low-elevation counterparts, drawing attention to its implications on melting glaciers (Guo et al. 2021; Nair et al. 2023). These results show a higher warming trend than average global values over the Himalayan mountains (Xu and Grumbine 2014; Azam et al. 2021). Several studies have demonstrated that the substantial loss of glacier ice mass has resulted in the rapid retreat of the Himalayan glaciers in recent decades (Bolch et al. 2012; Brun et al. 2017; Kumar et al. 2019; Shean et al. 2020). However, due to the remoteness, rugged topography and high-altitude terrain of Himalayan glaciers, in-situ hydro-meteorological measurements are limited to very few glaciers (WGMS 2019). The glacier climate interaction and glacier mass change in the Himalaya is poorly understood. Therefore, there are gaps in our understanding of various factors, including atmospheric conditions, energy fluxes, and glacier mass balance. As a result, detailed calibration and validation of model studies are sparse and filling these knowledge gaps would reduce uncertainty in predicting future of Himalayan glaciers (Mayewski et al. 2020).

Due to the influences of the WD and the ISM, the Himalayan region has complex climatic conditions, which cause variability in atmospheric conditions and mass balance over the region (Bolch et al. 2012; Brun et al. 2017; Shean et al. 2020). In addition, the heterogeneous changes in glacier mass balance are driven primarily by mechanisms associated with altitude-dependent warming, surrounding topography, land-atmospheric interactions and seasonal to inter-annual variation in atmospheric circulations on a large or regional scale (Kulkarni et al. 2007; Pepin et al. 2022; Nair et al. 2023). Further, higher temperature changes the fraction of solid to liquid precipitation, reducing accumulation (Wang et al. 2013). It intensifies the melt thereby, lengthening the duration of ablation season (Arndt and Schneider 2023). Rising snowlines expose more glacier ice, reducing surface albedo and leading to further melt through snow-albedo feedback (Bolch et al. 2012). Warming can also alter meltwater refreezing, retention, surface roughness and flow dynamics (Sakai and Fujita 2017). All these processes interact to change glaciers surface energy and mass balance. Therefore, it is essential to understand the response of glaciers to atmospheric forcing using hydro-meteorological observations and numerical models.

Although an empirical temperature index model (Hock 2003) is convenient for modeling glacier mass balance using air temperature and precipitation, this simple model does not track the energy fluxes. The energy balance model approach, which considers different energy fluxes interacting with glaciers, is valuable for detailed climate sensitivity studies and considered to be very effective for simulating the regional glacier mass balance (Oerlemans and Reichert 2000; Reid et al. 2012; Li et al. 2019). The coupling interface between surface ice and snowpack is provided by mass balance models of different complexities and physically based energy balance models that resolve the glacier surface and snowpack at high resolution as well as with an evolving microstructure. Furthermore, advanced models of energy balance can potentially simulate the surface mass balance with higher accuracy by explicitly calculating the significant effects of radiation, vertical heat transport in the snow, aging and albedo changes on the snow surface, snow densification with depth and liquid water retention (Reijmer et al. 2012). In addition to the surface energy balance, adding the snowpack to the multi-layer vertical dimension of the model enables an explicit simulation of vertical heat diffusion, the percolation of liquid water from melting and rain, the refreezing of liquid water and internal accumulation. This provides a realistic representation of firn densification caused by overloading and refreezing (Huintjes et al. 2015).

A gridded analysis for glacio-hydrological modeling studies requires distributed temperature data, amongst other meteorological variables. The lack of observational data in highly challenging terrain of high mountains has caused these modeling studies to often assume linearly decreasing surface temperatures with increasing elevation using a constant spatio-temporal environmental temperature lapse rate (6.5 °C km^{-1}) (Huang et al. 2008; Minder et al. 2010). This approach is common in various mountainous regions globally and may yield unrealistic results (Minder et al. 2010; Sheridan et al. 2010). Also, factors like inversions and cold air pooling pose a substantial challenge to this quantification (XM Li et al. 2022). Limitations of these assumptions are evident, particularly in regions where lapse rate deviate substantially from conventionally used values (Immerzeel et al. 2014). Therefore, accurately representing temperature distribution across complex glacierised terrain is critical for climate and glacio-hydrological research (Nigrelli et al. 2018; Azam et al. 2021). Understanding the air temperature lapse rate is a crucial parameter for quantifying elevation-dependent variability in precipitation phase changes, glacier melts, and other cryospheric processes across the region (Immerzeel et al. 2014; Yadav et al. 2019; Singh et al. 2023).

The WDs and the ISM are the dominant sources of precipitation over the Himalayan region that significantly affect on the mass balance of the glaciers (Shekhar et al. 2010). While WD plays a dominant role in determining glacier behaviour in the western Himalaya, the ISM plays a more critical role in the central and eastern Himalaya. The WDs mainly contribute to the winter precipitation events in the Indus Basin (western Himalaya), driven by the approaching extra-tropical synoptic-scale disturbances (Philippe et al. 2021). Furthermore, the Indus Basin is most dependent on snow and glacier melt, with nearly 62% of the total annual discharge contributed by snow and glacier melt, whereas this fraction is significantly less in the Ganges (20%) and Brahmaputra (25%) basins in the central and eastern Himalaya, respectively (Lutz et al. 2014). Thus, glaciers will have a dominant role in the water budget of the Indus Basin under future climate change scenarios (Immerzeel et al. 2020). For example, the Lahaul and Spiti region in the upper Indus Basin has experienced a higher rate of glacier ice loss compared to glaciers in western Nepal, highlighting significant spatial and temporal variations in glacier retreat (Maurer et al. 2019).

However, only a few studies from the Indus Basin were undertaken particularly on the variability of air temperature lapse rate and energy fluxes. As a result, the interactions between glaciers and atmospheric forcing are poorly constrained. Therefore, a systematic long-term study of spatio-temporal variability of air temperature lapse rate and surface energy and mass balance of Indus Basin glaciers is required. One of the major sub-basins of the upper Indus Basin is the Chandra Basin, which lies in the transition zone of WD and ISM. Since the Chandra River is passing through a semi-arid zone, its water budget is highly sensitive to the melting of snow and glaciers. Various studies show that glaciers in the Chandra Basin region have experienced negative mass balance (Table 1.2). Figure 1.5 shows the comparison of different methods used to estimate the mass balance of glaciers in this region. With the recent increase in temperature, the Chandra Basin provides an ideal testbed to understand the status and climate sensitivity of glaciers from the western Himalaya.

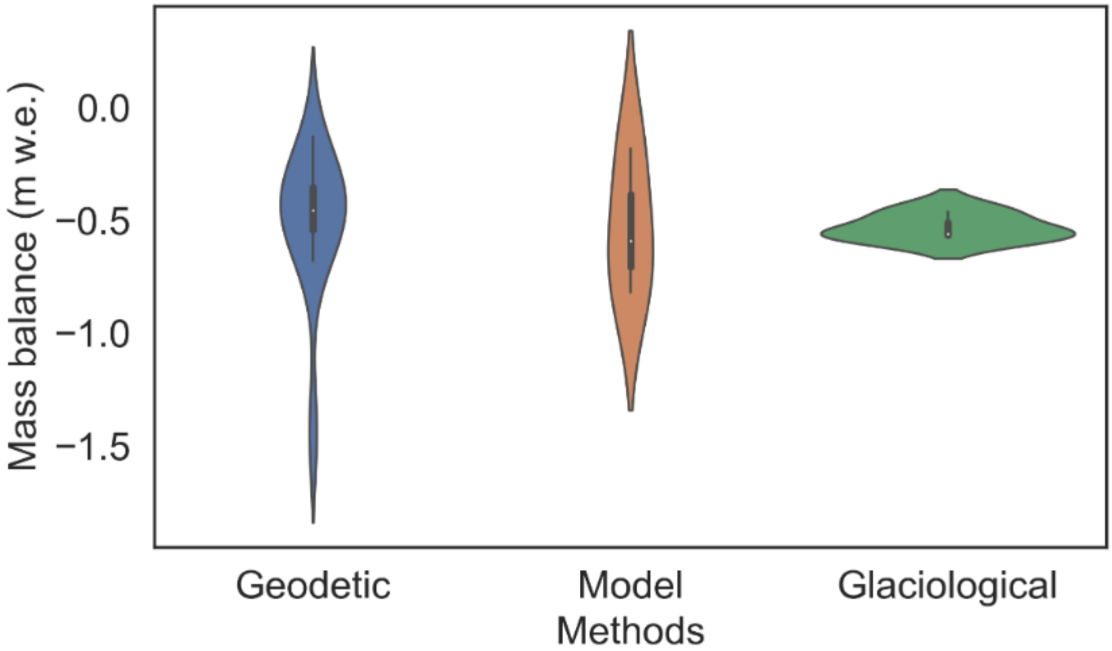

Figure 1.5. Comparison of geodetic, model, and glaciological methods for estimating mass balance (m w.e.).

Table 1.2. Various methods mean mass balance for Chandra Basin glaciers.

Mass Balance Method	Mass Balance (m w.e. a^{-1})	Year	Reference
Geodetic*	−0.47 ± 0.50	1989-2020	Chandrasekharan and Ramsankaran (2023)
VIC Model*	−0.18 ± 0.14	1980-2018	Laha et al. (2023)
Energy balance+	−0.82 ± 0.21	2015-2017	Oulkar et al. (2022)
Energy balance+	–0.59 ± 0.12	2013-2018	Patel et al. (2021)
Glaciological@	−0.57 ± 0.12	2013-2017	Sharma et al. (2020)
Glaciological$	−0.46 ± 0.40	2002-2019	Mandal et al. (2020)
Geodetic*	−0.31± 0.08	2000-2016	Shean et al. (2020)
Geodetic*	−0.13 ± 0.14	1975-2000	Maurer et al. (2019)
Geodetic*	−0.48 ± 0.15	2001-2016	Maurer et al. (2019)
Geodetic*	−0.30 ± 0.10	2000-2015	Mukherjee et al. (2018)
Geodetic*	−0.37 ± 0.09	2000-2016	Brun et al. (2017)
Geodetic*	−0.61 ± 0.46	1984-2012	Tawde et al. (2017)
Geodetic*	−0.37 ± 0.09	2000-2016	Brun et al. (2017)
Glaciological$	−0.56 ± 0.40	2002-2014	Azam et al. (2016)
Geodetic*	−0.52 ± 0.32	2000-2012	Vijay and Braun (2016)
Geodetic^	−1.44 ± 0.69	2001-2012	Mishra et al. (2014)
Geodetic*	−0.68 ± 0.15	1999-2011	Gardelle et al. (2013)
Geodetic*	−0.44 ± 0.09	1999-2011	Vincent et al. (2013)

Region: **Chandra Basin, +Sutri Dhaka, #Eight glaciers, @Five glaciers, $Chhota Shigri, ^Hampta*

In order to understand the spatio-temporal variability in air temperature lapse rate, surface energy and mass balance, it is important to undertake integrated studies using in-situ measurements and employing state-of-the-art models. In this study, response of Chandra Basin glaciers is examined using both field data and a well-constrained physically-based surface energy and mass balance model during contrasting hydrological years.

The primary aim of this doctoral thesis is to address how field data be optimally integrated into advanced models and to understand how glacier energy and mass balance react to glacier-atmosphere interactions.

1.6 Research gaps

1. The limited in-situ observations of glacier mass balance and the lack of long-term meteorological data, due to the remoteness, rugged topography, and high-altitude terrain of Himalayan glaciers, create significant gaps in understanding glacier dynamics and glacier-climate interactions. This emphasizes the need for more robust, distributed surface energy and mass balance models.
2. Insufficient studies examining the spatio-temporal variability in air temperature lapse rates and their effects on glacier mass balance across the Himalayan region.
3. Energy and mass balance model uncertainty due to the simplistic assumptions about surface characteristics, temperature distribution, and varying atmospheric conditions.
4. Limited assessment of the glacier mass balance sensitivity to different atmospheric variables and importance of snow-to-rain conversion during warmer years in amplifying the temperature sensitivity of the mass balance.

1.7 Research questions

1. How do basin-wide meteorological conditions and glacier-atmosphere interactions influence the energy and mass balance of glaciers in the Chandra Basin?
2. How does temperature variability in complex high mountain topography impact glacio-hydrological modeling, and how can this understanding be improved in the data-scarce Himalaya?
3. What are the climatic and non-climatic factors influencing the distributed surface energy and mass balance of the Chandra Basin glaciers?
4. How sensitive is glacier mass balance to changes in meteorological inputs, particularly temperature and precipitation variability, in the Chandra Basin?
5. How the mass balance uncertainty related to meteorological forcing, model parameters, and surface characteristics can be estimated?

1.8 Objectives of the study

The following are scientific objectives of this doctoral study:

1. To understand the basin-wide meteorological conditions and glacier-atmosphere interactions using in-situ meteorological observations in the Chandra Basin.
2. To study the spatio-temporal changes in the mass balance of a glacier (Sutri Dhaka glacier) in the Chandra Basin using surface energy and mass balance modeling and field-based glaciological measurements.
3. To understand the distributed surface mass balance and its sensitivity to meteorological variability in the Chandra Basin glaciers.

1.9 Thesis outline

The research work carried out in the thesis are compiled into six chapters as following:

Chapter 1 provides general introduction, literature survey and key questions addressed in the thesis. A review of the previous work pertinent to the study carried out is included. The chapter also provides an overall background on the current state of the Himalayan cryosphere. A brief overview of the physically based surface energy and mass balance is described. Based on critical knowledge gaps, the chapter raises some key questions. Furthermore, the chapter highlights the motivation of research on the proposed topic and the objectives of the study.

Chapter 2 describes the data and the techniques used in this study. This chapter contains a detailed overview of the study region (Chandra Basin, western Himalaya) and its general characteristics. It is also describes the instruments used, data collection, field measurements, details of the data processing and modeling work undertaken in this study. The methodology used in estimating the air temperature lapse rate, surface energy and mass balance is also described in this chapter.

Chapter 3 focuses on analysis of the air temperature lapse rate (TLR) over the glacierised terrain of Chandra Basin, using in-situ data obtained from the network of automatic weather stations. The chapter highlights the spatio-temporal variations in the TLR and identifies the key factors driving these variations. This chapter also explains an experiment conducted by employing a temperature-index model to demonstrate the impacts of TLR variability on glacier surface mass balance. This study provides some insights into the control of TLR for the surface mass balance of the Chandra Basin glaciers.

Chapter 4 focuses on the drivers of mass balance variability of the Sutri Dhaka Glacier from the upper Chandra Basin, using field observations along with a physically based energy and mass balance model. It provides comprehensive information on the estimation of the surface energy fluxes. This study also provides assessment of the mass balance sensitivity of the glacier to different atmospheric variables and investigate the importance of snow-to-rain conversion during warmer years in amplifying the temperature sensitivity of the mass balance.

Chapter 5 examines on the distributed surface energy and mass balance of glaciers from the upper Chandra Basin for seven hydrological years from 2015 to 2022. The sources of uncertainty related to meteorological forcing, model parameters and surface characteristics are quantified using Monte Carlo simulations in this study. This chapter provides overview of both climatic and non-climatic factors influencing the mass balance of glaciers in the region. The study also demonstrate that the glacier mass balance is highly sensitive to changes in air temperature and precipitation.

Chapter 6 summarizes the major findings and significant conclusions from this thesis work. Furthermore, this chapter gives a brief outline on future perspective and implications.

Chapter 2

2 Material and methods

2.1 The study area

The Chandra Basin is one of the major sub-basins of the Chenab River within the Indus River system, located in the Pir Panjal range in Lahaul-Spiti, Himachal Pradesh, India (Figure 2.1). The Chandra River originates from the southern slopes of the Baralacha Pass and flows for approximately 125 km through the basin before its confluence with the Bhaga River at Tandi. The basin covers an area of 2446 km^2 based on the boundary. The elevation within the basin ranges from 2800-6592 m a.s.l. The glacierised (> 0.2 km^2) area of the basin is 631 km^2, i.e., ~26% of the basin area. While it contains ~211 glaciers, only five of them have an area >20 km^2. The mean slope of the glaciers is about ∼28°. It comprises mountain and valley-type glaciers, characterized by clean ice and debris-covered glaciers (Pratap et al. 2023).

The orientation of the Chandra Basin valley divides the Pir-Panjal range and the Greater Himalayan range. It is located within the transition zone between monsoon and arid climate and experiences the ISM during summer (July–September) and the Northern Mid WDs associated with the mid latitude westerlies during winter (December –April) (Bookhagen and Burbank 2010). However, ~60-80% of the annual precipitation occurs during the winter, mainly in the form of snowfall, whereas the remaining 20-40% falls during the summer monsoon season (Koul and Ganjoo 2010; Oulkar et al. 2022).

The details related to the study area, specific to each chapter, are elaborated within the respective chapters.

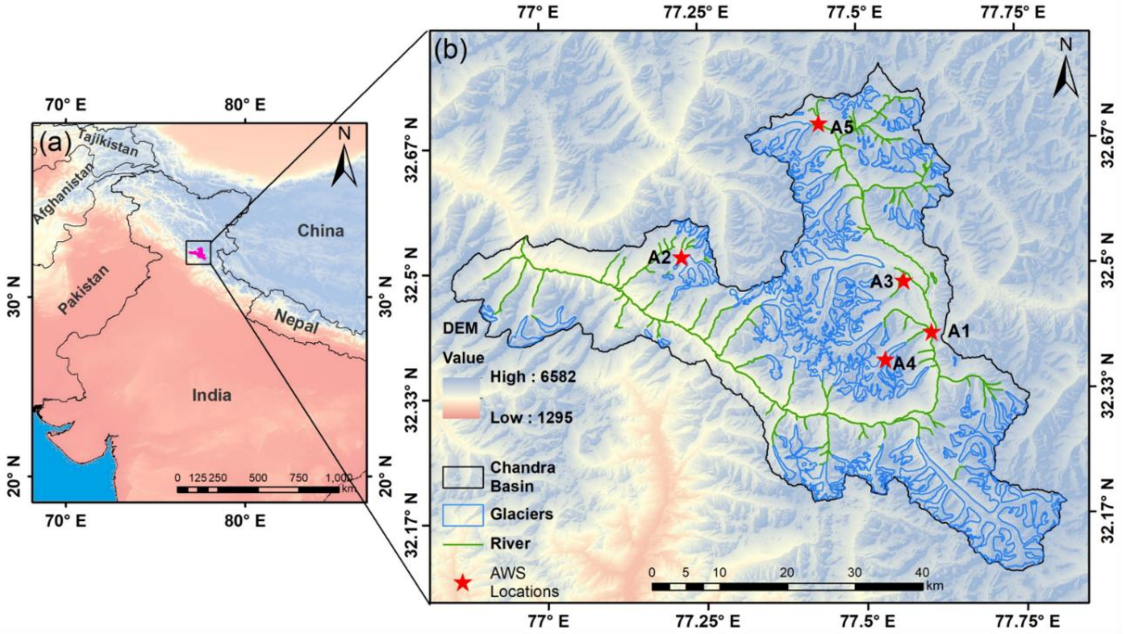

Figure 2.1. The location map of the **(a)** study region in the western Himalaya (pink) and **(b)** the Chandra Basin. The red stars are the Automatic Weather Stations (AWS) at Himansh Base Camp (A1), Gepang Gath Glacier (A2), Samudra Tapu Glacier (A3), Sutri Dhaka Glacier (A4) and Baralacha Pass (A5).

2.2 Data collection

Six glaciers in the Chandra Basin have been monitored by the National Centre for Polar and Ocean Research (NCPOR) since 2013 as part of the multidisciplinary research project entitled "Cryosphere and Climate".

2.2.1 Meteorological data

The NCPOR has installed five AWSs since October 2015 to monitor hydro-meteorological variables (Figure 2.1 and Table 2.1). The installation of the AWS was carefully considered to assess detailed meteorological conditions across the basin. Our site selection strategy focused on several key factors: diverse surface characteristics (including both glacier and rock surfaces), a range of elevations to capture orographic effects, broad spatial distribution for comprehensive coverage, representativeness of larger areas, accessibility for maintenance, and variations in slope and aspect. This strategic network design enabled us to develop a more accurate understanding of basin-wide climate, support improved modeling of glacier mass balance and runoff, provide crucial data for validating regional climate models, and enhance our ability to monitor climate change impacts in the western Himalaya. By considering these factors, we aim to capture the complex interplay of meteorological conditions across different terrain types and elevations, providing a robust dataset for climate and glaciological studies in this critical region. The AWSs mast is equipped with various sensors, such as air temperature, precipitation, wind speed and direction, relative humidity, surface temperature, incoming/outgoing shortwave and longwave radiation (Table 2.2). All analog and digital sensors are connected to a datalogger (Campbell CR1000 and CR1000X) within a watertight enclosure. The datalogger is programmed to store data every 10 minutes, 30 minutes, and at daily intervals. The data is downloaded during each field expedition in summer every year, and quality-control checks are implemented. The AWS locations and their corresponding altitudes with each site are detailed in Table 2.1. Details of the surroundings of the AWS installed over the Chandra Basin are as follows (Figure 2.2**)**:

(i) The AWS at Himansh Base Camp (A1) is situated on an open ground with a gradual slope and a northeast aspect. It is located at a ~3.5 km distance from the Sutri Dhaka Glacier snout (terminus) (Figure 2.2a).

(ii) The AWS near Gepang Gath Glacier (A2) is situated on the barren land (Figure 2.2b). It is positioned in close proximity to the proglacial Gepang Gath Lake and lies at a distance of ~0.4 km from the glacier (Figure 2.2f).

(iii) The AWS near the Samudra Tapu Glacier (A3) also lies on the barren land, ~3.8 km distance from the glacier (Figure 2.2c).

(iv) The AWS at Sutri Dhaka Glacier (A4) is situated on the upper ablation zone of the glacier (Figure 2.2d). The surroundings of A4 are characterized by snow/ice surfaces throughout the year.

(v) The AWS near Baralacha Pass (A5) is on the barren land (Figure 2.2e). Baralacha Pass is a high mountain pass in the Zanskar range where the Chandra River headwaters originate.

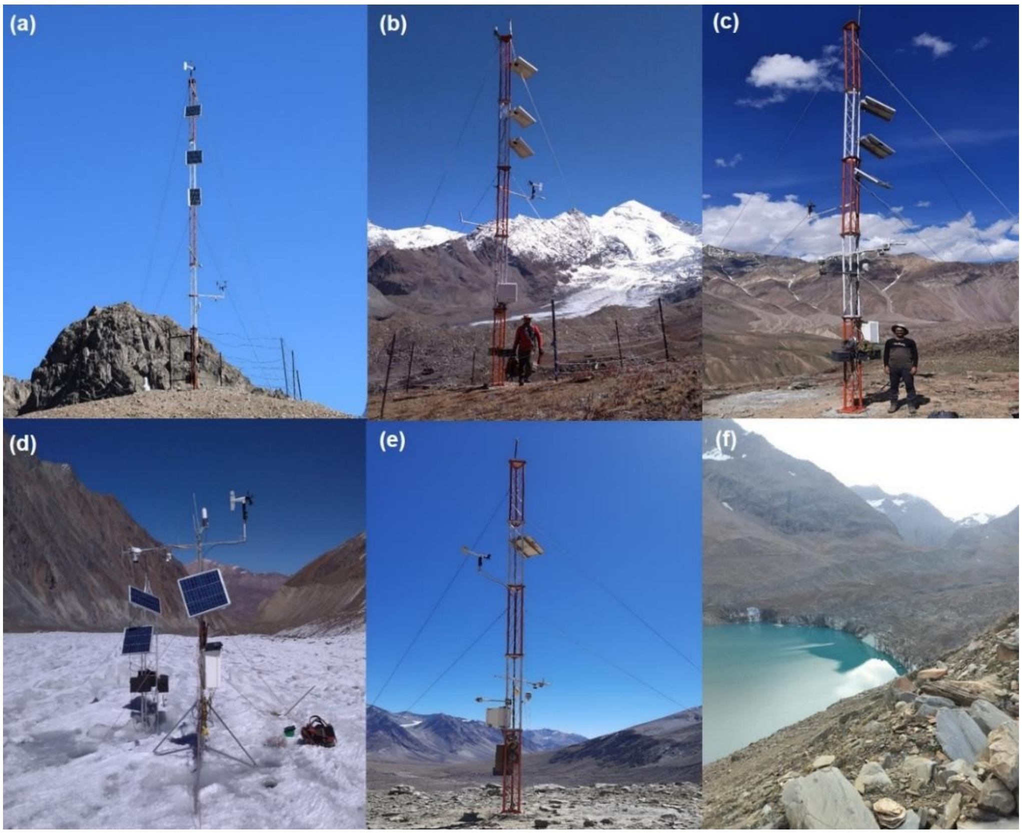

Figure 2.2. Photos of Automatic Weather Stations (AWS), **(a)** Himansh Base Camp (A1), **(b)** Gepang Gath Glacier (A2), **(c)** Samudra Tapu Glacier (A3), **(d)** Sutri Dhaka Glacier (A4), **(e)** Baralacha Pass (A5) and **(f)** Gepang Gath Lake.

Table 2.1. List of AWS locations, along with their respective altitudes.

AWSs Name	Site description	Latitude	Longitude	Altitude (m a.s.l.)
A1	At Himansh Base Camp	32.410°N	77.609°E	4052
A2	Near Gepang Gath Glacier	32.517°N	77.218°E	4244
A3	Near Samudra Tapu Glacier	32.479°N	77.567°E	4513
A4	Over Sutri Dhaka Glacier	32.375°N	77.535°E	4864
A5	Near Baralacha Pass	32.691°N	77.439°E	4904

Table 2.2. List of hydrometeorological variables measured at the AWS sites in the study.

Variables	**Sensor Type**	**Measurement Range**	**Accuracy**
Air Temperature	Campbell HC2S3	–50 ºC to +60 ºC	±0.1 ºC
Relative Humidity	Campbell HC2S3	0-100% RH	±0.8% RH
Wind Speed & Wind Direction	RM Young Sensor 05103	0 to 100 m s^{-1}	±0.3 m s^{-1}& ±3° Direction
Surface Temperature	Campbell SI-111	–55 to 80 °C	±0.5 ºC at -40 to 70 ºC
Solar Radiation (Incoming & Outgoing)	Kipp & Zonen CNR4	0 to 2000 Wm^{-2}	± 10%-day total
Longwave Radiation (Incoming & Outgoing)	Kipp & Zonen CNR4	0 to 2000 Wm^{-2}	± 10%-day total
Precipitation	OTT Pluvio²	12-1800 mm/h	± 0.05 mm
Air Pressure	Vaisala CS106	500 to 1100 hPa	±1.5 hPa (-40 to +60°C)

To prevent temperature errors caused by radiation overheating, the sensors are ventilated by radiation shields. It is placed inside a radiation shield at ~2 m (standard height) from the ground to avoid the snowpack from eventually covering the sensors. The hydrological year spans from the 1st of October in the preceding calendar year to the 30th of September in the subsequent calendar year (Oulkar et al. 2022). For convenience, the regional meteorology for the Chandra Basin is classified into two seasons, i.e., winter (1st October to 30th April) and summer (1st May to 30th September) (Oulkar et al. 2022).

Cloud cover for the study region is estimated based on net longwave radiation and air temperature following the procedure by Van den Broeke et al. (2006), which calculates a quantitative cloud cover fraction estimate ranging between 0 and 1.

2.2.2 ERA5 reanalysis data

The European Reanalysis (ERA5) represents the fifth generation of climate and weather reanalysis of the ECMWF (European Centre for Medium-Range Weather Forecasts). The hourly data of ERA5 is downloaded from Copernicus Climate Change Service (https://cds.climate.copernicus.eu/cdsapp#!/dataset/reanalysis-era5-single-levels?tab=form) (Hersbach et al. 2020). For the corresponding study period, air temperature, incoming shortwave radiation, incoming longwave radiation, air pressure, wind speed, and albedo data are downloaded from ERA5 for the nearest surface grid points to A1 and A4 AWS. This data is used to fill gaps in the AWS data through bias correction. The bias correction method involved fine-tuning the ERA5-land reanalysis data using a linear regression model to align with the observed data from the HBC AWS (Maraun and Widmann 2018). We calculated the bias by comparing the reanalysis data with the observed data during overlapping periods and applied a correction factor based on the standard deviation. This statistical adjustment ensured that the corrected data closely matched the characteristics of the observed data, improving the accuracy of the gap-filled data. Due to the unavailability of the precipitation sensor at other AWSs, only precipitation data from A1 AWS is used for analysis.

2.3 Methodology

2.3.1 Air temperature lapse rate (TLR)

2.3.1.1 TLR

The air temperature lapse rate (TLR, °C km^{-1}) is calculated independently between each station pair using the temperature (T) observations and corresponding elevations (Z). It is estimated as follows:

$$TLR = \frac{\Delta T}{\Delta Z} = \frac{T_1 - T_2}{Z_2 - Z_1} \quad (1)$$

Here, T_1 and T_2 are the air temperatures (°C) and Z_2 and Z_1 are the corresponding elevations (m a.s.l.) for the two stations.

The AWSs are distributed across the study region, spanning an elevation ranging from 4052 to 4904 m a.s.l. (Table 2.1). From the five AWSs (referred to as A1 to A5), ten unique station pairs are formed (i.e., A1-A2, A1-A3, A1-A4, A1-A5, A2-A3, A2-A4, A2-A5, A3-A4, A3-A5 and A4-A5), which allows ten distinct lapse rate estimates to characterize the temperature gradient across the study region. However, the A1-A2 pair is discarded due to inconsistent variability in derived TLR values, indicating potential microclimatic influences on the temperature observations at these locations, probably due to local topography and barriers. Also, the A4-A5 station pair is discarded as the elevation difference is less than 50 m, which falls below the analysis threshold for robust lapse rate estimation. Removing these two station pairs results in eight viable pairs meeting the elevation difference and temperature consistency criteria. Therefore, the following combinations are possible for TLR estimation (Figure 2.3): A1-A3 (ΔZ 561 m), A1-A4 (ΔZ 812 m), A1-A5 (ΔZ 852 m), A2-A3 (ΔZ 269 m), A2-A4 (ΔZ 620 m), A2-A5 (ΔZ 660 m), A3-A4 (ΔZ 351 m), and A3-A5 (ΔZ 391 m).

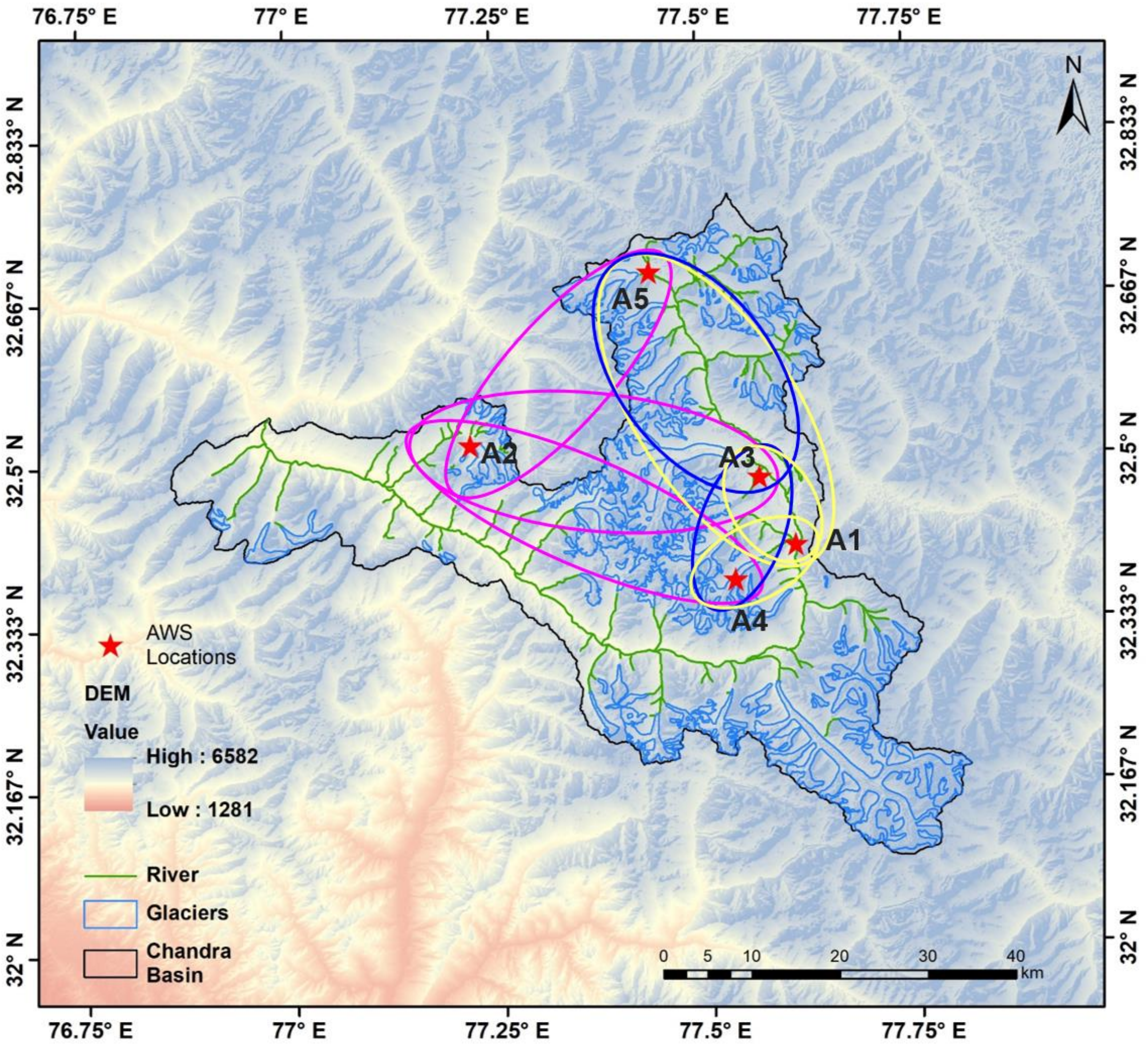

Figure 2.3. The selected catchment for the estimation of temperature lapse rate (TLR) (ºC km^{-1}). The AWSs pairs are A1-A3, A1-A4, A1-A5, A2-A3, A2-A4, A2-A5, A3-A4, and A3-A5.

2.3.1.2 TLR application for mass balance using T-index-based model

A temperature-index (T-index) glacier melt model (Hock 2003) is used to evaluate the need for using the observed site-specific TLR for estimating glacier surface mass balance over the Chandra Basin. The T-index model is forced with in-situ air temperature data obtained from the A1 station and bias-corrected ERA5 precipitation data (Hersbach et al. 2020) for the hydrological years 2015 to 2022. Here, a threshold temperature (0 °C) is used for partitioning the solid and liquid precipitation (Laha et al. 2023). The model runs at hourly timestep and estimates mass balance by extrapolating the temperature and precipitation to each 100 m altitudinal band based on the TLR and constant precipitation scale factor. Model runs are conducted to demonstrate the mass balance sensitivity to TLR (1) using the observed TLR from the AWS data and (2) using a constant environmental TLR of 6.5 °C km^{-1}.

The extrapolation of the temperature and precipitation to each 100 m altitudinal band is estimated as follows:

$$T_i = T_{air} - TLR \ x \ \Delta Z \tag{2}$$

$$P_i = P - P_G \ x \ \Delta Z \tag{3}$$

Where, T_i (°C) is the calculated temperature at 100 m altitudinal bands, T_{air} is the temperature at A1 AWS, ΔZ is the elevation difference between A1 AWS and the corresponding altitudinal band, and TLR is the lapse rate. P_i (mm) is the calculated precipitation at 100 m altitudinal bands, P is the precipitation at A1 AWS, and P_G is the precipitation scale factor. For the study, a precipitation scale factor of 1.4 is used (Laha et al. 2023).

The accumulation A_i (mm w. e. d^{-1}) at 100 m altitudinal band is estimated as:

$$A_i = \begin{cases} P_i & : T_i > T_p \\ 0 & : T_i \leq T_p \end{cases} \tag{4}$$

Where, P_i and T_i are precipitation (mm) and air temperature (°C), respectively, extrapolated at each altitudinal range and T_p is the threshold temperature (°C) for snow-rain.

The ablation M_i (mm w. e. d^{-1}) at each 100 m altitudinal band is estimated as:

$$M_i = \begin{cases} DDF \ x \ (T_i - T_m) & : T_i > T_m \\ 0 & : T_i \leq T_m \end{cases} \tag{5}$$

Where, DDF denotes the degree-day factor (mm d^{-1} °C^{-1}), T_i is extrapolated air temperature (°C) at each altitudinal band and T_m is the threshold temperature (°C) for melt. In the study, the degree-day factor (DDF) is 5 mm d^{-1} °C^{-1} for ice melt and 3 mm d^{-1} °C^{-1} for snow melt (Laha et al. 2023).

Mean mass balance (b_i) is calculated using ablation (M_i) and accumulation (A_i) as:

$$b_i = A_i - M_i \tag{6}$$

Glaciers mass balance (B_a) is calculated as:

$$B_a = \frac{\sum b_i a_i}{S} \tag{7}$$

Where, b_i is the mass balance at each altitudinal band, a_i is the area for each altitudinal band, and S is the total glacier area.

2.3.1.3 TLR uncertainty analysis

The AWS data from the air temperature sensor provides highly accurate measurements with a precision of ±0.1 ºC, however, variations in sensor height and surface characteristics (e.g. glacier surface, barren land) between AWS sites may impact the observations. The effect of varying sensor height in combination with different surface characteristics on temperature measurements, especially within the high elevation basin boundary layer, leads to significant errors in TLR estimation (Marshall et al. 2007). Additionally, the accuracy of elevation measurements, influenced by Global Positioning System (GPS) accuracy and manual measurement precision, may introduce uncertainties in TLR estimation. The error in the temperature and elevation observations propagates and gets amplified in the TLR estimation (Marshall et al. 2007; Petersen and Pellicciotti 2011). Therefore, it is essential to consider these factors in the analysis to assess the accuracy of the calculated TLR values. The associated uncertainty is estimated using the following relations.

$$\frac{\Delta TLR}{TLR} = \sqrt{(\frac{\Delta T}{\delta T_{air}})^2 + (\frac{\Delta Z}{\delta Z})^2} \tag{8}$$

$$\Delta T = \sqrt{(\Delta \mathrm{T}_{sensor})^2 + (\Delta \mathrm{T}_{human})^2} \tag{9}$$

$$\Delta Z = \sqrt{(\Delta \mathrm{Z}_{GPS})^2 + (\Delta \mathrm{Z}_{human})^2} \tag{10}$$

Here, δT_{air} is the air temperature difference, ΔT is the air temperature observation uncertainty, $\Delta \mathrm{T}_{sensor}$ (±0.1 ºC) is the air temperature sensor accuracy and $\Delta \mathrm{T}_{human}$ comprises potential localized temperature differences due to variations in the sensor height and surface characteristics (e.g. glacier surface, barren land) between AWSs. $\Delta \mathrm{T}_{human}$ have been taken as ±0.2 °C. The δZ is the elevation difference, and ΔZ is the elevation measurement uncertainty. It includes contributions from both GPS accuracy and manual measurement accuracy. GPS elevation accuracy ($\Delta \mathrm{Z}_{GPS}$) is ±3.2 m, based on typical uncertainties reported in GPS specifications (Garmin GPS) (Fator and Zomrawi 2015). Manual elevation measurements ($\Delta \mathrm{Z}_{human}$) is taken as ±4 m, based on analyzing human measurement errors and variabilities.

2.3.2 Field-based glaciological surface mass balance

The surface mass balance of two Chandra Basin glaciers (Sutri Dhaka and Samudra Tapu Glaciers) is measured using the in-situ glaciological method following established methodologies (Østrem and Brugman 1991; Cogley et al. 2011). The annual ablation and accumulation measurements are performed at the end of the ablation season (end of September). Ablation is measured using a network of stakes, and accumulation is measured through excavating snow pits or snow coring (Kovacs Mark II) at various locations on the glacier (Figure 2.4). A network of 30-35 (per year) ablation stakes is drilled into the ice over the glacier surface along with different altitudinal zones for the study years. These stakes are measured throughout the summer for ablation estimation using exposed stake heights. Ice density for the ablation zone is considered to be 870 kg

m^{-3} (± 25 kg m^{-3}, n=10), and the snow density of 490 kg m^{-3} (± 30 kg m^{-3}, n=8), which is measured in the field at the end of ablation season (Pratap et al. 2019b). The accumulation zone of the glacier for glaciological measurement is accessible up to ~5700 m a.s.l. To estimate the total accumulation, the snow density, snow water equivalent and depth measurements are extrapolated for the entire accumulation area. Mass balance is calculated using the sum of accumulation and ablation and integrated over the entire glacier surface area. The glacier-wide average annual mass balance is calculated using:

$$B = \frac{1}{S}\sum b_n s_n \tag{11}$$

Where, B is the glacier-wide average annual mass balance, b_n is the mass balance of the altitudinal range, s_n is the area of corresponding ablation or accumulation altitudinal range, and S is the total area of the glacier.

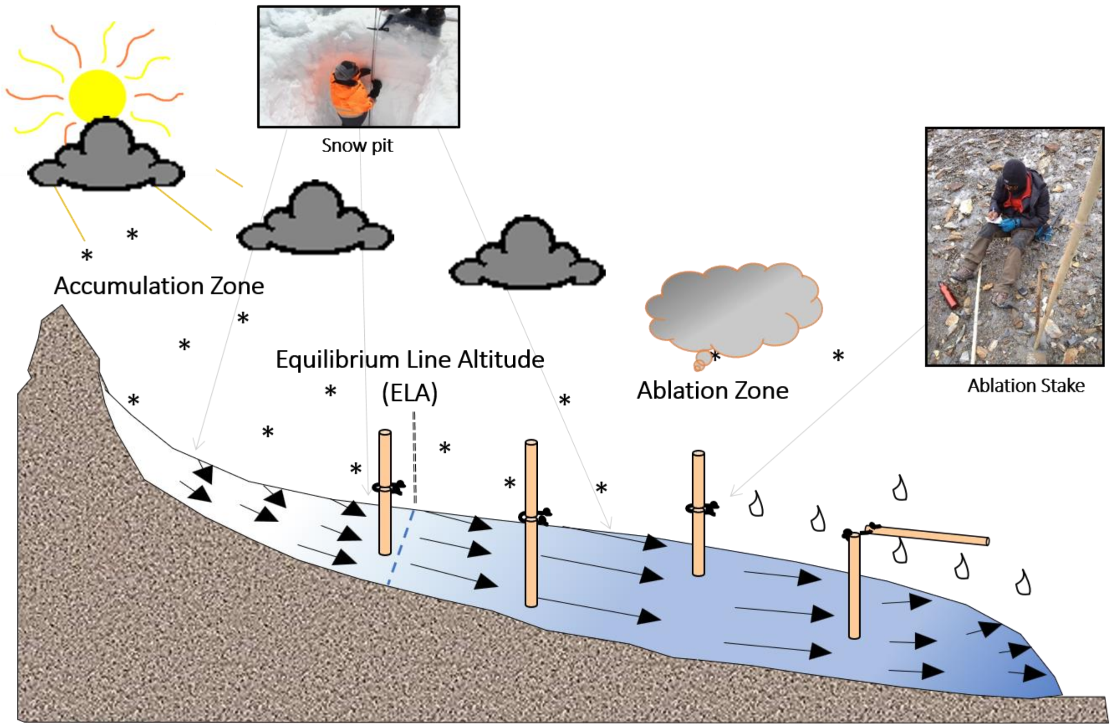

Figure 2.4. The schematic representation of ablation and accumulation measurements of glaciers.

2.3.2.1 *Glaciological surface mass balance uncertainty*

The potential annual mass balance uncertainties in the in-situ observations are related to: (i) the uncertainties in ablation estimates related to stake height measurements and ice density; (ii) the uncertainties in accumulation observations of snow depth and snow density, and (iii) the uncertainty related to the extrapolation of point measurements of corresponding altitudinal bands and the entire glacier (Thibert et al. 2008). The uncertainties in stake height measurements could be due to the mean height difference. Although a representative surface is chosen in the vicinity to install the stakes, the variability associated with the surface morphological changes (such as meltwater channels, boulders and avalanches) cannot be evaluated. Rather, those stakes with such uncertainties are excluded from the final calculation. Therefore, the propagated uncertainty associated with extrapolation of the ablation is ±0.19 m w.e. a^{-1}. It is derived from the errors in stake height differences over time intervals (random errors) and the uncertainties during glacier-wide interpolation (systematic errors) (Zemp et al. 2013; Stumm et al. 2021). For each point measurement, the error in annual ablation (Δ_{Aa}) is calculated from the error in stake height (H) change measurement (Δ_{h}), the uncertainty in the ice density (D) used to convert height changes to water equivalent (Δ_{d}), and the error in debris thickness (Δ_{dt}) due to varying debris thickness (Dt). The total error for an individual ablation stake measurement over a balance year is computed as follows:

$$\frac{\Delta_{Aa}}{Aa} = \sqrt{\left(\frac{\Delta_h}{H}\right)^2 + \left(\frac{\Delta_d}{D}\right)^2 + \left(\frac{\Delta_{dt}}{Dt}\right)^2} \qquad (12)$$

Further, the uncertainty in accumulation measurements is calculated following the approach by Kenzhebaev et al. (2017); (i) The uncertainties in snow density are estimated as ±30 kg m^{-3} for the calculation of the accumulation. (ii) 0.22 m w.e. $(100\ m)^{-1}$ is used as the accumulation gradient measured at the Chhota Shigri Glacier (MF Azam et al.

2016) to approximate a linear increase in accumulation. (iii) For the two uppermost altitude bins, an inverse gradient is adopted. The uncertainty in accumulation measurements (±0.28 m w.e. a^{-1}) is calculated using the mean of standard deviations obtained using the methods described above. Taking all the errors into account, an overall uncertainty in observed mass balance at the glacier is calculated as ±0.33 m w.e. a^{-1}. This is well within the estimated uncertainties of the glaciological methods ranging from ±0.27 to ±0.53 m w.e for various Himalayan glaciers (Azam et al. 2012; Wagnon et al. 2013; Sunako et al. 2019; Mandal et al. 2020; Soheb et al. 2020).

2.3.3 Model

To simulate the distributed surface energy and mass balance, the COSIMA (COupled Snowpack and Ice surface energy and MAss balance) and COSIPY (COupled Snowpack and Ice surface energy and mass balance model in Python) models are used, which are open source physically-based energy balance models for high mountain glaciers (Huintjes et al. 2015; Sauter et al. 2020). COSIMA 1D is used to estimate the energy and mass balance at a single point, considering only temporal variations. On the other hand, COSIMA 2D accounts for both spatial and temporal variations to estimate energy and mass balance. The modelling study on Sutri Dhaka Glacier began in early 2019, when the COSIMA model (Huintjes et al. 2015) was available in MATLAB for energy mass balance estimation. At that time, COSIPY, a more advanced Python-based model, had not yet been developed. However, by 2020, COSIPY (Sauter et al. 2020) became available, and for subsequent studies on glaciers in the upper Chandra Basin, the updated COSIPY model was adopted to estimate the energy and mass balance more precisely. While retaining the fundamental structure of COSIMA, the COSIPY is coded in Python, offering enhanced computational efficiency. The parameterization of subsurface energy and mass fluxes within the model is directly coupled to the surface processes like other widely used surface energy and mass balance studies (Klok and Oerlemans 2002; Hock and Holmgren 2005; Pellicciotti et al. 2009). The model includes several modules that solve the heat equation and calculate surface temperature and energy balance, meltwater percolation, refreezing and densification (Figure 2.5) (Huintjes et al. 2015; Sauter et al. 2020). It explicitly calculates the percolation of meltwater and the refreezing process within the snowpack, taking into account the latent heat flux release and resulting subsurface melt and the effects on subsurface temperature, snow density and the ground heat flux. Furthermore, the model can effectively estimate the mass balance by explicitly calculating the effects of radiation, aging and albedo changes on the snow surface, vertical heat transport in the snow, densification of snow with depth, and liquid water retention (Huintjes et al. 2015; Sauter et al. 2020). In addition to the full energy balance on the surface, adding snowpack to the multi-layer vertical dimension of the model enables an explicit simulation of vertical heat diffusion, percolation of liquid water from melting and rain, the refreezing of liquid water and internal accumulation, and a realistic representation of firn densification due to overloading and refreezing (Huintjes et al. 2015; N Singh et al. 2018; Sauter et al. 2020).

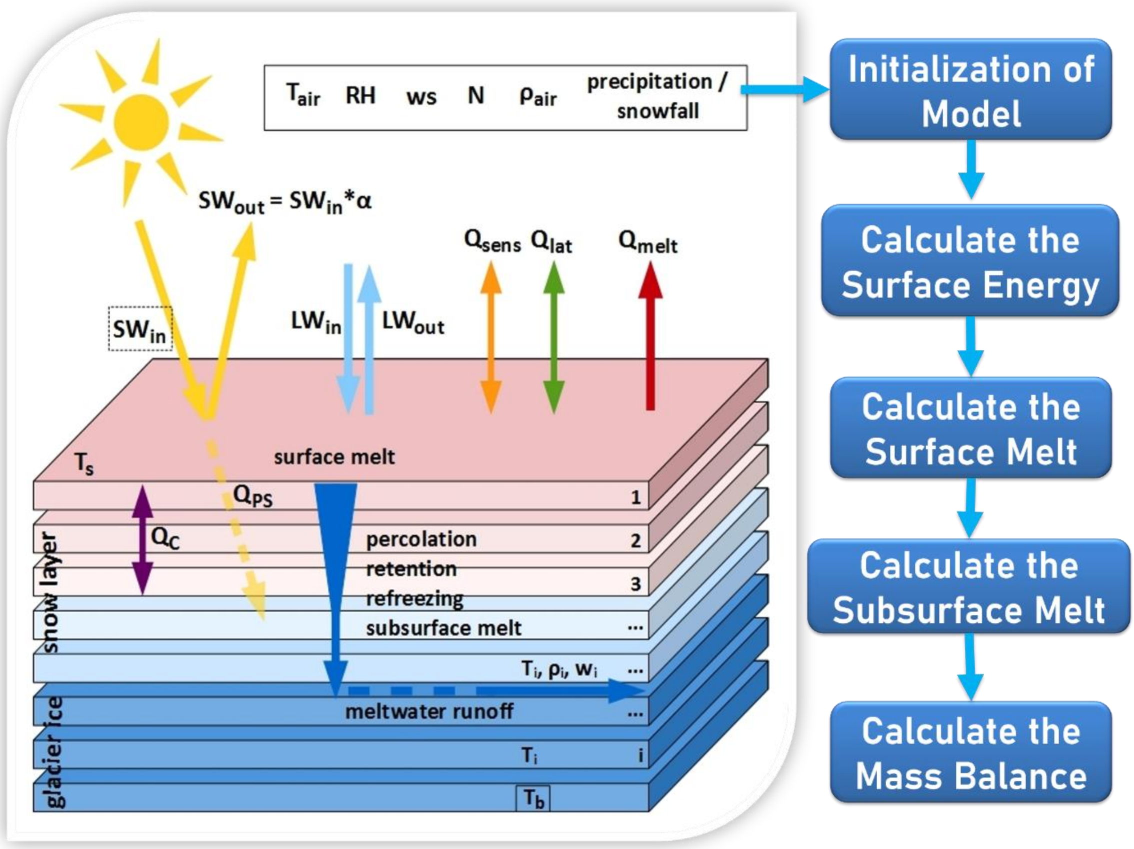

Figure 2.5. A diagram of multi-layer snowpack surface energy balance and mass model. (Adapted from Huintjes et al. (2015)).

The model is forced with meteorological data, including air temperature, relative humidity, total precipitation, wind speed, air pressure, incoming shortwave radiation, and cloud cover fraction. The hourly data of meteorological variables along with the re-sampled DEM are used to derive the spatial distribution of surface energy and mass balance for the Sutri Dhaka Glacier and the upper Chandra Basin glaciers for corresponding study period.

2.3.3.1 Mass balance model

The model is based on energy and mass conservation and estimates surface energy and mass balance. It combines a surface energy balance model with a multi-layer snow and ice model to calculate energy fluxes, subsurface processes, and mass balance at a given resolution (Huintjes et al. 2015; Sauter et al. 2020). The mass balance is estimated as follows:

$$MB = Ab + Ac + Aci + Abi \tag{13}$$

Where, Ab is surface ablation from melt and sublimation, Ac is an accumulation from snowfall and deposition, Aci is an internal accumulation from refreezing, and Abi is internal ablation from subsurface melt (from penetrating radiation).

Solid precipitation (snowfall) contributes directly to accumulation. Liquid precipitation (rainfall) and meltwater percolate through the snowpack following a tipping bucket approach based on the liquid water holding capacity (Huintjes et al. 2015; Sauter et al. 2020). Refreezing occurs when snow temperature is below 0 °C and liquid water is present from rainfall or melt. Excess meltwater that reaches the bottom of the snowpack contributes to runoff. The model uses a dynamic mesh with variable layering to represent the vertical profile of snow and ice properties, including temperature, density, liquid water content, and ice fraction (Huintjes et al. 2015; Sauter et al. 2020). Layer thickness adapts over time, with thinner layers near the surface and increasing thickness with depth.

2.3.3.2 Surface energy balance model

The total energy flux (Wm^{-2}) at the glacier surface is calculated within the model (Oerlemans 2001; Huintjes et al. 2015; Sauter et al. 2020) as follows:

$$Q = S_{in}(1-\alpha) + L_{in} + L_{out} + H_{se} + H_{la} + Q_G \tag{14}$$

Where, Q is the total heat flux, S_{in} is incoming shortwave radiation, α is the surface albedo, L_{in} is incoming longwave radiation, L_{out} is outgoing longwave radiation, H_{se} is turbulent sensible heat flux, H_{la} is turbulent latent heat flux and Q_G is ground heat flux. Heat flux from liquid precipitation is negligible and hence neglected in the model (Huintjes et al. 2015).

In the Chapter 4 for the Sutri Dhaka Glacier, the S_{in} is calculated separately, following the approach by Huintjes et al. (2015). First, a solar radiation model by Kumar et al. (1997) is used to compute clear-sky and diffuse incoming shortwave radiation ($S_{,\mathrm{pot}}$) without considering the cloud effect at A4 AWS with no shading. The cloud effect of the $S_{,pot}$ is corrected with incoming shortwave radiation data of A4 AWS to determine the correction factor, which is further used in the study to derive spatially S_{in}. However, in the Chapter 5, for the selected glaciers in the upper Chandra Basin, the S_{in} is estimated using the approach by Georg et al. (2016) within the COSIPY (Sauter et al. 2020).

The modelled L_{in} and L_{out} are estimated using Stefan–Boltzmann law (Klok and Oerlemans 2002). L_{in} is a function of water vapour pressure, air temperature, cloud cover, whereas L_{out} is a function of surface temperature. The Q_G consists of fluxes due to heat conduction and penetrating shortwave radiation (Q_{ps}). The Q_{ps} remains negative, as it only transfers energy from the glacier surface into the snow or ice. The turbulent heat fluxes H_{se} and H_{la} are calculated using the bulk aerodynamic method with correction of stability (Oerlemans 2001). The bulk transfer coefficients for H_{se} and H_{la} depends on the instrument height (z), and surface roughness length (z_0). The z_0 changes depending on time from fresh to aged snow (Molg and Scherer 2012). The z_0 increases linearly from 0.24 mm for fresh snow (Gromke et al. 2011) to 4 mm for aged snow (Brock et al. 2006), whereas z_0 is assumed to be 1.7 mm for the snow-free surface (Cullen et al. 2007).

The turbulent sensible heat flux is calculated as:

$$H_{se} = \rho_{air} \; x \; c_p \; x \; C_{se} \; x \; u \; (T_{air} - T_{surf}) \qquad (15)$$

Where, ρ_{air} is the air density, c_p is the specific heat capacity of air (1004.67 J kg^{-1} K^{-1}), C_{se} is bulk transfer coefficient, u is wind speed, T_{air} is the air temperature and T_{surf} is surface temperature.

The turbulent latent heat flux is calculated as:

$$H_{la} = \rho_{air}\ x\ L_{E/S}\ x\ C_{la}\ x\ u\ (q_{air} - q_{surf}) \tag{16}$$

Where, ρ_{air} is the air density, L_E is the latent heat of evaporation (2.514×10^6 J kg^{-1}), L_S is the latent heat of sublimation (2.849×10^6 J kg^{-1}), u is wind speed, C_{la} is bulk transfer coefficient, q_{air} is specific humidity at 2 m and q_{surf} is specific humidity at the surface. The q_{air} is estimated from relative humidity, whereas for q_{surf} the relative humidity is assumed to be 100% at the surface.

All energy fluxes are expressed in Wm^{-2} and defined as positive when it is towards the surface of the glacier and negative when it is away from the surface. The resulting flux Q leads to surface melt energy (Q_{melt}) only when the surface temperature is at the melting point (0 ºC). The subsurface model uses a vertical layer structure consisting of layers equal to 0.2 m. The temperature, density, and depth are characterized by each subsurface snow/ice layer. The initial temperature profile is interpolated linearly between air temperature and surface temperature. Each time step calculates the surface temperature profile from the thermodynamic heat equation (Huintjes et al. 2015). The initial snow depth is set to zero at the start of the balance year (i.e., 1st October). Thus, the subsurface density profile is initialized with a constant glacier ice density of 870 kg m^{-3} and a snow density of 490 kg m^{-3} based on field observations (Pratap et al. 2019b). The values for site-specific constants within the model are adopted from Klok and Oerlemans (2002) and Huintjes et al. (2015) for simulations at the glaciers.

2.3.3.2.1 The parameterization of surface albedo

At each DEM pixel, the glacier surface characteristics are controlled by surface temperature and albedo, determined in the model at each time step and changed linearly over time from fresh to aged snow. The parameterization of surface albedo (α) follows the scheme of Oerlemans and Knap (1998), where α is determined as a function of snowfall frequency and snow depth:

$$\alpha_{snow} = \alpha_{firn} + \left(\alpha_{frsnow} - \alpha_{firn}\right) exp\ (t_{snow}\ t^{*-1}) \tag{17}$$

$$\alpha = \alpha_{snow} + (\alpha_{ice} - \alpha_{snow})\ exp\ (-h\ d^{*-1}) \tag{18}$$

The free parameters of the surface albedo scheme are determined according to Molg and Scherer (2012) and measurements at A4 AWS between 2015 and 2017. The values are fresh snow albedo (α_{frsnow}) = 0.9, firn albedo (α_{firn}) = 0.55, and ice albedo (α_{ice}) = 0.2. However, t_{snow} is the time since the last snowfall, t* is constant (6 days) for the effect of aging on snow albedo, h is the snow depth and d* is a constant (8 cm) for the effect of snow depth on albedo.

2.3.3.2.2 Estimation of precipitation phase

The precipitation phase is calculated using the sigmoidal relationship technique, which takes the form of a hyperbolic tangent function and is air temperature dependent (Dai 2008; Ding et al. 2014; Harpold et al. 2017). The following equations are used to distinguish between snowfall and rainfall (Huintjes et al. 2015):

$$snowfall = \mathrm{P}\ x\ (0.5\ x\ (-\tanh\ (((T_{air} - 273.15) - 2.5)\ x\ 2.5) + 1)) \tag{19}$$
$$snowfall\ (snowfall < 0) =\ 0$$

$$rainfall = (P - snowfall)\ x\ 0.25 \tag{20}$$
$$rainfall\ (rainfall < 0) =\ 0$$

Where, T_{air} is the air temperature, and P is the total precipitation.

2.3.3.3 *Sensitivity experiments*

To assess climate sensitivity of the glaciers, the meteorological variables are perturbed according to the climatic factors and associated simulations (Yang et al. 2011; Yang et al. 2013; Sun et al. 2018; Zhu et al. 2018; Li et al. 2019). The sensitivity experiments are performed for mass balance by changing the assumed value for one input parameter at a time, leaving all other parameters unchanged for Sutri Dhaka Glacier. The perturbed value is defined as ±1°C for air temperature, ±10% for relative humidity, ±50 Wm^{-2} for incoming shortwave radiation, ±10% for total precipitation, and ±1 m s^{-1} for wind speed throughout the period.

The sensitivity of mass balance (MB) to temperature ($\frac{\mathrm{dMB}}{\mathrm{dT}}$) and precipitation ($\frac{\mathrm{dMB}}{\mathrm{dP}}$) is calculated following Oerlemans and Knap (1998) and Azam et al. (2014a) as:

$$\frac{dMB}{dT} \cong \frac{MB(+1°C) - MB(-1°C)}{2} \cong MB(+1°C) - MB(0°C) \qquad (21)$$

$$\frac{dMB}{dP} \cong \frac{MB(P+10\%) - MB(P-10\%)}{2} \cong MB(P + 10\%) - MB(P) \qquad (22)$$

Furthermore, the variations in air temperature and precipitation play pivotal roles in driving glacier mass balance changes, as explored through simulations conducted to investigate their impact on the mass balance of the Sutri Dhaka Glacier (Oulkar et al. 2022). Therefore, in order to evaluate the climate sensitivity of the upper Chandra Basin glacier mass balance, perturbation experiments of air temperature and precipitation are performed. To simulate temperature variations, the air temperature changes by a step of 0.5 °C from -2 °C to +2 °C. Similarly, simulations are conducted to explore the effects of precipitation changes using eight scenarios, where the precipitation is adjusted in 10% increments from -40% to +40%. During these simulations, other pertinent variables remain constant. Additionally, a coupled parameter perturbation approach is employed, wherein alterations in both air temperature and precipitation are simultaneously introduced as forcings to the model. This approach mainly sought to address the extent to which changes in precipitation could compensate for the additional loss of glacier mass attributed to a 1 °C increase in air temperature.

2.3.3.4 Model uncertainty assessment using Monte Carlo simulations

The uncertainty in the model result comes from different sources, such as meteorological variable measurements, uncertainty of energy fluxes, model parameters, threshold values, etc. Therefore, to assess model uncertainty, 100 Monte Carlo simulations are performed with varying model parameters and thresholds by 10% and meteorological inputs within measurement uncertainty ranges, following van der Veen (2002) and Machguth et al. (2008). Model uncertainty is quantified by running repeated simulations at all observed point locations over Samudra Tapu and Sutri Dhaka Glacier. Based on the results of the 100 simulations compared against the observed mass balance, there is a well match between the uncertainty range and observed mass balance. This uncertainty range is determined by calculating the standard deviation of the mass balance results. The standard deviation captures the spread in mass balance estimates from the 100 simulations. With a normal distribution of results, about 68% of simulations are within ±1 σ from the mean. Therefore, the ±25% uncertainty range represents approximately ±1 σ of the mass balance results from the simulations.

Chapter 3

3 Temporal variability in air temperature lapse rates across the glacierised terrain of the Chandra Basin, western Himalaya

3.1 Introduction

The EDW in the high mountains, where temperature is systematically higher over high-mountain areas as compared to their low-elevation counterparts, has led to concerns due to its implications for melting glaciers (Palazzi et al. 2019; Guo et al. 2021; Nair et al. 2023). However, the warming rate does not monotonously increase with elevation as there are factors affecting it. Due to limited observations, the modeling studies often assume linearly decreasing temperature with increasing elevation using a constant (6.5 °C km^{-1}) spatio-temporal environmental TLR (Huang et al. 2008; Minder et al. 2010). This approach used in various mountainous regions may potentially yield unrealistic results (Mihalcea et al. 2008; Minder et al. 2010; Sheridan et al. 2010; Li et al. 2013). The regional TLR fluctuates on both seasonal and diurnal scales due to the complex interaction between surface characteristics and the local atmospheric conditions. This variability leads to distinct microclimates within the basin, influencing various climatic and glacio-hydrological processes (Minder et al. 2010; Kattel et al. 2015; Sun et al. 2022). It influences the distribution of snow cover, the timing of snow/ice melt onset at different elevations, runoff patterns, wind speed and direction, precipitation distribution, surface pressure gradient and heat exchange processes (Ruelland 2020; Song et al. 2022; Zhao et al. 2022). Higher regional TLR changes the temperature gradient, resulting in the change of snow/ice melt rates. These melting rate changes further alter surface albedo, creating a positive feedback loop that amplifies warming trends within the basin (Zeitz et al. 2021). In contrast, a lower regional TLR will have the opposite effect, potentially slowing down snow/ice melt rates (Zeitz et al. 2021). Also, factors like inversions and cold air pooling pose a substantial challenge to this quantification (Rolland 2003; Petersen and Pellicciotti 2011; XM Li et al. 2022). Limitations of these assumptions are evident, particularly in regions where lapse rates deviate substantially from conventionally used values (Immerzeel et al. 2014).

The variability of the TLR may be influenced by moisture content, saturation vapour pressure, wind speed, cloud cover, radiation fluxes, albedo, roughness, topography, and aspect of the surface conditions (Marshall et al. 2007; Gardner et al. 2009). Therefore, accurately representing temperature distribution across complex glacierised terrain is critical for climate and glacio-hydrological research (Richard and Gratton 2001; Nigrelli et al. 2018; Azam et al. 2021). Understanding the TLR is a crucial parameter for quantifying elevation-dependent variability in precipitation phase changes, glacier melts, and other cryospheric processes across the region (Immerzeel et al. 2014; Yadav et al. 2019; Singh et al. 2023). However, few studies have found substantial spatio-temporal variations in the TLR across different Himalayan sites, which vary substantially from 0.7 to 11.4 °C km^{-1} (Kattel et al. 2013; Pratap et al. 2013; Heynen et al. 2016; Steiner and Pellicciotti 2016; Pratap et al. 2019a; Yadav et al. 2019).

Despite the crucial role of TLR in understanding high-altitude atmospheric conditions, there is a scarcity of studies specifically investigating this parameter in the western Himalaya. The only study focusing on TLR in this region is on the Sutri Dhaka Glacier catchment using two weather stations (Pratap et al. 2019a). Broader spatial and temporal coverage is needed to capture TLR variability across land surface characteristics. To address this gap, a comprehensive analysis of the TLR is presented over the glacierised terrain of Chandra Basin in the semi-arid zone of western Himalaya. The analysis is based on the observations from five AWS (Campbell Scientific). The study highlights the spatio-temporal variations in the TLR and identifies the key factors driving these variations. Statistical analyses are applied to relate lapse rate variability to meteorological observations of wind speed, relative humidity, and incoming/outgoing shortwave and longwave radiation. An experiment employing a temperature-index model (Hock 2003) is conducted to demonstrate the impacts of TLR variability on glaciers surface mass balance. This experiment provides valuable insight into the control of TLR for the surface mass balance of the Chandra Basin glaciers. The overarching goal is to improve the physical understanding of temperature variability in complex high mountain topography and its implications for glacio-hydrological modeling across the data sparse region of high Himalayas.

3.2 Temperature Lapse Rate (TLR) study

This study uses data collected during a common observation period of five AWSs (A1-A5) established across the Chandra Basin from 2020 to 2022 (Table 3.1). The measurement range of the air temperature sensor (HC2S3) spans from -50 ºC to +60 ºC. It provides highly accurate temperature measurements with a precision of ±0.1 ºC within its operating range.

Table 3.1. List of AWS locations, along with their respective altitudes and periods of observation.

AWSs name	Altitude (m a.s.l.)	Common observation period (dd-mm-yyyy)
A1	4052	03-10-2020 to 14-10-2020 29-10-2020 to 10-10-2022
A2	4244	01-10-2020 to 30-09-2022
A3	4513	07-10-2020 to 30-09-2022
A4	4864	01-10-2020 to 30-09-2022
A5	4904	12-10-2020 to 30-09-2022

The AWS pairs for TLR estimation are A1-A3 (ΔZ 561 m), A1-A4 (ΔZ 812 m), A1-A5 (ΔZ 852 m), A2-A3 (ΔZ 269 m), A2-A4 (ΔZ 620 m), A2-A5 (ΔZ 660 m), A3-A4 (ΔZ 351 m), and A3-A5 (ΔZ 391 m) (Section 3.3.1).

3.3 Results and discussion

3.3.1 Air temperature at Chandra Basin

The Indian summer monsoon is active over the Chandra Basin between June and September, and the mid-latitude westerlies from December to February, resulting in notable air temperature fluctuations. Figure 3.1 depicts the hourly, daily, and monthly observed air temperature variations during the common study period starting from October 2020 till September 2022. The air temperature exhibits a strong seasonal pattern with significant daily and hourly fluctuations at all five sites (Figure 3.1). For both hydrological years, substantial variability is observed in the maximum, minimum, and mean values of air temperature at A1 (14.7, -24.4, -2.0 °C), A2 (12.4, -17.6, -1.4 °C), A3 (12.8, -19.5, -2.5 °C), A4 (10.2, -20.9, -3.7 °C) and A5 (11.5, -22.2, -5.0 °C), respectively. The observed air temperature maximum at each AWS occurs in late August, whereas the minimum occurs in late January (Figure 3.1). During winter, air temperature remains consistently below 0 °C at all AWS locations, whereas in the summer, it is always above the melting point (Figure 3.1).

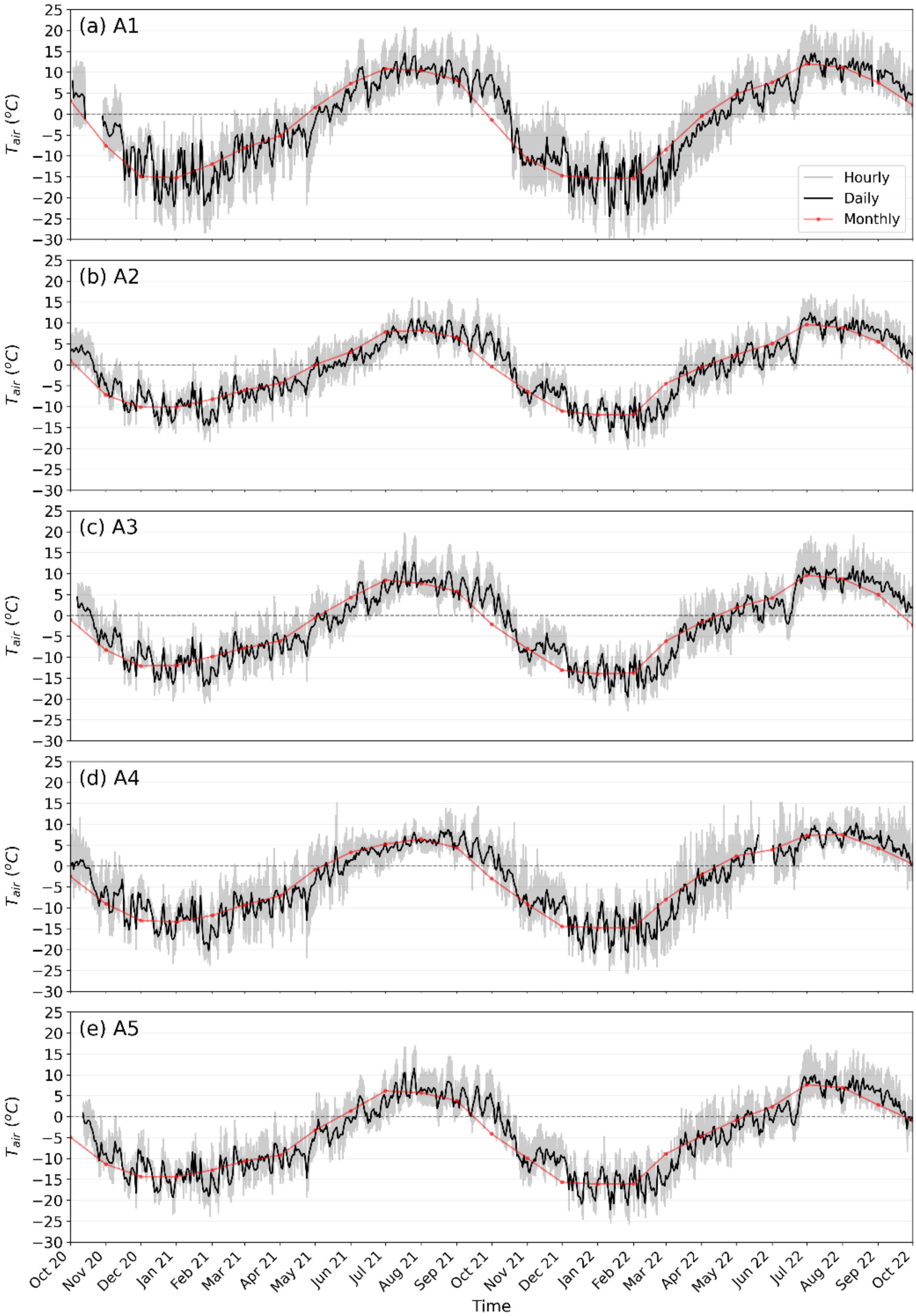

Figure 3.1. Observed monthly (red line), daily (black line) and hourly (gray line) air temperature (Tair) (ºC) data values for AWS sites **(a)** A1, **(b)** A2, **(c)** A3, **(d)** A4, and **(e)** A5 for the study period from October 2020 to September 2022.

Figure 3.2 shows the monthly observed air temperature variation for the study period from October 2020 to September 2022. In winter, the mean monthly air temperature varies between -15.3 ºC and 0.56 ºC, with a mean of -8.59 ºC at All AWS locations. In contrast, during the summer, the mean monthly air temperature ranges from 2.79 ºC to 12.58 ºC, with an overall mean of 5.56 ºC. Over the analyzed two hydrological years, the mean annual air temperature ranges between -5 and -2 ºC for all AWS locations. The elevations of A4 and A5 are similar (ΔZ 40 m), however, there is a significant difference in the corresponding temperatures. Station A4 is situated on the Sutri Dhaka Glacier, which is a glacier environment. The glaciers tend to exhibit different temperatures compared to non-glacier surfaces at similar elevations (Pepin et al. 2015). On the other hand, station A5 is located on barren land at a high mountain pass. This area experiences prolonged snow cover throughout the year and is surrounded by several clean-type glaciers. Therefore, the temperature at A5 site consistently remains significantly lower compared to temperatures recorded at other observed stations. The difference can be attributed to the contrasting surface characteristics, valley effects and local climatic factors affecting these locations. The surface characteristics are glacier/non-glacier, snow cover, barren land, soil moisture, and surface roughness, which significantly influence near-surface temperatures, even at similar elevations (Lookingbill and Urban 2003). Additionally, the valley effect also plays a role in temperature variations over short horizontal distances (Minder et al. 2010; Cullen and Marshall 2011). The gray shaded area in Figure 3.2 depicts the air temperature inversion period. This happens because the air near the surface cools faster than the air above it when the wind is calm. The temperature inversion during the winter (December to February) primarily occur due to the katabatic wind (Figure 3.3) and radiative cooling occurring at low elevations (such as valleys that are sheltered from the wind) (Shen et al. 2016; Sun et al. 2022). At A1 station wind flows from the south-southeast during the summer (Figure 3.3a). While during winter, the wind blows from the north-northeast, and indicates a dominant downwind (Figure 3.3b).

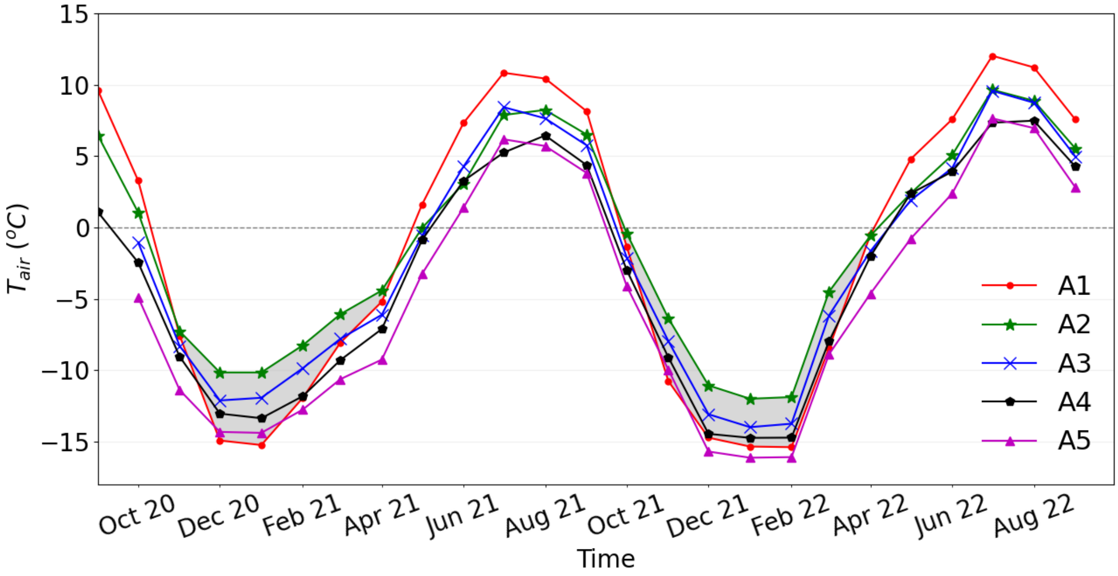

Figure 3.2. Monthly air temperature (T_{air}) (ºC) for all five AWS sites for A1, A2, A3, A4 and A5 for the study period from October 2020 to September 2022. The gray shaded area highlights the air temperature inversion.

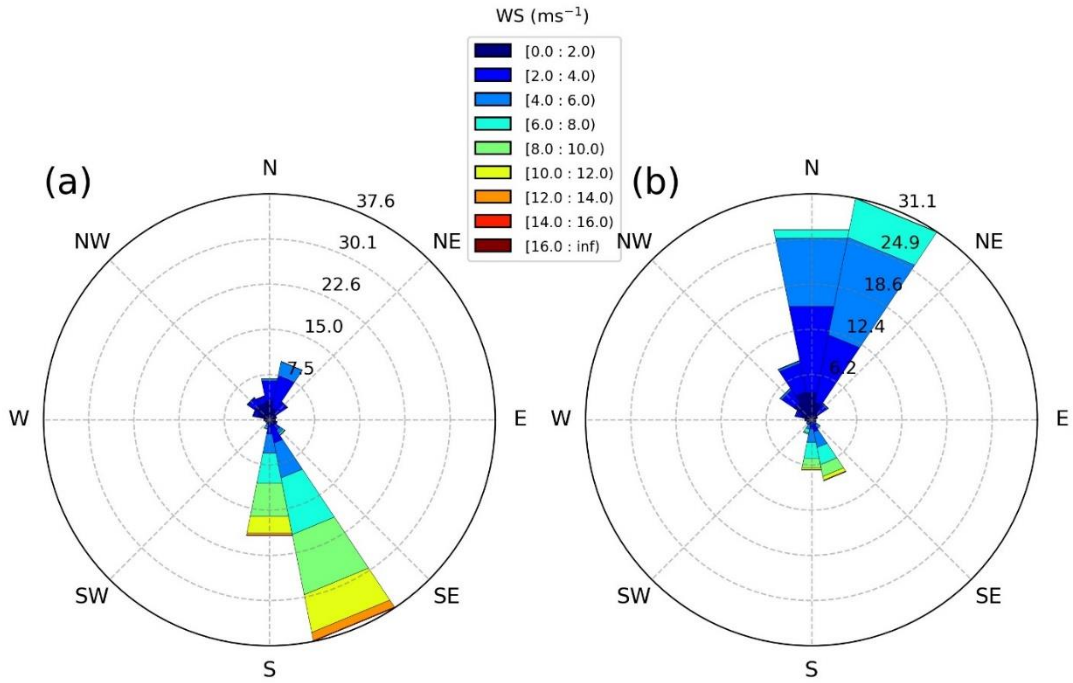

Figure 3.3. Wind speed and directions at A1 AWS during **(a)** summer and **(b)** winter for study period from October 2020 to September 2022. The frequency of wind directions is expressed as percentage over the observational period (indicated on the radial axes).

3.3.2 Temporal variations in TLR

This study focuses on AWS data collected during a common observation period from October 2020 to September 2022 for improved consistency in comparing TLR at all stations. For convenience, the regional meteorology for the Chandra Basin is classified into two seasons, i.e., winter (1st October to 30th April) and summer (1st May to 30th September) (Oulkar et al. 2022).

3.3.2.1 Annual variations

Over the observation period, the mean annual TLR varies from 1.6 ± 0.3 to 6.4 ± 0.4 °C km^{-1} for all station pairs (Table 3.2). The overall estimated mean TLR of 3.8 ± 0.3 °C km^{-1} is significantly less than the standard environmental lapse rate (i.e., 6.5 °C km^{-1}). However, the mean annual TLR (6.4 ± 0.4 °C km^{-1}) for the A3-A5 station closely matches the standard environmental lapse rate and remains similar throughout the year (Table 3.2). This consistency can be attributed to the stability of the atmospheric conditions and the overall balance between heating and cooling processes.

Table 3.2. Seasonal and annual mean of temperature lapse rate (TLR) (°C km^{-1}).

TLR	A1-A3	A1-A4	A1-A5	A2-A3	A2-A4	A2-A5	A3-A4	A3-A5	Mean
Summer	5.8±0.2	4.6±0.1	5.7±0.1	0.9±0.3	2.2±0.1	3.7±0.1	3.1±0.2	5.6±0.2	4.4±0.2
Winter	0.5±0.1	-1.6±0.1	2.3±0.1	6.3±0.2	4.6±0.1	6.6±0.1	3.3±0.2	6.8±0.2	3.6±0.1
Annual	1.6±0.3	2.4±0.2	3.9±0.2	3.7±0.6	4.2±0.3	5.5±0.2	3.3±0.5	6.4±0.4	3.8±0.3

3.3.2.2 Seasonal and monthly variations

Monthly variations in the TLR show large variability across different seasons in the catchment throughout the study period (Figure 3.4). During summer, the mean TLR across all station pairs ranges from 0.9 ± 0.3 to 5.8 ± 0.2 ºC km^{-1}, with an overall mean of 4.4 ± 0.2 ºC km^{-1} (Table 3.2). The highest TLR is observed during summer, characterized by warm and humid conditions. However, it is found that the values of TLR for the station pair A2-A3 and A2-A5 show an opposite trend, potentially due to the presence of cold air pools and thin air (Figure 3.4) (Minder et al. 2010). There is considerable intra-seasonal variation in the TLR between stations during the summer months of both hydrological years, indicating a diversity of weather conditions throughout each summer. These findings agree with previous studies conducted for the station pair A1-A4 catchment (Pratap et al. 2019a). Furthermore, the estimated TLR results during the summer season align well with other studies conducted in different regions of the Himalaya (Fujita and Ageta 2000; Immerzeel et al. 2014; Kattel et al. 2015; Heynen et al. 2016; Yadav et al. 2019). This deviation can be attributed to variations in elevation, topography, and surface characteristics of the study sites. In addition, the wide valleys of the Chandra Basin could be snow-free during the summer, contributing to almost uniform temperature distribution between these station pairs except for the A4 station over the glacier. The TLR is greatly influenced by various meteorological variables such as relative humidity, wind speed, and radiation fluxes (see section 4.3). These meteorological variables are higher in the summer, advancing air movement at higher elevations during saturated adiabatic conditions (DeScally 1997). Even during summer, the TLR between stations A3-A5 remains remarkably consistent. In our study, the A5 at an elevation of 4904 m a.s.l., experiences snow cover for a more extended period cover compared to the lower elevation areas, which may contribute to stable atmospheric conditions. During June to August, the Chandra Basin glaciers exhibit the highest TLR with a mean of 5.8 ± 0.2 °C km^{-1}. This shows an indication of a higher melting pattern under warm and humid conditions. Pratap et al. (2019a) also reported similar results of higher surface melting for the Sutri Dhaka Glacier from 2015 to 2017. Similarly, a study by Oulkar et al. (2022) also revealed higher surface melting during the same period.

The mean TLR across all station pairs during winter ranges from -1.6 ± 0.1 to 6.8 ± 0.2 ºC km^{-1}, with an overall mean of 3.6 ± 0.1 ºC km^{-1} (Table 3.2). Since, the Chandra Basin experiences heavy precipitation (snowfall) during winter due to the western disturbances (Bookhagen and Burbank 2006), it can result in the area being covered by dense clouds cover. In these conditions, moisture-laden winds move upward along the upslope areas (Marshall et al. 2007; Shen et al. 2016). The flow of cold air above the ground restricts temperature exchange between lowlands and higher elevations, resulting in atmosphere subsidence and longwave cooling of the surface temperature, which further contributes to strong inversion (Shen et al. 2016; Sun et al. 2022). Additionally, heavy precipitation alters the surface conditions at lower elevations, decreasing near-surface temperature. This leads to a strong inversion in air temperature (Figure 3.2), which results in negative TLR during the winter season at the station pair A1-A3, A1-A4 and A1-A5 (Figure 3.4). The significantly more negative TLR (-5.1± 0.2 ºC km^{-1}) which occur during December-January can be attributed to low air temperature at A1 station (Figure 3.2). However, TLR values observed at the station pairs A2-A3, A2-A4, A2-A5, A3-A4, and A3-A5 are positive, ranging from 2.4 ± 0.1 to 7.9 ± 0.2 ºC km^{-1}, consistent with previous study (Yadav et al. 2019). In contrast to the summer, heat exchange and moisture influx developments, influenced by the orographic uplift of air masses, are mostly lacking in the winter. During winter, the air temperature is around or below the freezing point across the region (Figure 3.2). The upslope area is covered by snow, which substantially enhances emissivity in clear and dry sky environments. As a result, the cooling effect occurs due to the longwave radiation reduction. Previous research in the Himalayan region has also highlighted a similar relationship between meteorological variables and TLR during winter (Kattel et al. 2013; Immerzeel et al. 2014).

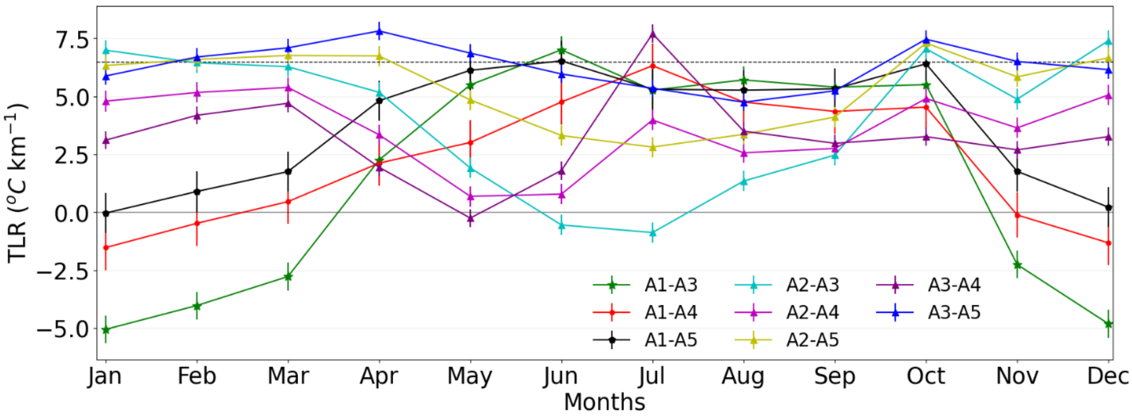

Figure 3.4. Mean monthly temperature lapse rate (TLR) (ºC km^{-1}) for the year from October 2020 to September 2022, for station pairs A1-A3, A1-A4, A1-A5, A2-A3, A2-A4, A2-A5, A3-A4, and A3-A5.

3.3.2.3 Diurnal cycle

The mean diurnal variation of TLR for station pairs A1-A4, A2-A4, and A3-A5 exhibit relatively consistent patterns with minimal fluctuation across seasonal and annual timescales (Figure 3.5). The A3-A5 station pair TLR values closely match the standard environmental lapse rate, likely due to stable atmospheric conditions and an overall balance of heating and cooling processes (Minder et al. 2010; Shen et al. 2016). The A1-A4 and A2-A4 station pairs show slightly lower values than the standard lapse rates during the summer. However, in winter, the A1-A4 station pair exhibits sub-zero values (below 0 °C km^{-1}) (Figure 3.5), indicating temperature inversions occur near station A1 (Figure 3.2). The consistency of the lapse rates suggests stability in atmospheric dynamics while the winter inversion highlights deviations potentially caused by local topography and weather patterns (Minder et al. 2010).

In contrast, the station pairs A1-A3, A1-A5, A2-A3, A2-A5, and A3-A4 demonstrate pronounced day-to-day fluctuations in the estimated mean diurnal TLR across seasonal and annual timescales (Figure 3.5). This variability depends highly on the specific location and is influenced by a range of factors including radiation fluxes, cloud cover, moisture, local surface characteristics, wind speed and direction, snow/ice melting, refreezing, and sublimation (Gardner et al. 2009; Petersen and Pellicciotti 2011). The lapse rate exhibits high temporal variability for these station pairs. More negative values tend to occur during late night to early morning hours (20:00 to 09:00 hrs). The negative diurnal TLR at night may be attributed to the absence of shortwave radiation, leading to a weaker heat exchange process between locations. This could also be attributed to the cooling effects of the overnight period, where radiative heat loss dominates (Minder et al. 2010). Whereas, positive lapse rates are observed from late mornings to late evenings (10:00 to 18:00 hrs). These time intervals often experience the strongest influence of solar radiation, leading to convective processes, enhanced vertical mixing and rapid changes in temperature with altitude. This pattern persists consistently throughout the seasons and the entire year, highlighting the specific time intervals (11:00 to 17:00 hrs) when the diurnal temperature fluctuation is most pronounced. The diurnal variation in the TLR is primarily influenced by the warming effect of incoming solar energy during the daytime and the cooling effect of outgoing longwave radiation during the nighttime (Bhutiyani et al. 2007; Brock et al. 2010; Petersen and Pellicciotti 2011; Immerzeel et al. 2014; Heynen et al. 2016; Steiner and Pellicciotti 2016). This fluctuation highlights an instability in atmospheric dynamics between these station pairs. The temperature profiles vary considerably over short time frames, deviating substantially from the standard environmental lapse rate. Similar findings are reported by Kattel et al. (2013) in the southeastern Tibetan Plateau and the eastern Himalaya.

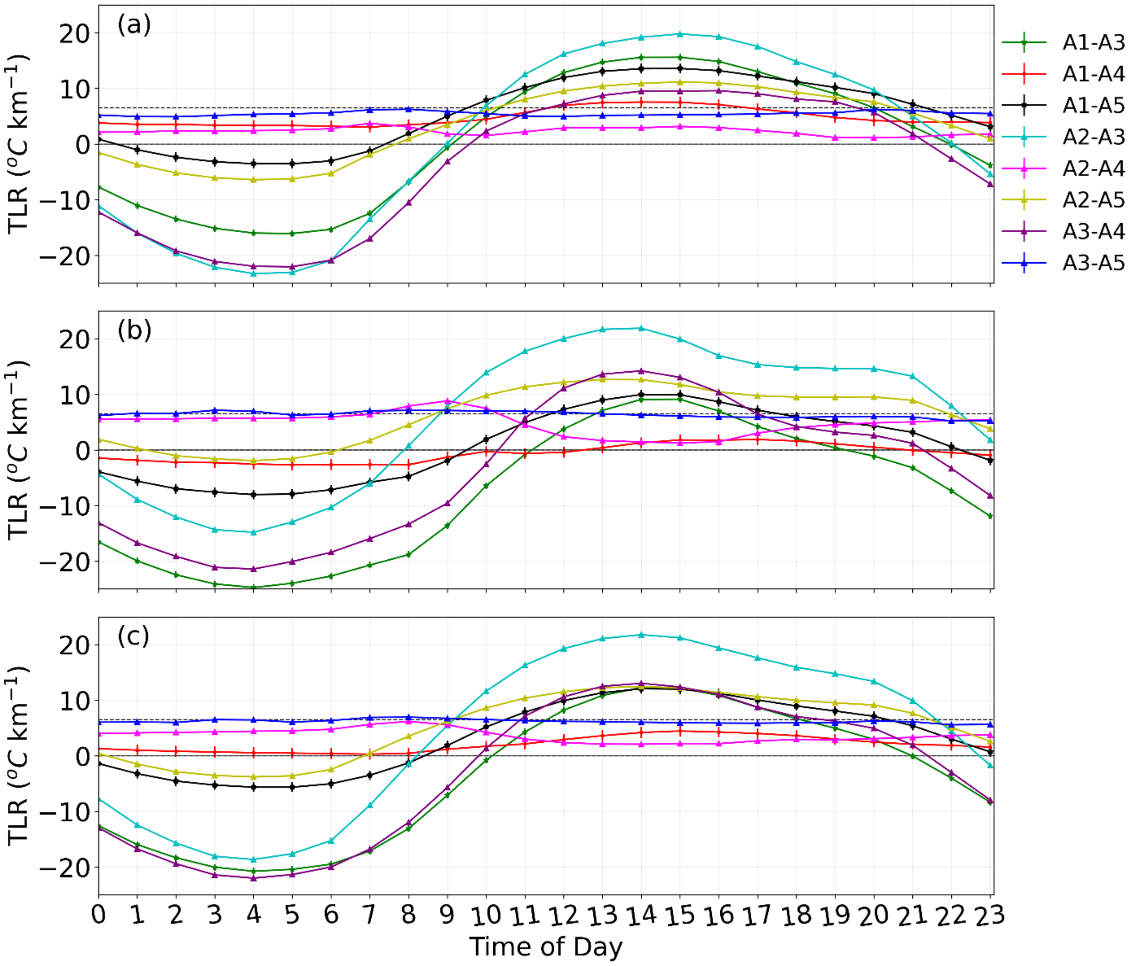

Figure 3.5. The mean diurnal cycle of temperature lapse rate (TLR) (ºC km^{-1}) for **(a)** summer, **(b)** winter and **(c)** annual for station pairs A1-A3, A1-A4, A1-A5, A2-A3, A2-A4, A3-A5, A3-A4 and A3-A5.

3.3.3 Relationship between TLR and meteorological variables

The TLR is controlled by several climatic factors. Figure 3.6 depicts the mean monthly variation of TLR, air temperature, wind speed, relative humidity, and incoming/outgoing shortwave and longwave radiation during the study period from October 2020 to September 2022. The mean monthly values of these meteorological variables within the Chandra Basin follow similar seasonal trends, with higher values in the summer and lower in the winter (Figure 3.6). However, the mean monthly outgoing shortwave radiation shows an opposite pattern, with higher values during winter when snow cover is extensive across the Chandra Basin, and lower values in summer when the AWSs area are snow free. Additionally, the mean monthly wind speed recorded at station A1 exhibits higher velocities in winter compared to other seasons (Figure 3.6).

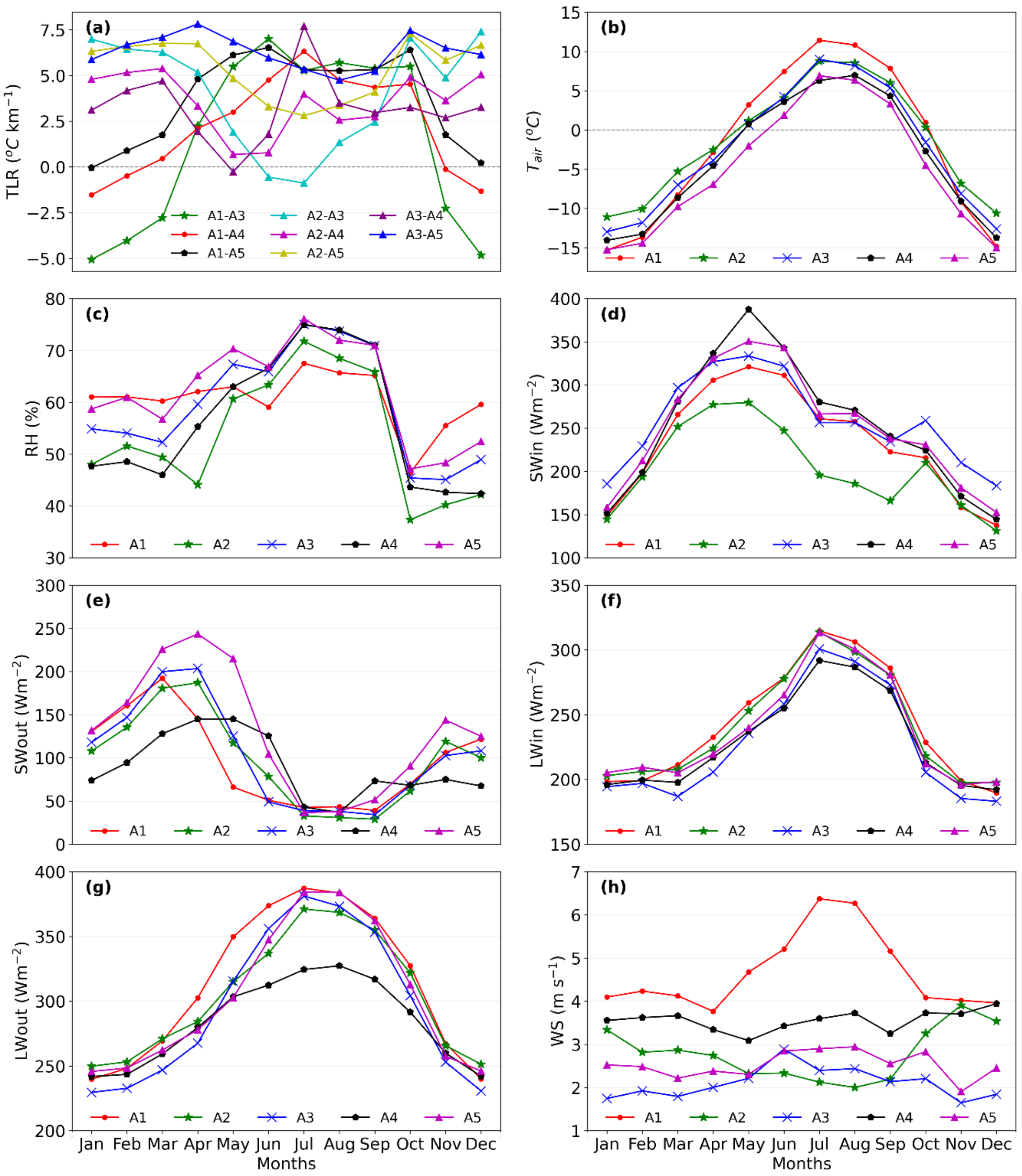

Figure 3.6. Mean monthly temperature lapse rate and meteorological variables for the study period. **(a)** temperature lapse rate (TLR, ºC km^{-1}), **(b)** air temperature (Tair, ºC), **(c)** relative humidity (RH, %), **(d)** incoming shortwave radiation (Sin, Wm^{-2}), **(e)** outgoing shortwave radiation (Sout, Wm^{-2}), **(f)** incoming longwave radiation (LWin, Wm^{-2}), **(g)** outgoing longwave radiation (LWout, Wm^{-2}), and **(h)** wind speed (WS, m s^{-1}). The A1, A2, A3, A4 and A5 are Automatic Weather Stations (AWS).

To further demonstrate the relationship between the TLR and climatic factors, the correlations between the TLR and the meteorological variables are examined (Figure 3.7). This analysis involves calculating the correlation for both the mean monthly (Figure 3.7a) and diurnal (Figure 3.7b) TLR with the corresponding overall mean of the meteorological variables. The mean monthly TLR for the station pairs A1-A3, A1-A4 and A1-A5 shows a strong positive correlation with all the meteorological variables (air temperature, wind speed, relative humidity, incoming shortwave radiation, incoming/outgoing longwave radiation) except for outgoing shortwave radiation, which has a significantly negative correlation (Figure 3.7a). Similar findings are reported by Sun et al. (2022) in the southeastern Tibetan Plateau and the eastern Himalaya. The relative humidity and TLR values for A1-A3, A1-A4, and A1-A5 station pairs have similar seasonal trends, with higher values in the summer and lower values in the winter (Figure 3.6a,c). During summer, increased solar heating and convective activity lead to higher temperatures, which can hold more moisture, resulting in higher relative humidity (Figure 3.6b,c,d). At the same time, the stronger surface heating during summer creates higher temperature differences between higher and lower elevations, leading to a higher TLR (Figure 3.6a). In contrast, during winter, lower temperatures and reduced convective activity result in lower relative humidity (Figure 3.6c) and a lower TLR due to strong inversion in air temperature (Figure 3.2, Figure 3.6a). This seasonal variation of relative humidity and TLR leads to a strong positive correlation at the monthly scale (Figure 3.7a). Furthermore, during the winter, the presence of snow cover results in a higher surface albedo, leading to increased outgoing shortwave radiation (Figure 3.6e). In contrast, during the summer season, the snow cover typically melts, resulting in a lower surface albedo and decreased outgoing shortwave radiation (Figure 3.6e). Therefore, we observe strong negative correlation between outgoing shortwave radiation and TLR at the monthly scale (Figure 3.7a). However, for the station pairs A2-A3, A2-

A4 and A2-A5, the mean monthly TLR has a strong positive correlation only with wind speed and outgoing shortwave radiation, while with the remaining meteorological variables, the correlation is highly negative (Figure 3.7a). A strong negative correlation between relative humidity and TLR is observed, which is inconsistent with the previous study (Shen et al. 2016). Furthermore, for station pair A3-A4, the mean monthly TLR does not fluctuate significantly, and therefore, no significant correlation can be determined (Figure 3.6a, Figure 3.7a). Additionally, the mean monthly TLR for station pair A3-A5 does not show a significant correlation with the meteorological variables (Figure 3.6, Figure 3.7a).

The mean diurnal TLR for the station pairs A1-A3, A1-A4, A1-A5, A2-A3 and A2-A4 shows a strong positive correlation with all the meteorological variables (air temperature, wind speed, incoming/outgoing shortwave and longwave radiation) except for relative humidity, which has a significantly negative correlation (Figure 3.7b). For the station pairs A1-A3, A1-A4, and A1-A5, the relationship between relative humidity and TLR is opposite. During the daytime, increased surface heating and turbulent mixing create a higher TLR due to more efficient heat transfer from lower to higher elevations (Whiteman 2000). Whereas, during the night, the atmosphere is more stable, with weaker turbulent mixing and less efficient heat transfer between elevations. This results in a lower TLR (Figure 3.6a). Therefore, the higher TLR values occur during the daytime when relative humidity is lower, leading to a strong negative correlation between TLR and relative humidity (Figure 3.7b). Further, the positive correlation between outgoing shortwave radiation and TLR can be attributed to the simultaneous effects of surface heating, albedo differences between elevations, atmospheric stability and mixing processes, which collectively result in higher TLR and higher outgoing shortwave radiation during the daytime (Qu et al. 2014; Pepin et al. 2022). The diurnal variation of the TLR follows an inversely proportional trend to the relative humidity which could be attributed to factors related to radiative cooling, turbulent mixing, and cloud cover (Shen et al. 2016; Sun et al. 2022). The TLR for station pair A2-A3 does not correlate significantly with the wind speed. However, for the station pairs A2-A4, A2-A5 and A3-A4, some of the meteorological variables have a positive correlation with the mean diurnal TLR, and some are negative (Figure 3.7b). This may be influenced by regional topography and weather patterns. Additionally, the mean diurnal TLR for station pair A3-A5 does not show significant correlation with the meteorological variables (Figure 3.7b). These findings are consistent with previous studies conducted across diverse regions (Bhutiyani et al. 2007; Brock et al. 2010; Petersen and Pellicciotti 2011; Immerzeel et al. 2014; Heynen et al. 2016; Steiner and Pellicciotti 2016).

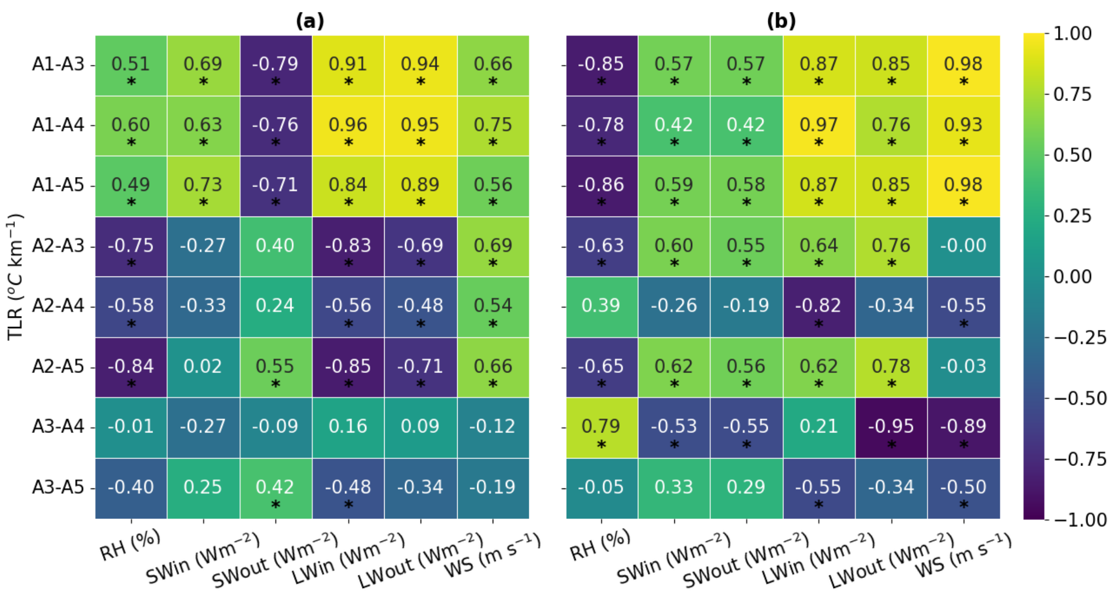

Figure 3.7. Correlation between **(a)** mean monthly and **(b)** mean diurnal temperature lapse rate (TLR) (ºC km^{-1}) and corresponding meteorological variables over the study period. The meteorological variables are relative humidity (RH, %), incoming shortwave radiation (Sin, Wm^{-2}), outgoing shortwave radiation (Sout, Wm^{-2}), incoming longwave radiation (LWin, Wm^{-2}), outgoing longwave radiation (LWout, Wm^{-2}), and wind speed (WS, m s^{-1}). Here, * indicates that the correlation is significant at p value < 0.01 level.

3.3.4 Application of TLR for mass balance modeling

TLR is one of the essential parameters for glacio-hydrological studies, particularly glacier mass balance modeling. Here, a comprehensive investigation of the importance of observed TLR on the mass balance over the Chandra Basin glaciers is conducted using the temperature index model (Section 3.3). The analysis has certain limitations associated with parameters (including precipitation factor and DDF, specifically for a single glacier (Figure 3.10) that are not calibrated and are beyond the scope of the study. The analysis predominantly focuses on the mass balance sensitivity to TLR changes.

Figure 3.10 shows the annual mass balance of the glaciers over the Chandra Basin for seven hydrological years (2015 to 2022). The air temperature data obtained from the A1 station, incorporating a constant TLR of 6.5 °C km^{-1} is used for seven hydrological year annual mass balance. The mass balance of the Chandra Basin glaciers has predominantly experienced a negative mean annual mass balance (Figure 3.10). However, our findings reveal a large difference between the estimated mass balance and the results of previous studies on glacier mass balance within the basin (Figure 3.10, Table 3.3) (Gardelle et al. 2013; Vijay and Braun 2016; Tawde et al. 2017; Mandal et al. 2020; Sharma et al. 2020; Patel et al. 2021; Oulkar et al. 2022; Chandrasekharan and Ramsankaran 2023). Therefore, a sensitivity analysis is conducted by varying the TLR used in the model from the constant value of 6.5 °C km^{-1} to values within the observed range of TLR at the study site (3.0 to 7.5 °C km^{-1}) (Figure 3.4). The modeled mass balance is found to be highly sensitive to changes in TLR within this observed range. A change in TLR of 3.0 °C km^{-1} resulted in a 74 % more negative mean annual mass balance estimate compared to using the constant 6.5°C km^{-1} TLR. Conversely, a TLR of 7.5 °C km^{-1} resulted in a 36 % less negative mean annual mass balance estimate. Overall, across the observed TLR range, the mean annual mass balance sensitivity is 0.3 m w.e. a^{-1} per unit TLR (°C km^{-1}) change. The sensitivity analysis undertaken in this study provides quantitative evidence of the magnitude of errors that could arise from assuming a constant environmental TLR in the region.

Table 3.3. The glaciers mass balance studies in the Chandra Basin using different methodologies.

MB Method	Region	Mass Balance (m w.e. a^{-1})	Year	Reference
Geodetic	Chandra Basin	−0.47 ± 0.50	1989-2020	Chandrasekharan and Ramsankaran (2023)
Energy balance	Sutri Dhaka	−0.82 ± 0.21	2015-2017	Oulkar et al. (2022)
Energy balance	Eight glaciers	–0.59 ± 0.12	2013-2018	Patel et al. (2021)
Glaciological	Five glaciers	−0.57 ± 0.12	2013-2017	Sharma et al. (2020)
Glaciological	Chhota Shigri	−0.46 ± 0.40	2002-2019	Mandal et al. (2020)
Geodetic	Chandra Basin	−0.61 ± 0.46	1984-2012	Tawde et al. (2017)
Geodetic	Chandra Basin	−0.65 ± 0.43	2000-2012	Vijay and Braun (2016)
Geodetic	Chandra Basin	−0.68 ± 0.15	1999-2011	Gardelle et al. (2013)

Our results highlight the importance of employing the measured variability in TLR when assessing glacier mass balance, emphasizing the need for accurate and site-specific TLR estimations. Furthermore, the non-linear temperature gradient due to inversions needs to be considered in models while extrapolating the temperature distribution at a regional scale. This study demonstrates strong biases while employing constant environmental lapse rates in several studies over the Himalayan region. The study suggests the critical importance of the TLR measurements in the glacio-hydrological research over the Himalaya.

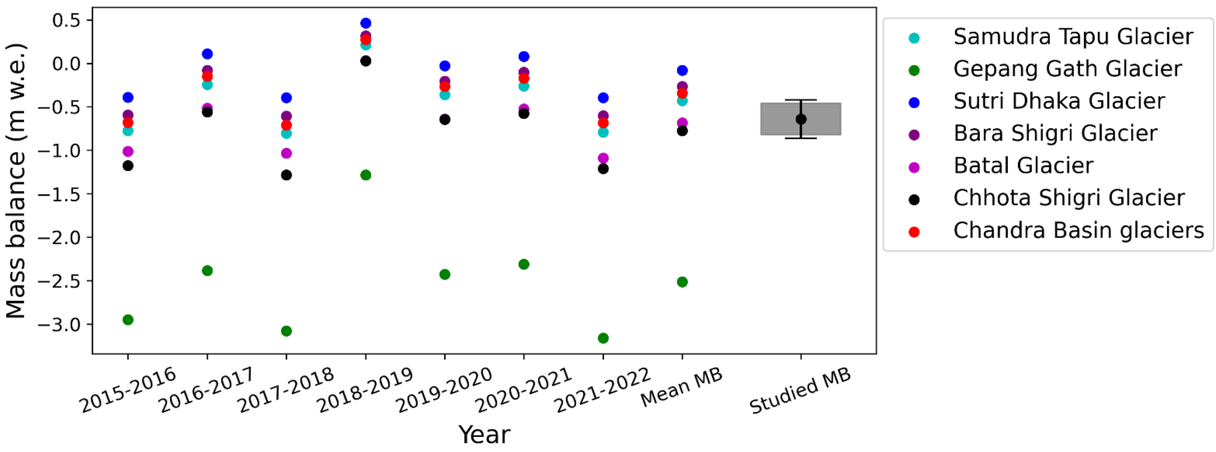

Figure 3.8. Estimated mass balance over the Chandra Basin glaciers for seven hydrological years (2015 to 2022) using the temperature index model, with the shaded gray rectangle representing mass balance values reported in published studies (Table 3.3) of the region. The analysis includes only 6.5 °C km^{-1} air temperature lapse rate (TLR).

Chapter 4

4 Energy fluxes, mass balance and climate sensitivity of Sutri Dhaka Glacier in the western Himalaya

4.1 Introduction

Several studies have demonstrated the substantial loss of glacier ice mass, resulting in rapid retreat of the Himalayan glaciers in the recent decades (Kulkarni et al. 2007; Bolch et al. 2012; Brun et al. 2017; Kumar et al. 2019; Shean et al. 2020). On a regional scale (western, central and eastern Himalaya), the glaciers have shown enhanced thinning during the past decade except for the Karakoram and adjacent regions (Kaab et al. 2012; Gardelle et al. 2013; Farinotti et al. 2020). However, due to the remoteness and high-altitude terrain of Himalayan glaciers, in-situ hydrometeorological measurements are limited to very few glaciers (Pratap et al. 2016; M Azam et al. 2018; Kumar et al. 2018; Azam et al. 2019; WGMS 2019). Thus, the relationship between atmospheric forcing and glacier mass change in the Himalaya is poorly understood. Therefore, it is essential to understand the response of glaciers to atmospheric forcing using hydrometeorological observations and numerical models. Although an empirical temperature index model (Hock 2003) is convenient for modeling glacier mass balance using air temperature (T_{air}) and precipitation, this simple model does not track the energy fluxes. The energy balance model approach, which considers different energy fluxes interacting with glaciers, is considered to be very effective for simulating the distributed mass balance of glaciers and are also valuable for detailed sensitivity studies of glacier mass balance (Oerlemans and Reichert 2000; De Woul and Hock 2005; Li et al. 2019).

Within the Himalaya, the Western Disturbance (WD) and the Indian Summer Monsoon (ISM) are the dominant sources of precipitation and significantly affect the mass balance of the glaciers (Shekhar et al. 2010; Azam et al. 2014a). While WD plays a dominant role in determining glacier behavior in the western Himalaya, the ISM plays more important role in the central and eastern Himalaya. The WDs mainly contributes to the winter precipitation events in the upper Indus Basin, which are driven by the approaching extra-tropical, synoptic-scale disturbances (Dimri et al. 2015; Philippe et al. 2021). One of the major sub-basins of the upper Indus basin is the Chandra Basin, which lies in the transition zone of WD and ISM (Bookhagen and Burbank 2006). Since the Chandra River is passing through a semi-arid zone, its water budget is highly sensitive to the melting of snow and glaciers. With the recent increases in extreme events of precipitation and increasing temperature, the Chandra Basin provides an ideal testbed to understand the status and climate sensitivity of glaciers from western Himalaya.

In order to understand the spatio-temporal variability in surface energy and mass balance, it is important to undertake integrated studies using in-situ measurements and by employing energy balance models that can simulate the distributed mass balance. Towards this, the Sutri Dhaka Glacier from the upper Chandra Basin, a relatively large (~20 km^2) and debris-free glacier is examined during two contrasting meteorological years using field data and a well-constrained physically-based 'COupled Snowpack and Ice surface energy and MAss balance model (COSIMA)' (Huintjes et al. 2015). The model is forced with meteorological data obtained from an on-glacier automatic weather station (AWS). The model is calibrated with meteorological and glaciological data from point locations and then use the model to simulate the mass balance for the entire glacier. This study allows us to assess the mass balance sensitivity of the Sutri Dhaka Glacier to different atmospheric variables and investigate the importance of snow-to-rain conversion during warmer years in amplifying the temperature sensitivity of the mass balance.

4.2 Study site: Sutri Dhaka Glacier

The Sutri Dhaka Glacier is the third largest glacier of the upper Chandra Basin (Figure 4.1). It covers an area of ~20 km^2, with a length of ~10.7 km along a north-east orientation. It is a debris-free glacier with only 5% of the ablation area covered with thin debris (Sharma et al. 2016). The glacier elevation ranges from 4500 m a.s.l. at the snout to 6000 m a.s.l. at the bergschrunds with an average slope of ~10º (Pratap et al. 2019b).

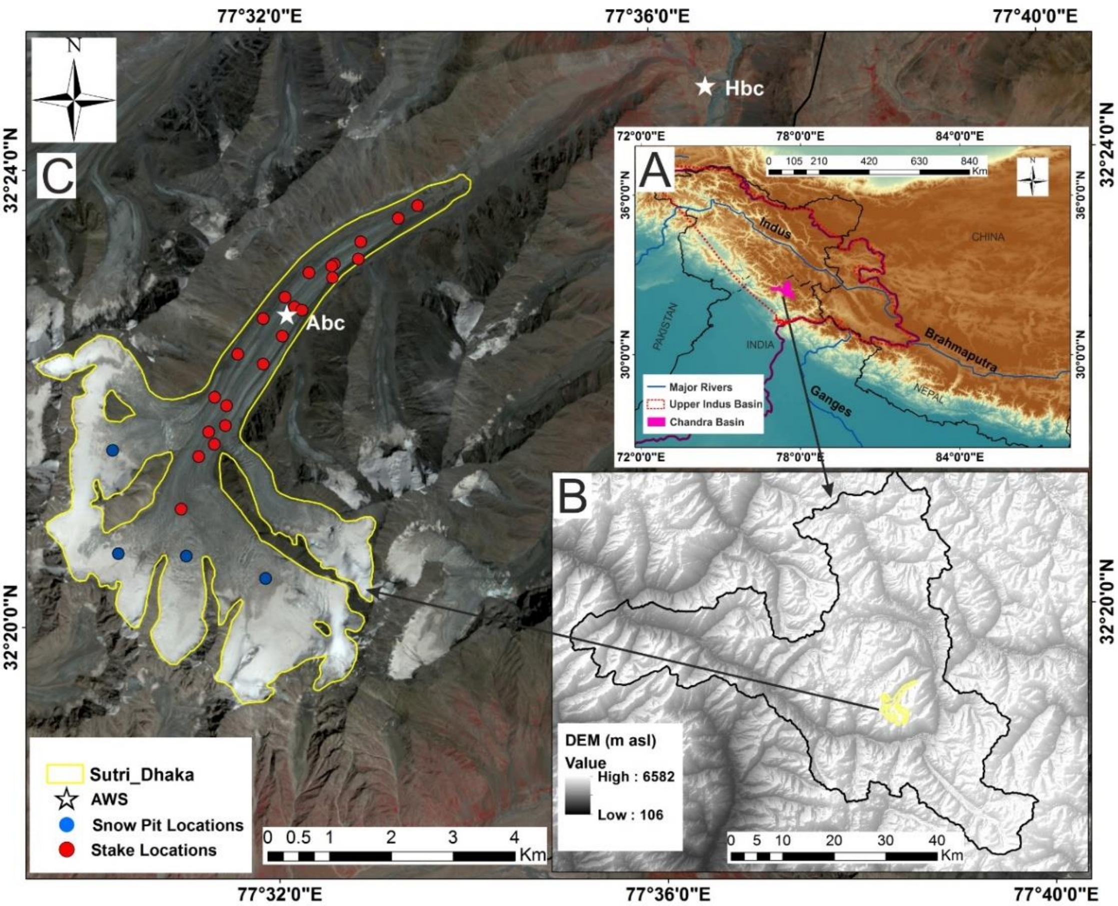

Figure 4.1. Location map **(A)** of the study region in the western Himalaya, **(B)** the Chandra Basin **(C)** the Sutri Dhaka Glacier (yellow outline) with the location of two AWS A1 (Hbc, 4052 m a.s.l.) and (white stars) located at A4 (Abc, 4864 m a.s.l.). The red dots represent the ablation stakes installed, and the blue dots are accumulation pit locations.

4.3 Observation period and data processing

Two AWS systems have been operating at Sutri Dhaka Glacier catchment since October 2015 (Figure 4.1C). One AWS is situated on the glacier surface in the upper ablation zone at Advance base camp (A4 AWS, 4864 m a.s.l.), while the other one is located on the open ground in the same catchment at the HIMANSH base camp (A1 AWS, 4052 m a.s.l.) (Figure 4.1C). The distance between A1 and A4 AWS is 8 km, with an altitudinal difference of 812 m. This study uses AWS data collected during a observation period from October 2015 to September 2017.

There is a brief data gap during the 2017 summer, as the AWS at A4 AWS stopped functioning from 25th to 30th June owing to the power cut. The data gap in T_{air} and relative humidity at A4 AWS are filled with linearly extrapolated data from the station A1 AWS using a lapse rate (Table 4.1). Additionally, hourly net shortwave (S_{net}) radiation, net longwave (L_{net}) radiation, wind speed and albedo data are obtained from the European Centre for Medium-Range Weather Forecasts (ECMWF) reanalysis (ERA5) at the nearest surface grid points of A4 AWS and used to fill the data gap using bias correction. Due to the malfunctioning of the precipitation sensor at A4 AWS, only A1 AWS precipitation data is used for analysis. Further, air pressure data at an hourly resolution is obtained from the ERA5 for the nearest surface level at the two-point location of A4 AWS. It is corrected from the ERA5 pixel elevation to the on-glacier site A4 AWS using the air pressure lapse rate. Cloud cover for the study region is estimated based on L_{net} and T_{air} following the procedure by Van den Broeke et al. (2006), which calculates a quantitative cloud cover fraction estimate ranging between 0 and 1.

The mean annual lapse rates are calculated with the observed meteorological data obtained from A1 AWS, A4 AWS and ERA5 data (Table 4.1). The monthly T_{air} lapse rate of the catchment ranges from -0.0003 to -0.0065 °C m^{-1}, with a mean of -0.0042

°C m^{-1}. The monthly relative humidity lapse rate varied from 0.009 to 0.016 % m^{-1} (mean 0.012 % m^{-1}). The monthly air pressure gradient calculated from grid points of ERA5 data nearest to the two AWS, ranged from -0.026 to -0.049 hPa m^{-1} (mean -0.034 hPa m^{-1}). For the observation period from October 2015 to September 2017, at all stake points, the estimated mass balance is calibrated using various precipitation gradient values and use the lowest root mean square error (RMSE) between modelled and measured mass balance. The precipitation gradient is derived from the model calibration process. The precipitation gradient value used in the study is 0.12 % m^{-1} (Figure 4.2)

Table 4.1. The mean annual altitudinal gradient/lapse rates calculated from A1 AWS, A4 AWS and ERA5 for extrapolation of data.

Variables	**Altitudinal gradient**
Elevation (m a.s.l.)	4500-6000
Air temperature lapse rate (°C m^{-1})	-0.0042
Precipitation gradient (% m^{-1})	0.12
Air pressure gradient (hPa m^{-1})	-0.034
Relative humidity lapse rate (% m^{-1})	0.012

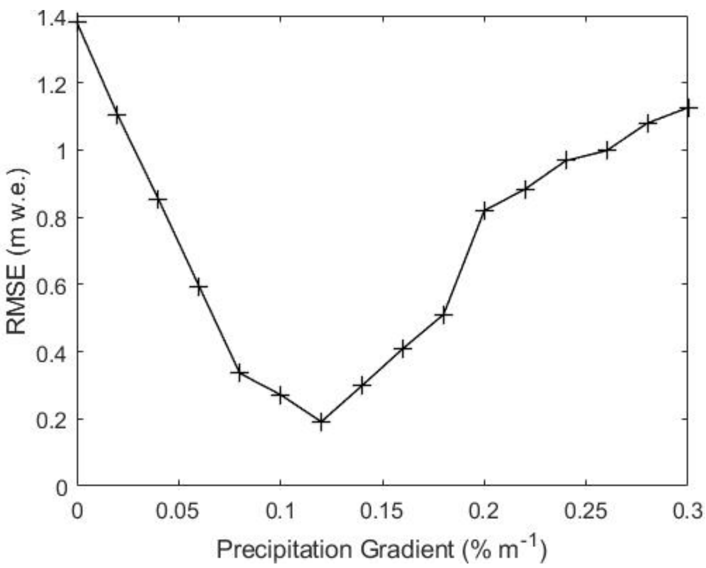

Figure 4.2. The root mean square error (RMSE) between observed and modelled mass balance (m w.e.) versus precipitation gradient (% m^{-1}).

A digital elevation model (DEM) with a spatial resolution of 30 m obtained from the Advanced Spaceborne Thermal Emission and Reflection Radiometer (ASTER) Global Digital Elevation Model Version 2 (GDEM V2) from Earth Remote Sensing Data Analysis Centre (ERSDAC) (Tachikawa 2011) is resampled bilinearly to a 45 m grid resolution. Based on the gradient (precipitation and air pressure) and lapse rate (T_{air} and relative humidity), the meteorological data is extrapolated at the grid points of the resampled 45 m DEM to obtain distributed surface energy and mass balance of the Sutri Dhaka Glacier (Table 4.1).

4.4 Model uncertainty using Monte Carlo simulations for Sutri Dhaka Glacier

The model uncertainty is estimated using the Monte Carlo simulations (van der Veen 2002). The model uncertainty is estimated based on repeated modelling of the mass balance at all observed point locations on Sutri Dhaka Glacier. The mass balance uncertainty of 100 simulations is evaluated using standard deviation. It is found that the difference between the observed and the modelled mass balance is within the range of uncertainty of 100 simulations (Figure 4.3). The overall uncertainty of modelled mass balance is ±25%.

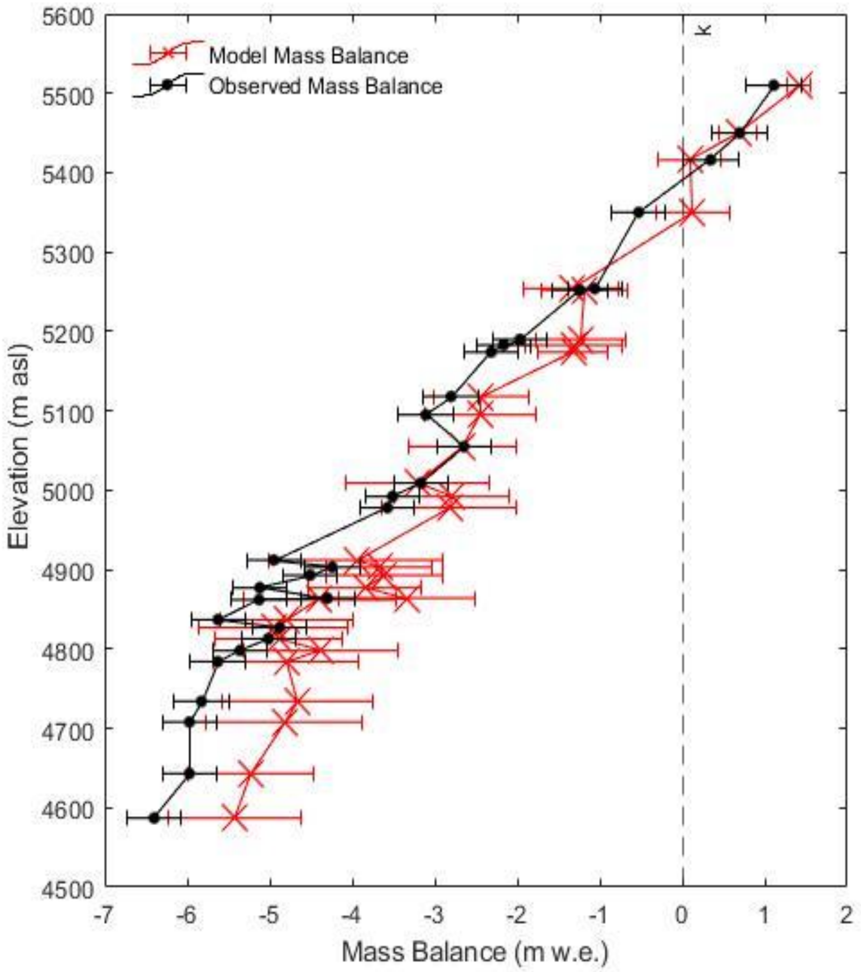

Figure 4.3. The observed and modelled mass balance (m w.e.) with uncertainty.

4.5 Results

4.5.1 Meteorological conditions at the Sutri Dhaka catchment

The meteorological data for the two balance years (2015/16 and 2016/17) obtained from the on-glacier site A4 AWS are shown in Figure 4.4. Over the study period, daily T_{air} varied from 10.0 to -22.4 ºC (Figure 4.4A). The mean values are -4.6 and -4.4 ºC for the balance years 2015/16 and 2016/17, respectively. Whereas, the daily surface temperature varied from 0 to -31.9 ºC with the mean values of -11.0 (2015/16) and -9.6 ºC (2016/17) (Figure 4.4B). The daily mean T_{air} is above 0°C between early June and the end of September. Data shows that January is the coldest month and August is the warmest month in this glacierized basin, in agreement with other studies on nearby glaciers (Azam et al. 2014a). During summer, surface temperature remains close to the melting point in agreement with consistently positive T_{air} (Figure 4.4A,B). Daily relative humidity varied from 4% to 92%, with mean values of 56% (± 16%) (Figure 4.4C). The area is characterized by a warm summer with high relative humidity from June to September and a cold winter season, comparatively less humid, from December to February. The daily mean wind speed varied between 1.2 and 8.5 m s^{-1} with a mean speed of 3.6 m s^{-1} (± 1 m s^{-1}) (Figure 4.4D). The observed wind direction during the study period is mostly downslope, with a maximum speed of 13.5 m s^{-1}, suggesting predominately katabatic flow with modest strength over the glacier. The winter period is characterized by high wind speed with larger variability (± 1.2 m s^{-1}), whereas in the summer, the wind speed is comparatively less varied (± 0.5 m s^{-1}) (Figure 4.4D). The mean daily values of S_{in} varied from 84 to 403 Wm^{-2} in summer and 30 to 385 Wm^{-2} in winter for both the balance years (Figure 4.4E). The annual mean is 248 and 223 Wm^{-2} for the balance years 2015/16 and 2016/17, respectively (Figure 4.4E). Summers are characterized with intense solar heating, whereas winters are associated with cold, dry, and windy conditions due to low sun elevation and strong westerlies. The variation of L_{in} in the summer is 178 to 324 Wm^{-2}, and in the winter, it is 112 to 306 Wm^{-2} for both the balance years (Figure 4.4F). The annual mean is 223 Wm^{-2} and 227 Wm^{-2} for the balance year 2015/16 and 2016/17, respectively (Figure 4.4F). During the summer, higher L_{in} can be associated with cloudy days, whereas, during the winter its variability is higher which can be due to significant fluctuation in cloud conditions. At the on-glacier site A4 AWS, albedo ranges between 0.20 and 0.98, with a mean value of 0.35 (2015/16) and 0.41 (2016/17) (Figure 4.4G). The A4 AWS location exhibited a higher mean albedo in winter (0.74) than in summer (0.31) due to the contrasting surface conditions of fresh snow versus glacier ice, respectively. The annual precipitation is 567 mm and 710 mm for the balance years 2015/16 and 2016/17, respectively. In both the balance years (2015/16, 2016/17), higher precipitation occurred during winter (60%, 80% respectively) than summer (40%, 20% respectively) (Figure 4.4H).

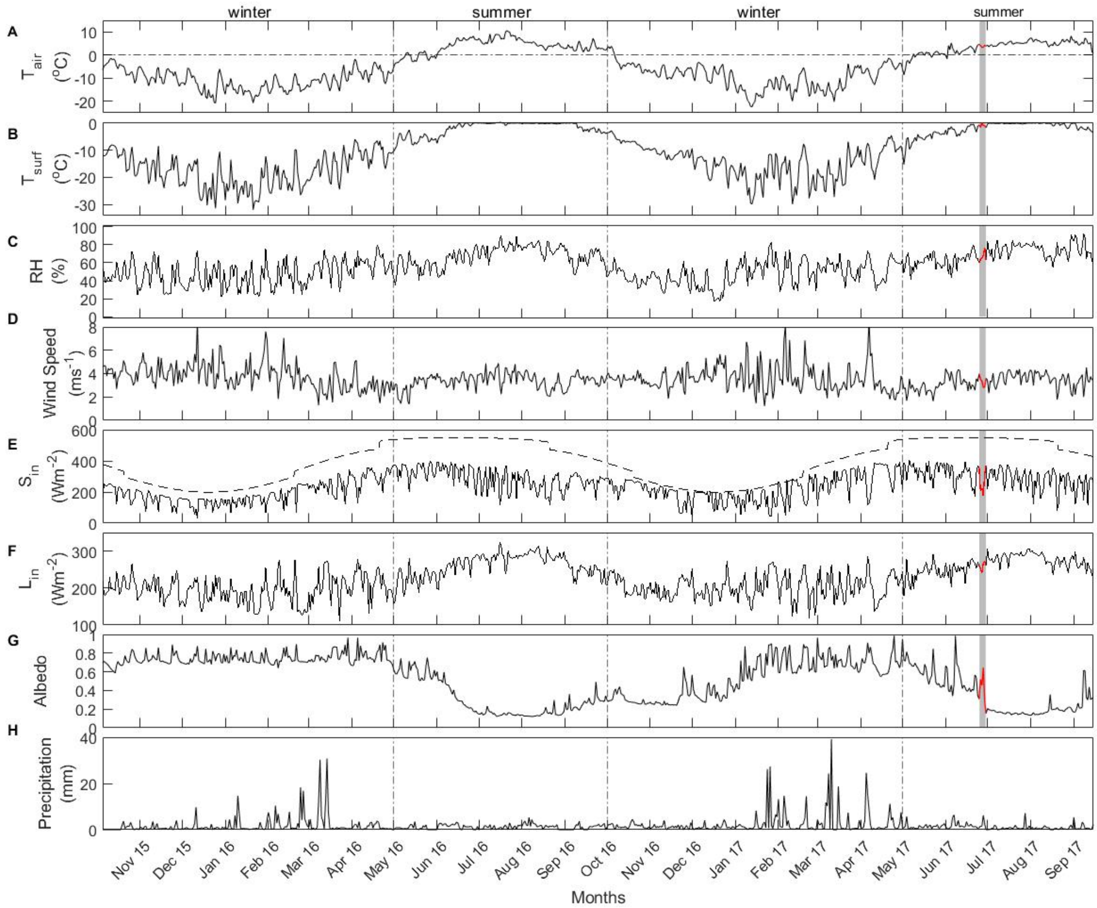

Figure 4.4. Observed daily mean values of **(A)** air temperature ($\boldsymbol{T_{air}}$) (ºC), **(B)** surface temperature ($\boldsymbol{T_{surf}}$) (ºC), **(C)** relative humidity ($\boldsymbol{RH}$) (%), **(D)** wind speed (m s^{-1}), **(E)** incoming shortwave ($\boldsymbol{S_{in}}$) radiation (Wm^{-2}), **(F)** incoming longwave ($\boldsymbol{L_{in}}$) radiation (Wm^{-2}), **(G)** albedo, and **(H)** total precipitation (mm) over the Sutri Dhaka Glacier at the site A4 AWS, for study period from October 2015 to September 2017. The gray shaded areas indicate the interval when meteorological variables (A to G) at the A4 AWS site is estimated using the A1 AWS and ERA5 data. Dashed line in (E) indicates Top of the Atmosphere (TOA) solar irradiance.

4.5.2 Model calibration

The COSIMA 1D model is used to assess the efficiency at several sites where calculations are done for one grid point, providing a quick and efficient technique to test the model performance (Huintjes et al. 2015). Initially, a set of observed hourly meteorological data are used as input data to run the COSIMA 1D model at the A4 AWS site (Figure 4.1C) for the period from 4th October 2015 to 15th September 2017. Further, the 1D model results are evaluated against the observed surface temperature, L_{net}, and albedo. Within the model, the initial temperature profile is simulated linearly between air and surface temperature; correspondingly, the surface roughness is determined based on fresh snow, aged snow, and ice (Molg and Scherer 2012). For the parameterization and initial conditions of surface albedo, the approach of Oerlemans and Knap (1998) is used, as shown in equation 4. These estimated variables (surface temperature, L_{net}, and albedo) obtained from the 1D model are compared with the observed A4 AWS data. A strong correlation is found between the modelled and observed A4 AWS data for surface temperature (r=0.96; n=712, mean absolute error=1.15 ºC), L_{net} (r=0.92; n=712, mean absolute error=20.59 Wm^{-2}), and albedo (r=0.89; n=712, mean absolute error=0.09) for the period from 4th October 2015 to 15th September 2017 (Figure 4.5).

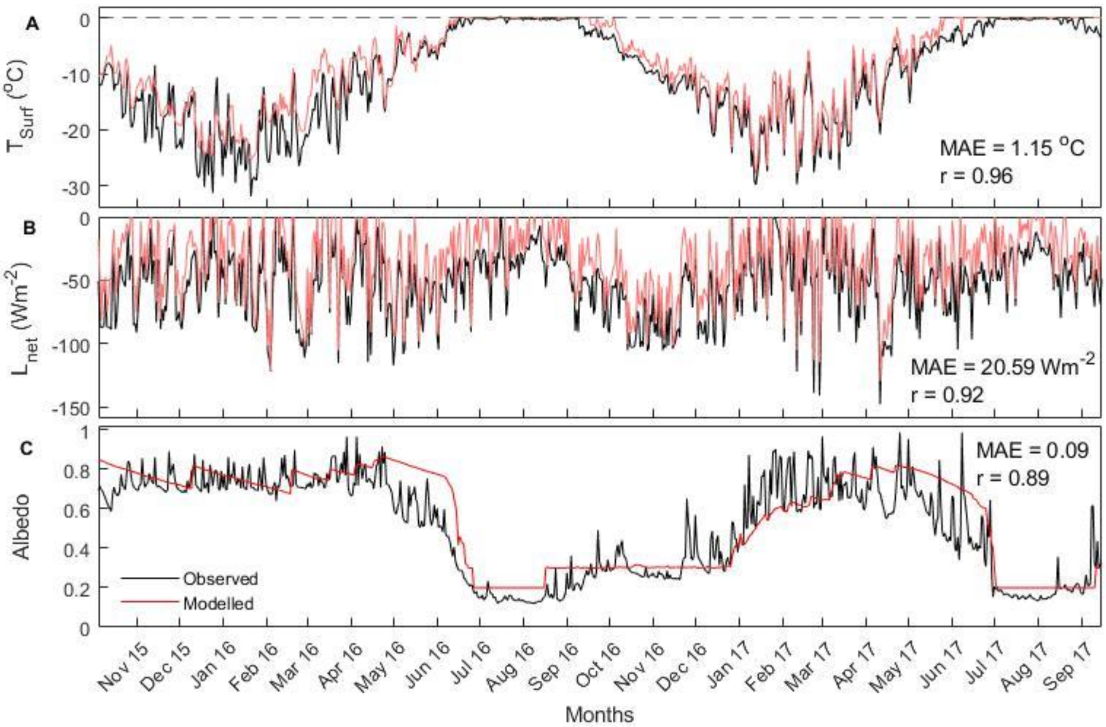

Figure 4.5. Observed (black) and modelled (red) daily mean values of **(A)** surface temperature (T_{surf}) (ºC), **(B)** net longwave (L_{net}) radiation (Wm^{-2}), and **(C)** albedo with their correlation coefficient at the A4 AWS site for the Sutri Dhaka Glacier from October 2015 to September 2017.

The observed mass balance for the nearest ablation stake (~5m from A4 AWS site, 4863 m a.s.l.) is -4.30 ± 0.33 and -3.59 ± 0.33 m w.e. and the calibrated modelled surface mass balance at A4 AWS site is -3.98 ± 0.99 and -3.34 ± 0.84 m w.e. for the balance year 2015/16 and 2016/17, respectively. Further, the observed annual balances (point-wise) is plotted with the modelled annual balance at the corresponding grid location (Figure 4.6). The coefficient of determination (R^2) between the simulation and the measurement for the surface mass balance is 0.97 (RMSE=0.38 m w.e.) for 2015/16 and 0.98 (RMSE=0.58 m w.e.) for 2016/17, respectively (Figure 4.6). The modelled (observed) annual mass balance gradient between 4500 and 5500 m a.s.l. is 0.8 (0.87) m w.e. $(100\ m)^{-1}$ and 0.79 (0.9) m w.e. $(100\ m)^{-1}$ for the balance year 2015/16 and 2016/17, respectively. Overall, the model has an excellent ability to simulate the mass balance processes of Sutri Dhaka Glacier and performed well for the study period from 4th October 2015 to 15th September 2017.

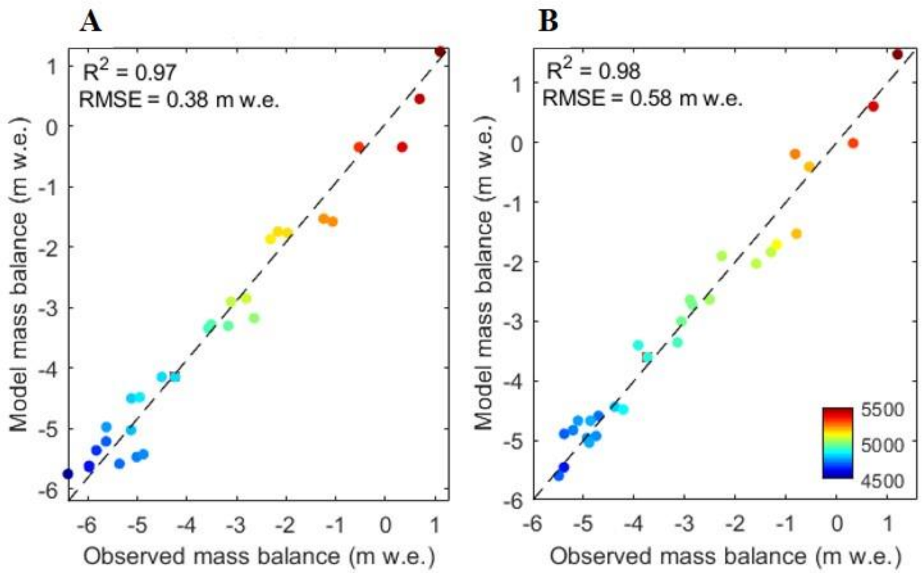

Figure 4.6. The comparison of observed and modelled mass balance (m w.e.) at Sutri Dhaka Glacier for two contrasting meteorological years **(A)** 2015/16 and **(B)** 2016/17.

4.5.3 Surface energy balance

4.5.3.1 Distributed surface energy balance

The simulated spatial variability of S_{net} and L_{net}, the turbulent heat fluxes (H_{se} and H_{la}), albedo and Q_{G} averaged over two balance years (2015/16 and 2016/17) is shown in Figure 4.7. The results obtained by the COSIMA 2D model show that mean S_{net} ranges from 20 to 200 Wm^{-2} (Figure 4.7A) and varies with altitude, where the S_{net} decreases as the mean albedo increases (Figure 4.7A, B). The mean L_{net} flux varied from -120 to -70 Wm^{-2} and decreased with the altitude (Figure 4.7C). The turbulent heat fluxes of H_{se} and H_{la} both showed maximum values over the lower ablation zone (Figure 4.7D, E). High values at the lower parts and decreasing values with increasing altitude can be explained by the temperature gradient against elevation. The modelled longwave radiation and turbulent heat fluxes depend mainly on T_{air} and relative humidity as a function of altitude (Klok and Oerlemans 2002; Molg et al. 2009). Simulated Q_G heat flux is mainly a function of surface temperature and topographic characteristics, therefore, it is lowest in the accumulation area (Figure 4.7F), where the surface temperature is minimum.

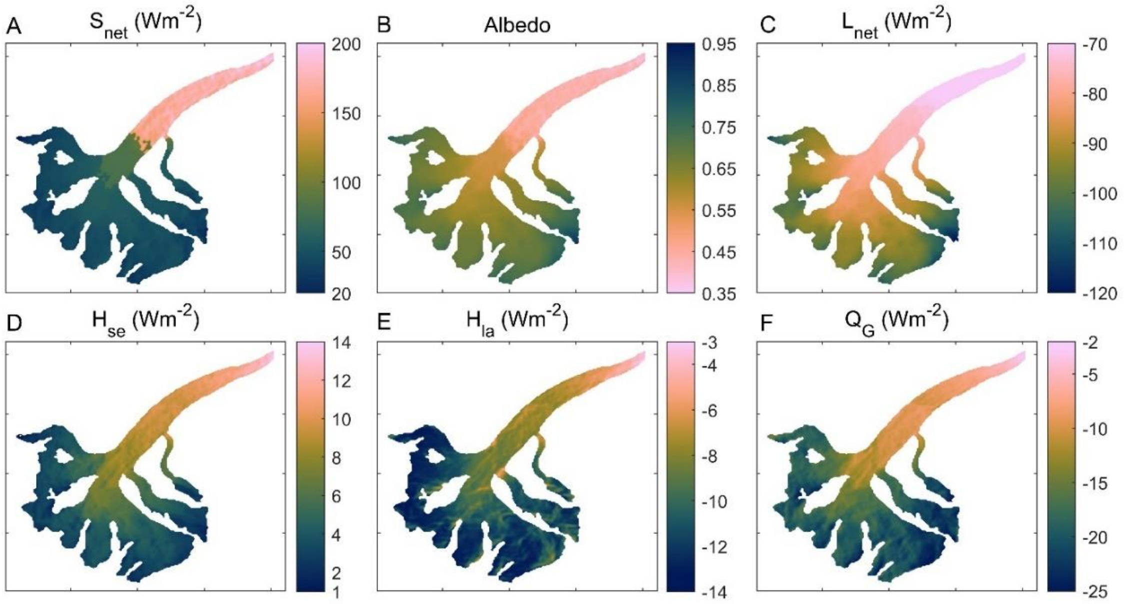

Figure 4.7. Spatial distribution of modelled mean surface energy fluxes for Sutri Dhaka Glacier over two balance years 2015/16 to 2016/17. **(A)** net shortwave (S_{net}) radiation,

(B) albedo, **(C)** net longwave (L_{net}) radiation, **(D)** sensible heat flux (H_{se}), **(E)** latent heat flux (H_{la}), **(F)** ground heat flux (Q_{G}).

4.5.3.2 Seasonal and annual contribution of energy fluxes

The accumulation and ablation area of the glacier is demarcated based on the observed mean ELA (5300 m a.s.l.). The contribution of energy fluxes is separately estimated for accumulation, ablation and glacier-wide zone based on the simulation (Figure 4.8 and Figure 4.9) In the accumulation and ablation zones surface energy exchanges happen due to distinct climatic characteristics (Wu et al. 2016).

In the accumulation zone, the mean energy fluxes during winter (2015/16 and 2016/17) is predominantly governed by outward L_{net} (Figure 4.8). The outward flux contribution is higher than the inward flux, which suggested that the cooling effect is dominant. Whereas, during summer, it is primarily contributed by inward S_{net}, and outward L_{net} (Figure 4.8). The total energy increased the temperature of the snowpack; however, the available energy only marginally exceeded the cold content of the snowpack. Throughout the study period, in the accumulation zone, higher contributions of outward H_{la} and Q_{G} heat flux suggests that there is maximum cooling effect. In the ablation zone of the glacier, during winter (2015/16 and 2016/17), the mean energy fluxes are primarily contributed by inward S_{net} and outward L_{net}, whereas, the summers showed dominant contribution by inward S_{net} (Figure 4.8). The S_{net}, accounted for 77% of the total heat flux during summer, resulting in strong summertime melting in the ablation zone of the Sutri Dhaka Glacier.

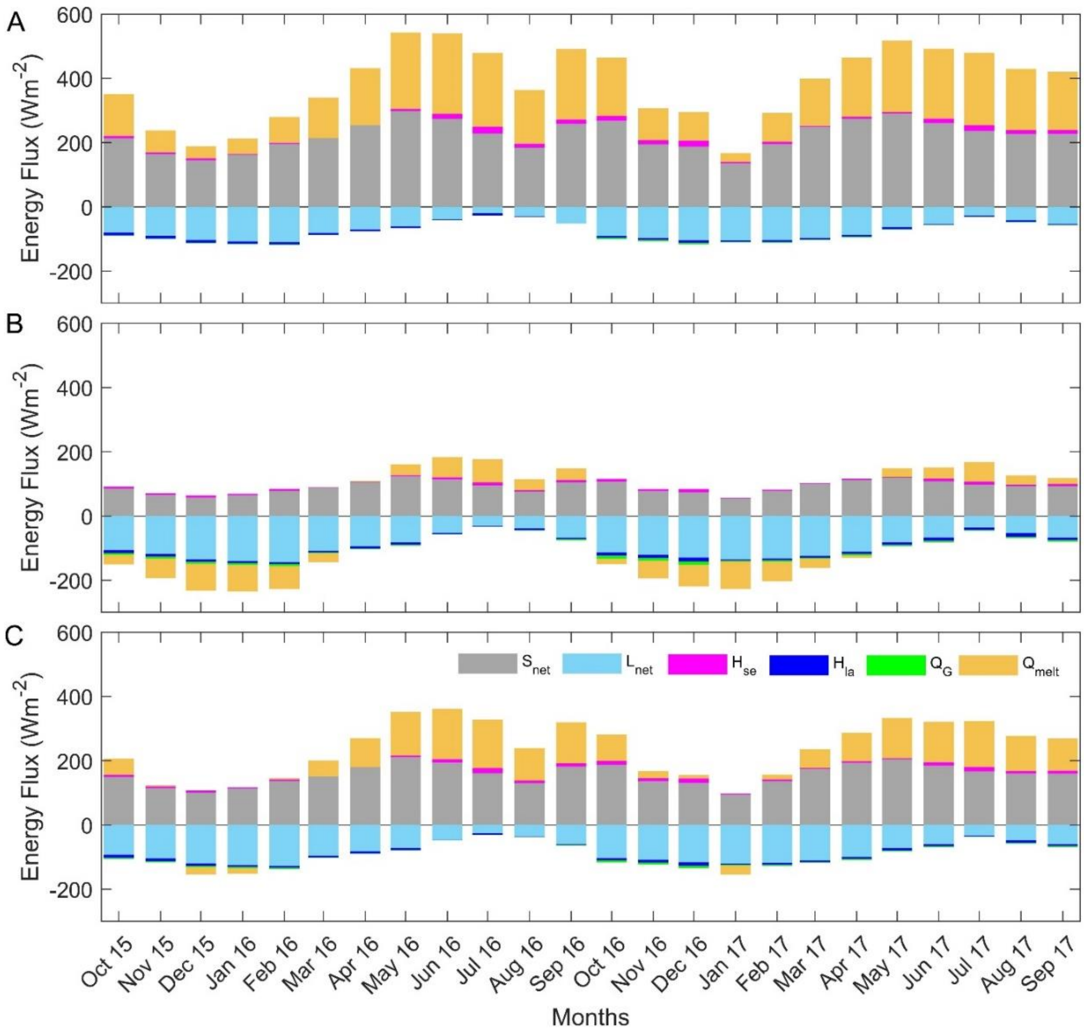

Figure 4.8. The monthly mean surface energy fluxes for **(A)** ablation zone (below 5300 m a.s.l.), **(B)** accumulation zone (above 5300 m a.s.l.) and **(C)** glacier-wide region of Sutri Dhaka Glacier.

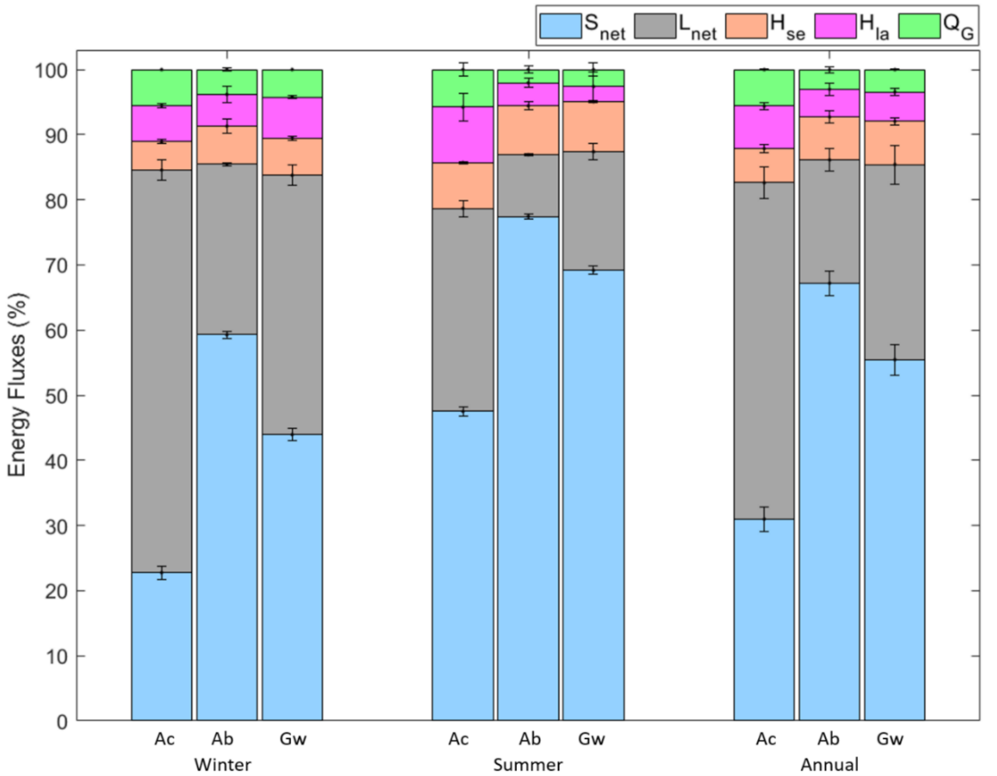

Figure 4.9. The mean seasonal and annual contribution of each energy flux in percentage for **Ac** (accumulation zone, above 5300 m asl), **Ab** (ablation zone, below 5300 m asl) and **Gw** (glacier-wide region) of Sutri Dhaka Glacier. The proportional contribution of each flux is calculated as |flux|/total; where the total is the sum of the energy fluxes in absolute values: $|S_{net}|$+$|L_{net}|$+$|H_{se}|$+$|H_{la}|$+$|Q_G|$.

The glacier-wide mean annual energy flux showed that S_{net} accounted for 56% of the total surface energy fluxes, followed by L_{net} (27%), H_{se} (8%), H_{la} (5%), and Q_{G} (4%) (Figure 4.9 and Table 4.2). The winter budget of S_{net} is mainly determined by albedo, which remains very high as the glacier's surface is covered by snow (winter time mean albedo ~0.74), and this leads to low S_{net} (Figure 4.4G and Figure 4.10). Therefore, the available surface energy (Q_{melt}) is significantly less during winter and this part of the energy source (S_{net}) is compensated collectively by the energy sink of L_{net}, the turbulent heat fluxes (H_{se}+ H_{la}) and Q_{G}. During the summer, S_{net} is the largest source of energy to the glacier surface and mainly controlled the temporal variability of surface melt, as a result, Q_{melt} followed the same oscillation trend as S_{net} (Figure 4.10). The contribution of S_{net} (L_{net}) is slightly high (less), i.e., 7% more in the 2015/16 balance year than in

2016/17. As a result, summertime melting is more intense, with Q_{melt} contributing more in 2015/16 than in 2016/17 (Table 4.4). During summer, clear-sky days with high air and surface temperature gradients are advantageous for H_{se} to heat the glacial surface, resulting in strong summertime melting of the Sutri Dhaka Glacier (Figure 4.10). The negative H_{la} values (Figure 4.10) suggest that the only mass loss during winter is in the form of sublimation. The estimated mass loss due to sublimation, results in a daily mean rate of 0.0013 m w.e. d^{-1}. However, during the summer, H_{la} is positive due to high T_{air} and relative humidity associated with the summer-monsoon circulation, giving rise to deposition at the glacier surface (Figure 4.4A, C and Figure 4.10). Such phenomena have also been reported at the Chhota Shigri Glacier (western Himalaya) and AX010 Glacier (central Himalaya) (Kayastha et al. 1999; Azam et al. 2014b). The energy released from condensation leads to positive H_{la} increasing surface melting during summer (Oerlemans 2000; Giesen et al. 2009). A negative value for $\mathrm{Q_G}$ suggests an increase of subsurface cold content during winter, whereas a positive Q_{G} heat flux implies a decreasing cold content in summer (Figure 4.10).

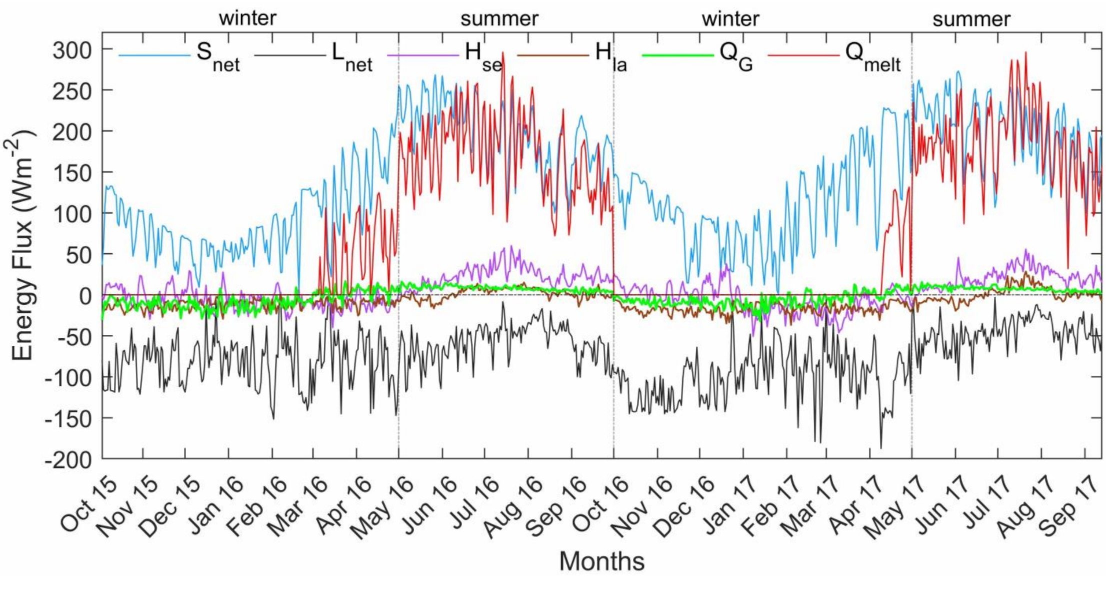

Figure 4.10. Modelled daily mean values of surface energy fluxes at Sutri Dhaka Glacier from October 2015 to September 2017. S_{net} is net shortwave radiation, L_{net} is net longwave radiation, H_{se} is sensible heat flux, H_{la} is latent heat flux, Q_G is ground heat flux and Q_{melt} is the available melt energy flux.

A comparison of surface energy balance of Sutri Dhaka Glacier depicting similarities (and important differences) with other Himalayan glaciers is shown in Table 4.2. As previously observed for Himalayan glaciers (Yang et al. 2011; Zhang et al. 2013; Azam et al. 2014b; N Singh et al. 2018; Patel et al. 2021), the current study also revealed that S_{net} is the predominant source of energy to the glacier surface and primarily determines the temporal variability of melting (Table 4.2). However, L_{net} is the largest energy sink that is substantially influenced by cloudy conditions. It is moderate during the summer, when L_{out} is nearly compensated by maximum L_{in} due to the warm, humid, and cloudy environment, which decreases energy loss at the surface, and high during the winter, when L_{in} is at its lowest.

Table 4.2. Comparison of the characteristics and mean annual surface energy fluxes (Wm^{-2}) for various Himalayan glaciers. Values in square brackets are the % contribution of each energy fluxes.

Glacier	**Sutri Dhaka**	**Chandra Basin glaciers**	**Pindari**	**Chhota Shigri**	**Zhadang**
Region	Western Himalaya	Western Himalaya	Central Himalaya	Western Himalaya	Central Tibetan Plateau
Period of observation	October 2015 to September 2017	October 2013 to September 2019	June 2016 to July 2017	July 2013 to October 2013	October 2009 to September 2011
Altitude (m a.s.l.)	4500-6000	4000 to 6200	3750	4670	5660
Latitude	32.38°N	30.08 to 32.45°N	30.26°N	32.28°N	30.47°N
S_{net}	157 [56]	64 [59]	[62]	–	69 [45]
L_{net}	-85 [27]	-88 [16]	[24]	–	-52 [37]
$R_{\text{net}} = S_{\text{net}} + L_{\text{net}}$	72 [83]	85 [75]	[86]	87 [80]	17 [82]
H_{se}	7 [8]	15 [15]	[12]	31 [13]	14 [10]
H_{la}	-5 [5]	-11 [8]	[2]	11 [5]	-9 [6]
Q_{G}	-3 [4]	- 2 [2]	–	4 [2]	-1 [2]
Reference	Present study	Patel et al. (2021)	N Singh et al. (2018)	Azam et al. (2014b)	Zhang et al. (2013)

4.5.4 Surface mass balance

The modelled distributed surface mass balance values of Sutri Dhaka Glacier revealed significant seasonal and interannual variability, with high positive values during winter and stronger snow/ice mass loss during summer (Table 4.3). The modelled glacier-wide annual balances are -1.09 ± 0.31 and -0.62 ± 0.19 m w.e. during 2015/16 and 2016/17, respectively (Figure 4.11 and Table 4.3). The values matched well with the observed values of -1.16 ± 0.33 and -0.67 ± 0.33 m w.e. during 2015/16 and 2016/17, respectively (Table 4.3). The ice loss is higher in the lower ablation zone and decreased with an increase in altitude. The modelled mean annual mass balance for two balance years is -0.86 ± 0.21 m w.e a^{-1}, which is similar to the mass balance reported by Sharma et al. (2020) based on the field results (-0.82 ± 0.17 m w.e. a^{-1} for 2013-2017). Our findings are also consistent with the study of Patel et al. (2021) that estimated an annual mass balance of -0.74 ± 0.1 m w.e. a^{-1} for Sutri Dhaka Glacier during 2013-2019. However, our estimated mass balance is more negative than the Chhota Shigri Glacier that has a value of -0.46 ± 0.40 m w.e. a^{-1} for the period 2002-2019 (Mandal et al. 2020). The estimated geodetic mass balance for the Chandra Basin is -0.68 ± 0.15 and -0.65 ± 0.43 m w.e. a^{-1} for the periods 1999–2011 and 2000–2012, respectively (Gardelle et al. 2013; Vijay and Braun 2016), which is close to our estimate.

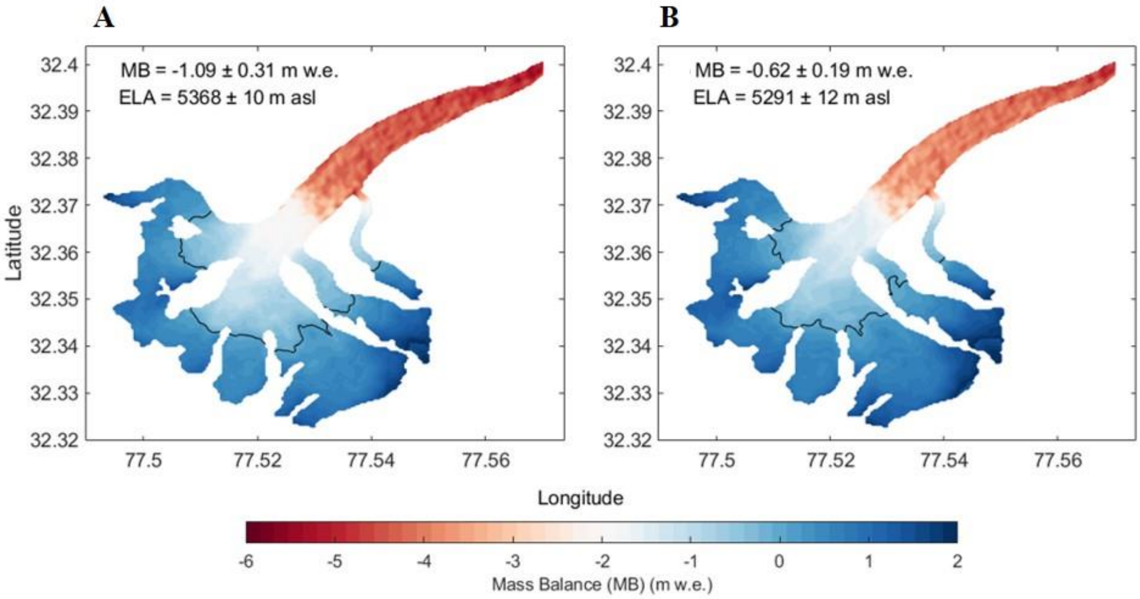

Figure 4.11. Spatial distribution of modelled annual mass balance at Sutri Dhaka Glacier for the balance years **(A)** 2015/16, **(B)** 2016/17. The black line indicates the equilibrium line altitude (ELA).

The modelled (observed) ELA is 5368 ± 10 (5398 ± 55) m a.s.l. and 5291 ± 12 (5295 ± 69) m a.s.l. during the year 2015/16 and 2016/17, respectively (Figure 4.11 and Table 4.3). The observed and model ELA of the Sutri Dhaka Glacier is higher than the observed ELA of Chhota Shigri Glacier, i.e., 5047 ± 104 m a.s.l. (Mandal et al. 2020).

Table 4.3. The modelled seasonal and annual mass balance (m w.e.) as well as the observed annual mass balance (m w.e.), modelled (observed) equilibrium line altitude (ELA; m a.s.l.) and accumulation area ratio (AAR) of Sutri Dhaka Glacier.

Year	Modelled Winter	Modelled Summer	Modelled Annual	Observed Annual	Modelled ELA	Observed ELA	Modelled (Observed) AAR
2015/16	1.99 ± 0.48	-3.07 ± 0.77	-1.09 ± 0.31	-1.16 ± 0.33	5368 ± 10	5398 ± 55	0.52 (0.48)
2016/17	2.08 ± 0.52	-2.72 ± 0.69	-0.62 ± 0.19	-0.67 ± 0.33	5291 ± 12	5295 ± 69	0.59 (0.58)

4.5.5 Contrasting climatic variables as drivers for glacier mass balance

Among the climate variables, summer T_{air} is slightly higher (3.8 ºC) for 2015/16 than 2016/17 (3.3 ºC) (Table 4.4). Precipitation amount differed considerably between 2015/16 and 2016/17 at Sutri Dhaka Glacier, with winter precipitation varying between 387 mm and 548 mm, respectively. It is similar in summer for both years (181 mm in 2015/16 and 162 mm in 2016/17) (Table 4.4). As a result, annual precipitation is substantially less (567 mm) during 2015/16 compared to 2016/17 (710 mm) (Table 4.4). Our study revealed that due to a substantially low snow accumulation the preceding winter, an early melt occurred (at a rate of ~0.009 m w.e. day^{-1}) during 2015/16 (from 5$^{\mathrm{th}}$ March, 2016), which is about 35 days in advance compared to 2016/17 (from 9$^{\mathrm{th}}$ April, 2017). This led to an enhanced melting of glacier ice in 2015/16 due to an early exposure of glacier ice. Therefore, two distinct annual mass balance results are observed for the two balance years (Table 4.3). The resulting spatially distributed annual mass balance for the period 2015/16 and 2016/17 are shown in Figure 4.11.

Table 4.4. Mean seasonal and annual meteorological variables and energy fluxes over the Sutri Dhaka Glacier, for study period from October 2015 to September 2017.

Variables	2015/16			2016/17			All Observed Period
	Winter	Summer	Annual	Winter	Summer	Annual	
T_{air} (ºC)	-9.4	3.8	-4.6	-10.7	3.3	-4.4	-4.5
T_{surf} (ºC)	-14.4	-2.1	-11.0	-17.6	-2.2	-9.6	-10.3
RH (%)	47	67	56	48	69	56	56
WS (m s^{-1})	3.8	3.4	3.6	3.6	3.3	3.5	3.6
Precipi (mm)	387	181	567	548	162	710	-
Press (hPa)	600	602	601	600	602	601	601
Cloud Cover	0.5	0.7	0.6	0.5	0.8	0.6	0.6
S_{in} (Wm^{-2})	217	294	248	192	288	233	240
S_{refl} (Wm^{-2})	116	92	112	141	106	121	116
Albedo	0.7	0.3	0.5	0.8	0.4	0.6	0.6
L_{in} (Wm^{-2})	196	260	223	202	264	227	225
L_{out} (Wm^{-2})	247	309	273	263	311	282	277
S_{net} (Wm^{-2})	101	202	136	51	181	112	124
L_{net} (Wm^{-2})	-51	-49	-50	-61	-47	-55	-52
H_{se} (Wm^{-2})	-6	22	6	-7	20	4	5
H_{la} (Wm^{-2})	-12	1	-6	-17	0	-10	-8
Q_G (Wm^{-2})	8	-8	1	6	-7	1	1
Q_{melt} (Wm^{-2})	13	181	79	9	170	77	78

In order to explore the impact of seasonality and type of precipitation in controlling the annual mass balance of Sutri Dhaka Glacier, the precipitation rates and partition are examined for the balance years 2015/16 and 2016/17. The modelled daily mean precipitation rates are 13.19 and 17.91 mm w.e. d^{-1} during 2015/16 and 2016/17, respectively. During winter, the mean daily rates of snowfall (rainfall) are 16.01 (0.00) and 23.76 (0.00) mm w.e. d^{-1} for 2015/16 and 2016/17, respectively. Compared to this, during summer, the mean daily rates of snowfall (rainfall) are 3.31 (2.73) and 4.06 (2.26) mm w.e. d^{-1} for 2015/16 and 2016/17, respectively. Therefore, the nearly 33% increase in winter snowfall, slightly enhanced summer snowfall and slightly reduced rainfall during 2016/17 led to reduced glacier melt compared to 2015/16.

4.6 Discussion

4.6.1 Sensitivity of glacier mass balance to climatic conditions

The climatic sensitivity of mass balance for the Sutri Dhaka Glacier is estimated using climatic variables and related simulations (Table 4.5). The model results suggest a decrease of mean annual mass balance of -0.25 m w.e. (29%) over an increase of 1°C in the T_{air} whereas an increase of 0.15 m w.e. (17%) in the mean annual mass balance over a decrease in T_{air} by 1°C. With a 10% increase in precipitation, the mean annual mass balance is increased by 0.21 m w.e. (24%), whereas it decreased by -0.17 m w.e. (20%) with a decrease of precipitation by 10% for the Sutri Dhaka Glacier. Therefore, the mass balance sensitivity for T_{air} and precipitation change for Sutri Dhaka Glacier is -0.21 m w.e. a^{-1} °C^{-1} and 0.19 m w.e. a^{-1} $(10\%)^{-1}$, respectively. With the increase in temperature, the melt seasons will be longer and thus warming scenario will have increased mass balance sensitivity. Furthermore, the refreezing decreases as the temperature increases, which promotes further melting and as a result, the glaciers can become more sensitive as the temperature keeps rising. However, if the temperature drops, there will be more refreezing conditions, and the glacier mass balance sensitivity will be reduced as compared to the rise in temperature. An increase in precipitation directly increases the snow accumulation, thus increasing the surface albedo, which results in higher glacier mass balance sensitivity (Mölg et al., 2009). The amount of melt energy during the summer period, seasonal precipitation, and characteristics of surface topography may thus account for the difference in the mass balance sensitivity.

A comparison with other glaciers in the region indicated that the mass balance sensitivity to T_{air} for Sutri Dhaka Glacier is significantly lower than that of the Chhota Shigri glacier (-0.52 m w.e. a^{-1} °C^{-1}) (Azam et al. 2014a) and is closer to that Stok glacier in Ladakh region (-0.32 m w.e. a^{-1} °C^{-1}) (Soheb et al. 2020). Similarly, mass balance sensitivity of precipitation is consistent with Stok Glacier (0.12 m w.e. a^{-1} $(10\%)^{-1}$) (Soheb et al. 2020). The mass balance sensitivity for relative humidity, S_{in} and wind speed change for Sutri Dhaka Glacier is -0.10 m w.e. a^{-1} $\%^{-1}$, -0.09 m w.e. a^{-1} $(Wm^{-2})^{-1}$, and -0.005 m w.e. a^{-1} $(m\ s^{-1})^{-1}$ respectively. This is similar to Urumqi River Glacier No.1 in the Tien Shan, where a change in relative humidity by ±10%, reduced the glacier mass balance by 9% and increased by 8%, whereas a change in S_{in} by ±50 Wm^{-2} decreased the glacier mass balance by 10% and increased by 8% (Che et al. 2019).

Table 4.5. Sensitivities of Sutri Dhaka Glacier mass balance to air temperature (T_{air}), precipitation (P), relative humidity (RH), incoming shortwave radiations (S_{in}), and wind speed (u).

Variables	Perturbation	Mass balance change (m w.e.)	Sensitivity
T_{air}	+1 ºC	-0.25 (29%)	-0.21 m w.e. a^{-1} °C^{-1}
T_{air}	-1 ºC	0.15 (17%)	
P	+10 %	0.21 (24%)	0.19 m w.e. $a^{-1}(10\%)^{-1}$
P	-10 %	-0.17 (20%)	
RH	+10 %	-0.10 (12%)	-0.10 m w.e. a^{-1} $\%^{-1}$
RH	-10 %	0.11 (13%)	
S_{in}	+50 Wm^{-2}	-0.09 (10%)	-0.09 m w.e. a^{-1} $(Wm^{-2})^{-1}$
S_{in}	-50 Wm^{-2}	0.1 (12%)	
u	+1 m s^{-1}	-0.02 (2%)	-0.005 m w.e. a^{-1} $(m\ s^{-1})^{-1}$
u	-1 m s^{-1}	0.009 (1%)	

The temperature variability not only controls that of the melt, but also influences the partitioning of the precipitation into snow or rain. The latter process has a potentially strong impact on the energy balance due to an associated albedo feedback. Following Cullen and Conway (2015), the role of the snow-to-rain partitioning on the mass balance of Sutri Dhaka Glacier is investigated by considering the frequency distribution of daily mean T_{air} on the days with non-zero precipitation. The distribution of T_{air} during periods of precipitation resulted in a bimodal distribution (Figure 4.12). There is a broad peak in the range -21°C to -5°C, suggesting that 60% of the precipitation events occurred on winter days with temperatures less than -5°C. In contrast, the summer peak is associated with ISM (-3°C to 5°C). Due to these differences, the snow-to-rain ratio is only weakly dependent on temperature on Sutri Dhaka Glacier with a 4% decline in snowfall for a 1°C rise in T_{air}. Consequently, the T_{air} sensitivity of mass balance on Sutri Dhaka Glacier is about ~6 times smaller than that on Halji Glacier in central Himalaya (-1.43 m w.e. a^{-1} $°C^{-1}$) (Arndt et al. 2021). Therefore, if all other factors remain the same, western Himalayan glaciers like Sutri Dhaka Glacier are likely to have a weaker mass balance response to temperature variability and change than their central and eastern Himalaya counterparts (Fujita 2008; Kumar et al. 2019). However, since our study consists of only two years of data, its representativeness for understanding future changes requires extended observations and additional analysis.

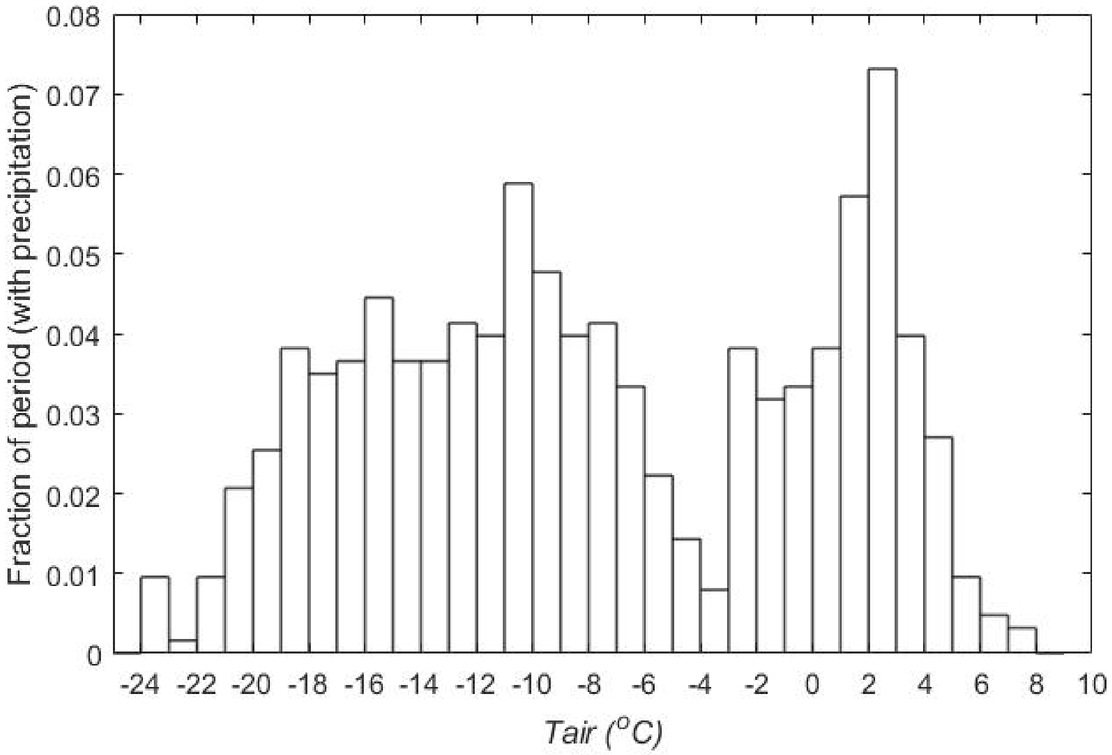

Figure 4.12. Distribution of air temperature (T_{air}) when total precipitation is > 0 on Sutri Dhaka glacier (site A4 AWS).

Chapter 5

5 Study of distributed surface energy and mass balance for upper Chandra Basin glaciers, western Himalaya

5.1 Introduction

To adequately capture the full surface energy and mass balance, a distributed physically-based model incorporating spatial variability in meteorological conditions and surface properties is required (Hock and Holmgren 2005). Ablation over glaciers processes are governed by the surface energy balance, consisting of radiative fluxes (net shortwave and longwave radiation), turbulent fluxes (sensible and latent heat), the heat flux from rain, and heat conduction into the snow/ice. The heterogeneity of glaciers and their surrounding topography creates significant spatial variability in meteorological variables and surface characteristics, leading to complex patterns in energy and mass fluxes (Yu et al. 2013; Brun et al. 2019; Patel et al. 2021). Studies that have identified significant spatial heterogeneity in mass balance across glacier surfaces, highlighting the need for physical based distributed modelling (Reijmer et al. 2012). Surface energy and mass balance are crucial for understanding the behavior of glaciers and their response to changing climatic conditions.

The western Himalaya is a particularly important region for studying glaciers, as it contains several glaciers that are experiencing significant retreat and thinning (Gardelle et al. 2013; Vijay and Braun 2016; Sharma et al. 2020; Patel et al. 2021). However, the lack of detailed, high-resolution data on the glacier surface energy and mass balance has limited our understanding of their behavior. The Chandra Basin glaciers exhibit significant variability in size, slope, aspect and surrounding topography, resulting in heterogeneity in energy fluxes over the basin (Patel et al. 2021; Oulkar et al. 2022).

Therefore, this chapter investigates and quantifies the distributed surface energy and mass balance of the upper Chandra Basin glaciers for seven hydrological years from 2015 to 2022 to understand how this balance is affected by climatic (meteorological variability) and non-climatic factors. In this study the COSIPY (COupled Snowpack and Ice surface energy and mass balance model in PYthon) model (Sauter et al. 2020) is used to simulate surface energy and mass balance of selected glaciers. Meteorological data obtained from Automatic Weather Stations (AWS) is forced as an input to the model. This data is used to extrapolate the hourly meteorological variables across the glacier surface, combined with a resampled digital elevation model, to derive the spatial distribution of surface energy and mass balance. Furthermore, the model is calibrated using in-situ point mass balance measurements and then validated over Sutri Dhaka Glacier and Samudra Tapu Glacier. Sources of uncertainty related to meteorological forcing, model parameters and surface characteristics are quantified through Monte Carlo analyses. Furthermore, both climatic and non-climatic factors influencing the mass balance of glaciers in the selected region are analyzed. The sensitivity of glacier mass balance to climatic variations is crucial, and therefore, perturbation experiments are conducted to assess the impacts of changes in air temperature and precipitation.

5.2 Study area: upper Chandra Basin glaciers

The Chandra Basin glaciers have large differences in size, surface characteristics and orientation/aspect (Figure 5.1b). A significant variability in the energy balance particularly the net shortwave radiation within the basin is caused by non-climatic and climatic parameters (Patel et al. 2021; Oulkar et al. 2022). Therefore, the basin is categorized into the upper Chandra Basin based on the orientation and size of the glaciers (Figure 5.1c). The upper Chandra Basin covers an area of ~298 km^2, about 47% of the total Chandra Basin. Chapter 5 considers only those glaciers which covers area ≥ 1 km^2, a criterion employed to mitigate uncertainties in model estimation and ensure a more precise examination of the glacier surface energy and mass balance. In addition, all these selected glaciers are clean-type glaciers and are only partially covered with debris over the lower ablation zone. Within the catchment of this selected study region, four AWS (A1, A3, A4 and A5) were installed to monitor the meteorological conditions (Figure 5.1). Using the data from these AWS sites, hourly data of meteorological variables is extrapolated along with the re-sampled (100 m resolution) digital elevation model to derive the spatial distribution of surface energy and mass balance. The study covers 18 glaciers in upper Chandra Basin which also include glaciers such as Samudra Tapu, and Sutri Dhaka. The in-situ mass balance data have been collected systematically for Sutri Dhaka Glacier and Samudra Tapu Glacier during 2015-2022 (Figure 5.2). The in-situ observations are used to validate and strengthen the effectiveness of the energy and mass balance model simulation, offering a fast and most efficient method to evaluate the model performance.

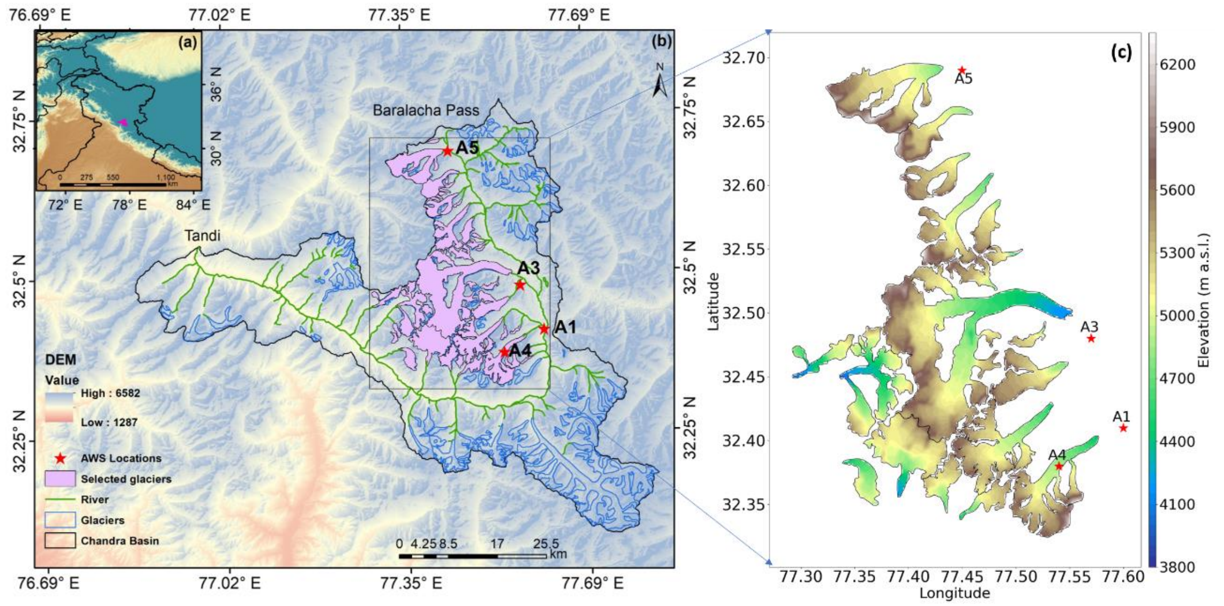

Figure 5.1. Location map **(a)** of the study region in the western Himalaya, **(b)** the Chandra Basin with selected glaciers (cyan color), and **(c)** selected glaciers. The red star represents Automatic Weather Stations (AWSs); HIMANSH Base Camp (A1, 4052 m a.s.l.), Sutri Dhaka Glacier (A4, 4864 m a.s.l.), Samudra Tapu Glacier (A3, 4513 m a.s.l.), and Baralacha Pass (A5, 4904 m a.s.l.).

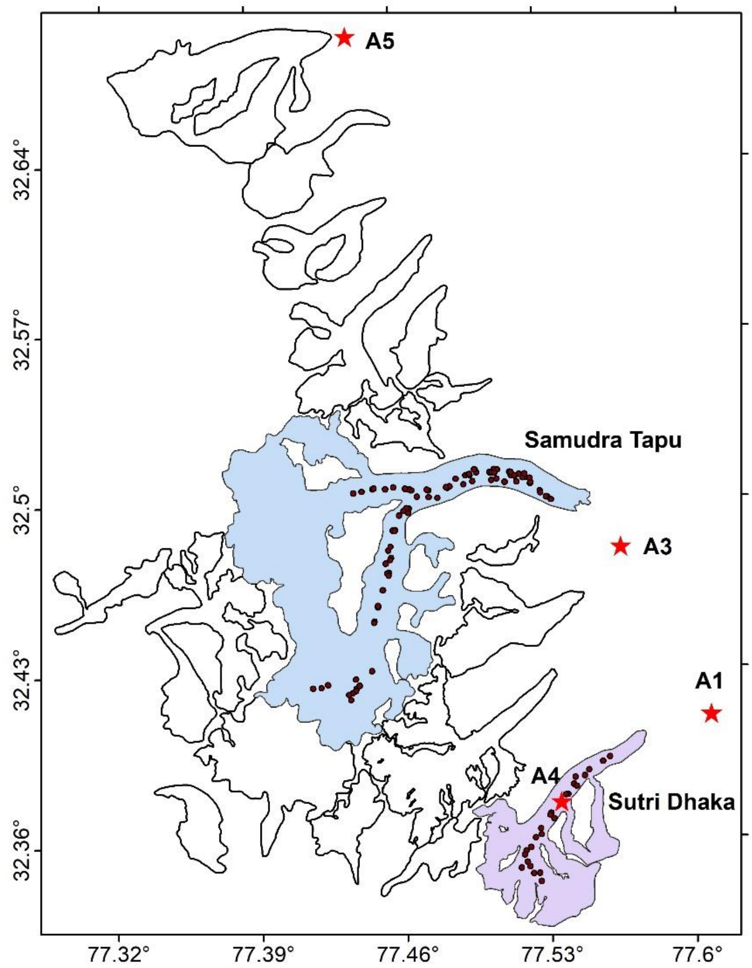

Figure 5.2. The upper Chandra Basin glacier with the location of in-situ mass balance measurements (black dots) for Sutri Dhaka Glacier and Samudra Tapu Glacier from 2015 to 2022. The red star represents Automatic Weather Stations (AWSs).

5.3 Observational data and uncertainty estimation

5.3.1 Meteorological data

To estimate the surface energy and mass balance of the glaciers in the selected upper Chandra Basin, hourly meteorological data from the A1 AWS site located at 4052 m elevation is used. The A1 site has data for the longest period from October 2015 to September 2022 with minor data gaps owing to power cuts, compared to other AWSs. To fill the data gap, hourly data is obtained from the European Centre for Medium-Range

Weather Forecasts (ECMWF) reanalysis (ERA5-land) (Hersbach et al. 2020) at the nearest surface grid points of A1 sites using bias correction. In addition, data for air pressure and total precipitation is obtained from the ERA5 for the nearest surface level at the two-point location of A1 site. Cloud cover over the study area is estimated using the method from Van den Broeke et al. (2006). This method calculates cloud cover as a fraction between 0 and 1 based on net longwave radiation and air temperature measurements.

To simulate the surface energy and mass balance of the selected glaciers, a 100 m resolution digital elevation model (DEM) derived from the 30 m ASTER GDEM V2 dataset is used. The ASTER GDEM V2 data is obtained from the Earth Remote Sensing Data Analysis Centre (ERSDAC) (Tachikawa 2011). The lapse rate or vertical gradient is highly sensitive to surface characteristics and local microclimate and thus significant variations are expected in the extrapolated data. To ensure accurate distributed data, the selected upper Chandra Basin glaciers is partitioned into four zones: CB1, CB2, CB3, and CB4 (Figure 5.3). This is based on the proximity of these zones to four installed AWS (A1, A3, A4, and A5) and their aspects (Figure 5.3). Meteorological data obtained from these AWS is utilized to estimate lapse rates for the corresponding zones, thereby representing the vertical gradients of air temperature and relative humidity (Table 5.1). Lapse rates are computed on a mean annual basis by regression of the AWS data against station elevation. The lapse rates are then applied to extrapolate the point AWS data to the entire DEM based on the elevation at each 100 m grid cell to obtain distributed surface energy and mass balance of the glaciers (Table 5.1). The precipitation and air pressure gradient data used in this analysis are obtained from previous study by Oulkar et al. (2022). These distributed meteorological data are forced as inputs to the energy balance model to simulate hourly mass balance for the seven hydrological years.

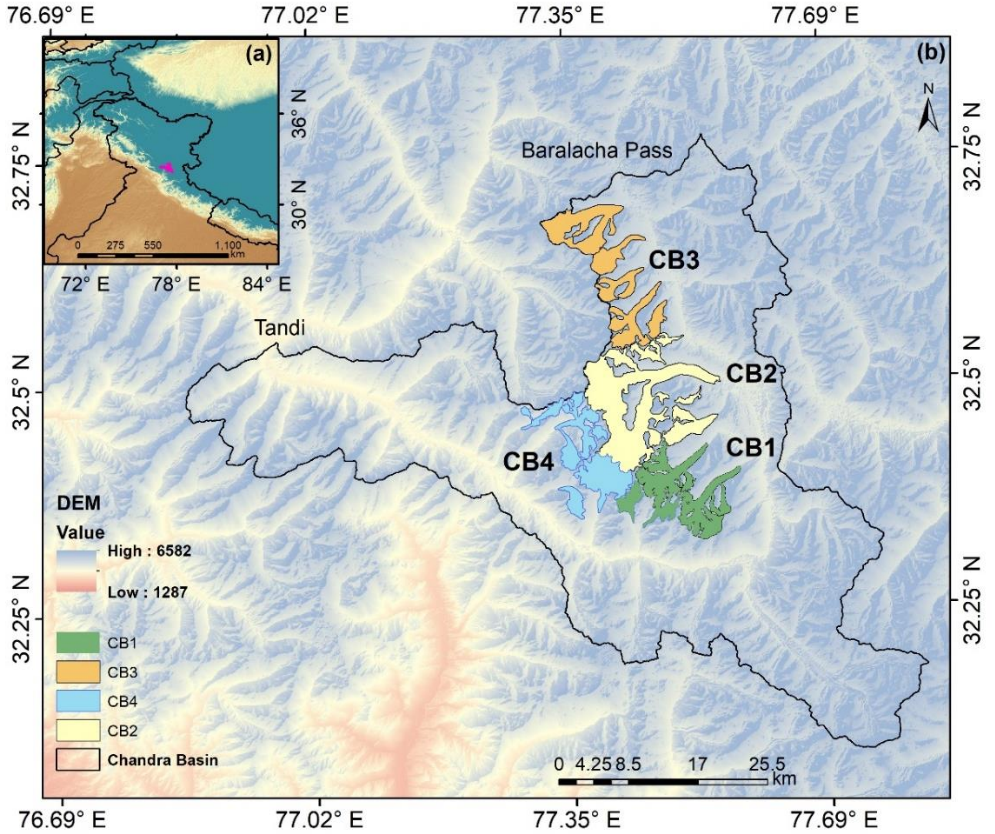

Figure 5.3. Location map **(a)** of the study region in the western Himalaya, **(b)** Upper Chandra Basin glaciers partitioned into four zones (CB1, CB2, CB3, and CB4) based on their proximity to four installed AWS (A1, A3, A4, and A5).

Table 5.1. Details of model parameters (altitudinal gradient/lapse rates) and extrapolation methods.

Variables	Parameters/Model			
	CB1	CB2	CB3	CB4
Air temperature lapse rate (°C m^{-1})	-0.0035	-0.0031	-0.0044	-0.0037
Relative humidity lapse rate (% m^{-1})	0.049	0.032	0.022	0.031
Precipitation gradient (% m^{-1})	0.12 (Oulkar et al. 2022)			
Air pressure gradient (hPa m^{-1})	-0.034 (Oulkar et al., 2022)			
Cloud cover	Estimated based on $Lnet$ and $Tair$ (Van den Broeke et al. 2006)			
Incoming shortwave radiation	Solar radiation model (Georg et al. 2016)			
Longwave radiation	Stefan–Boltzmann law (Klok and Oerlemans 2002)			
DEM: digital elevation model (m)	100 x 100 m resolution			

5.3.2 Model uncertainty assessment

The model uncertainty is quantified by running the repeated Monte Carlo simulations at all observed point locations on Samudra Tapu Glacier and Sutri Dhaka Glacier (Figure 5.2). The mean mass balance of 500 Monte Carlo simulations is within the uncertainty range of the corresponding in-situ values. Based on the results of the 500 simulations compared against the observed mass balance, there is a good match between the uncertainty range and observed mass balance (Figure 5.4). This uncertainty range is determined by calculating the standard deviation of the mass balance results. The standard deviation captures the spread in mass balance estimates from the 500 simulations. With a normal distribution of results, about 68% of simulations are within ±1σ. Therefore, the ±25% uncertainty range represents approximately ±1σ of the mass balance results from the simulations.

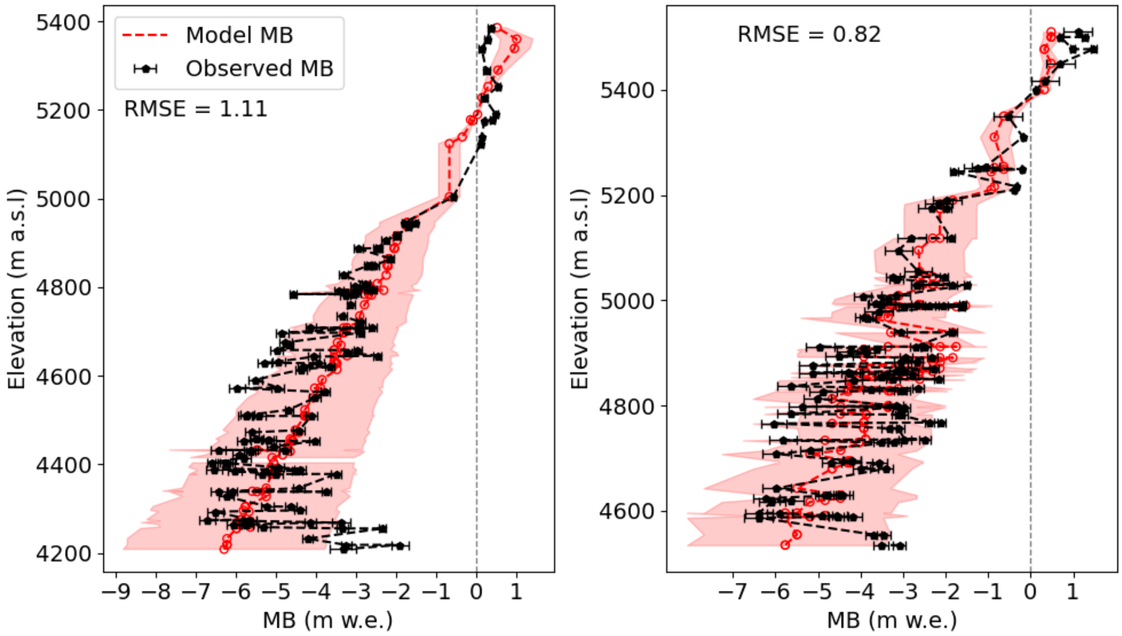

Figure 5.4. The observed and modelled mass balance (m w.e.) with the uncertainty of **(a)** Samudra Tapu Glacier and **(b)** Sutri Dhaka Glacier. The pink area represents the 500 model runs in Monte Carlo simulations.

5.4 Results and discussion

5.4.1 Climatic setting

Figure 5.5 shows the daily mean meteorological variables over the upper Chandra Basin glaciers for the study period from October 2015 to September 2022. These meteorological variables show substantial temporal variation and distinct patterns over the study period. The daily mean air temperature ranges from -25.48 to 15.67 °C with a mean annual value of 1.67 °C (Figure 5.5a). The daily mean relative humidity ranges from 16 to 99%, with a mean annual value of 60% (Figure 5.5b). The daily mean wind speed ranges from 0 to 9.84 m s^{-1} with a mean annual value of 4.57 m s^{-1} (Figure 5.5c). The daily mean incoming shortwave radiation ranges from 37 to 400 Wm^{-2}, with a mean annual value of 237 Wm^{-2} (Figure 5.5d). The incoming longwave radiation ranges from 139 to 344 Wm^{-2}, with a mean annual value of 343 Wm^{-2} (Figure 5.5e). The daily mean pressure ranges from 597 to 636 hPa (Figure 5.5f). The highest cloud cover is observed in the winter with mean of 0.7 and the lowest in the summer with a mean of 0.3 (Figure 5.5g). This significant variability in meteorological variables can be attributed to the semi-arid climate conditions prevailing in the area (Bookhagen and Burbank 2010). During the summer, warm and humid air is brought into the region, causing temperatures to rise (Oulkar et al. 2022). Consequently, the higher humidity levels also contribute to the warmer climate during this period. In contrast, during the winter, the monsoon winds subside, and the western disturbance becomes active, leading to a drop in temperatures and an increase in cloud cover (Figure 5.5a, g). The combined influence of these factors results in the observed variations in climate over the Chandra Basin. The contrasting temperatures and moisture throughout the year can affect the ablation and accumulation rates of the glaciers, leading to changes in their overall mass balance.

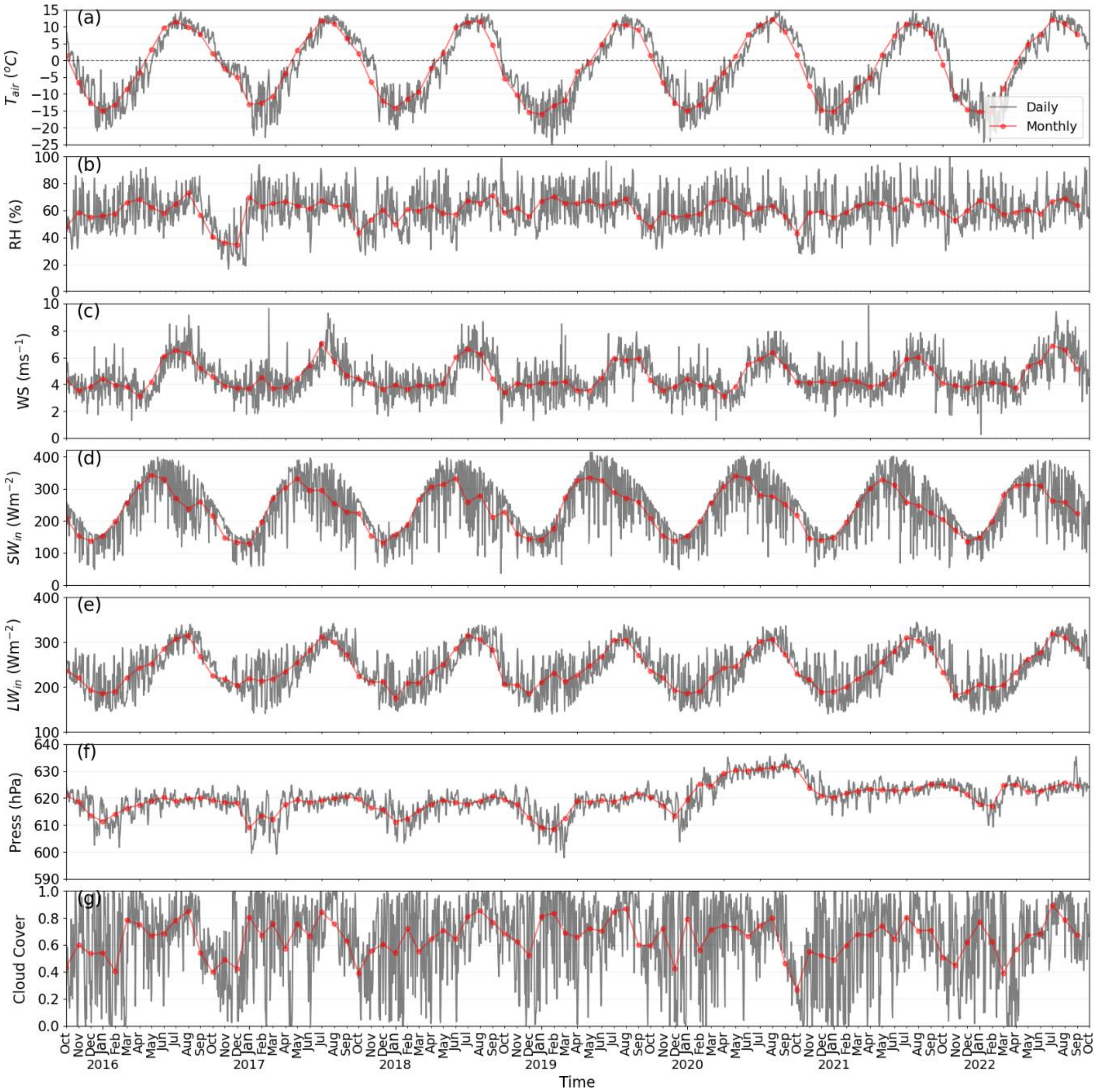

Figure 5.5. Observed daily mean values of **(a)** air temperature (Tair, °C), **(b)** relative humidity (RH, %), **(c)** wind speed (m s^{-1}), **(d)** incoming shortwave radiation (SWin, Wm^{-2}), **(e)** incoming longwave radiation (LWin, Wm^{-2}), **(f)** pressure (hPa), and **(g)** cloud cover over the Chandra Basin glaciers at the site A1 for study period from October 2015 to September 2022.

5.4.2 Distributed surface energy fluxes

The distributed energy fluxes estimated using distributed meteorological data over seven hydrological years (2015 to 2022), including mean net shortwave (SW_{net}) and longwave (LW_{net}) radiation, mean turbulent heat fluxes (H_{se} and H_{la}), and mean ground heat flux (Q_g) are shown in Figure 5.6. The mean SW_{net} ranges from 30 to 130 Wm^{-2} (Figure 5.6a) and varies with altitude. Specifically, the SW_{net} values decrease with increasing altitude, primarily due to the higher albedo over the accumulation zone. The SW_{net} is the largest energy source, with higher values in the ablation zone compared to the accumulation zone. This reflects the lower albedo and greater absorbed solar radiation at lower elevations. SW_{net} shows strong seasonal variation, with peak value during the summer season when incoming solar radiation is at a maximum. The mean LW_{net} varied from -106 to -84 Wm^{-2} and decreased with the altitude (Figure 5.6b). This variation can be attributed to the influence of temperature and relative humidity as a function of altitude. The LW_{net} is negative across the region, indicating radiative cooling. More negative values are found at higher altitudes, likely due to colder temperatures. The turbulent heat flux H_{se} (0 to 38 Wm^{-2}) and H_{la} (-78 to -21 Wm^{-2}) shows strong spatial variation (Figure 5.6c,d). The turbulent heat fluxes of H_{se} and H_{la}, shows maximum values at lower elevations due to the presence of large gradients in surface temperature and water vapor pressure. As altitude increases, the turbulent heat fluxes tend to decrease (Figure 5.6c,d). The magnitude of $\mathrm{Q_g}$ heat flux is small compared to the other energy components and varied from -44 to -7 Wm^{-2} (Figure 5.6e).

The surface energy flux components show a strong seasonality, with net shortwave and longwave radiation being the dominant energy flux in the ablation season. In contrast, sensible and latent heat flux dominates in the accumulation season. The annual contribution of energy flux revealed that net shortwave radiation made up the largest portion at 58% of the total, followed by net longwave radiation at 25%, sensible heat at 8%, latent heat at 6%, and ground heat flux at 3%. These findings are consistent with prior energy balance studies on Himalayan glaciers in this region (Azam et al. 2014b; Patel et al. 2021; Oulkar et al. 2022). Also, the altitude dependence and seasonal variations match previous observations on high mountain glaciers (Nair et al. 2023).

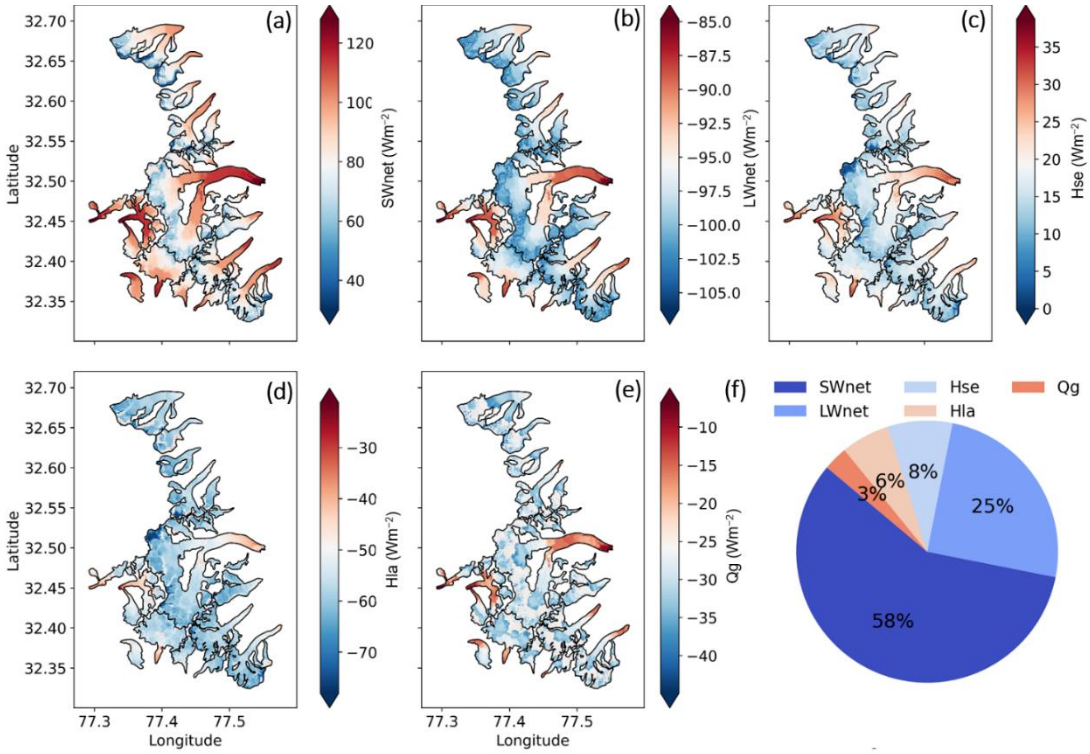

Figure 5.6. Distributed mean surface energy fluxes for the glaciers of the upper Chandra Basin for the period from October 2015 to September 2022. **(a)** SW_{net} is net shortwave radiation, **(b)** LW_{net} is net longwave radiation, **(c)** H_{se} is sensible heat flux, **(d)** H_{la} is latent heat flux, **(e)** Q_g is ground heat flux and **(f)** annual contribution of each energy flux in percentage.

5.4.3 Mass balance

5.4.3.1 Mean mass balance

Figure 5.7 shows the changes in the mass balance of the upper Chandra Basin over seven hydrological years from 2015 to 2022. The annual mass balance ranges from -0.89 to 0.1 m w.e., indicating an overall trend of negative mass balance. The estimated mean mass balance for upper Chandra Basin glaciers is -0.51 ± 0.28 m w.e. a^{-1}, with a cumulative mass balance of -3.54 m w.e during the last seven years. Overall, the modelled mean mass balance for seven hydrological years is consistent with the mass balance reported by various studies within the Chandra Basin (Table 5.2). However, a positive mass balance is observed for the hydrological year 2018/19, attributed to higher accumulation driven by an extreme snowfall event in 2018 that covered most of the Lahaul-Spiti district (Pratap et al. 2023). This shows that extreme events can also affect the mass balance of the glaciers and that some years may have more favorable conditions for the growth of glaciers than others. However, this does not change the overall trend of glacier retreat, driven by long-term climate change. The modelled result agrees with the general trend of decreasing mass balance over time, indicating that the upper Chandra Basin is experiencing a negative glacier mass balance.

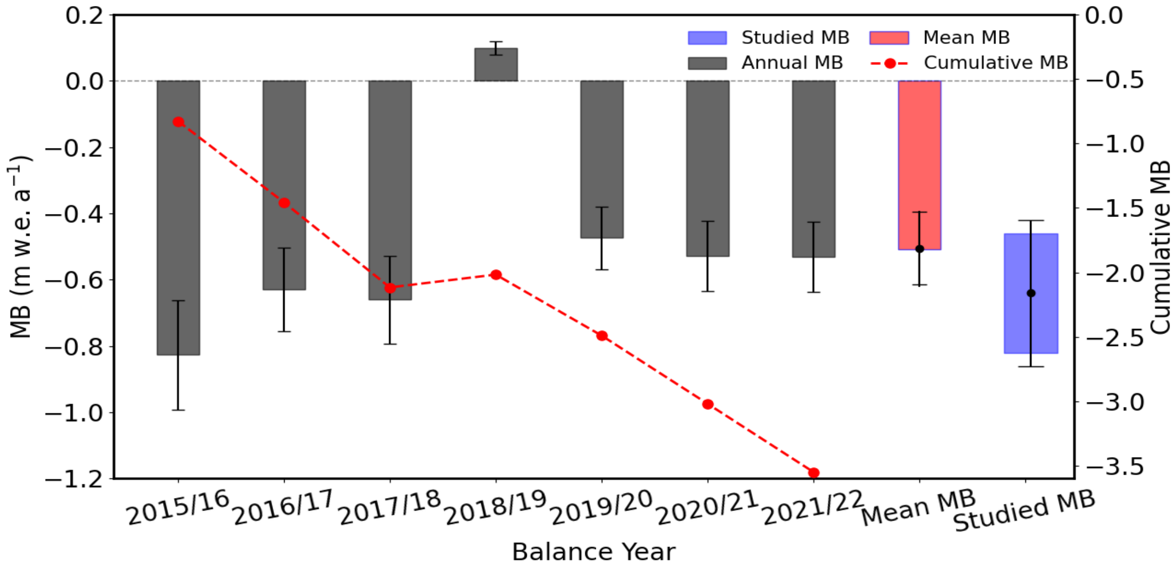

Figure 5.7. Mean annual mass balance of upper Chandra Basin for seven hydrological years from October 2015 to September 2022. The red bar is modelled mean mass balance, the purple box is previously studied mass balance in this region, and the red line shows the cumulative mass balance trend.

Table 5.2. Various methods mean mass balance for Chandra Basin glaciers.

Mass Balance Method	Mean Mass Balance (m w.e. a^{-1})	Year	Reference
Geodetic*	−0.47 ± 0.50	1989-2020	Chandrasekharan and Ramsankaran (2023)
VIC Model*	−0.18 ± 0.14	1980-2018	Laha et al. (2023)
Energy balance+	−0.82 ± 0.21	2015-2017	Oulkar et al. (2022)
Energy balance+	–0.59 ± 0.12	2013-2018	Patel et al. (2021)
Glaciological@	−0.57 ± 0.12	2013-2017	Sharma et al. (2020)
Glaciological$	−0.46 ± 0.40	2002-2019	Mandal et al. (2020)
Geodetic*	−0.31± 0.08	2000-2016	Shean et al. (2020)
Geodetic*	−0.13 ± 0.14	1975-2000	Maurer et al. (2019)
Geodetic*	−0.48 ± 0.15	2001-2016	Maurer et al. (2019)
Geodetic*	−0.30 ± 0.10	2000-2015	Mukherjee et al. (2018)
Geodetic*	−0.37 ± 0.09	2000-2016	Brun et al. (2017)
Geodetic*	−0.61 ± 0.46	1984-2012	Tawde et al. (2017)
Geodetic*	−0.37 ± 0.09	2000-2016	Brun et al. (2017)
Glaciological$	−0.56 ± 0.40	2002-2014	MFR Azam, A. et al. (2016)
Geodetic*	−0.52 ± 0.32	2000-2012	Vijay and Braun (2016)
Geodetic^	−1.44 ± 0.69	2001-2012	Mishra et al. (2014)
Geodetic*	−0.68 ± 0.15	1999-2011	Gardelle et al. (2013)
Geodetic*	−0.44 ± 0.09	1999-2011	Vincent et al. (2013)

*Region: *Chandra Basin, +Sutri Dhaka, #Eight glaciers, @Five glaciers, $Chhota Shigri, ^Hampta*

5.4.3.2 Distributed mass balance

Figure 5.8 highlights the variability of glaciers' SMB across the upper Chandra Basin and revels that the glaciers experiencing mass loss in the ablation zone. The study reveals spatial variability in mass balance, with lower values in the high-elevation areas of the glaciers and higher values in the lower elevation. This spatial variability can be attributed to several factors, including differences in glacier geometry, aspect, and shading effects (Yu et al. 2013; Brun et al. 2019; Olson and Rupper 2019; R. Kumar et al. 2021; Wang et al. 2022). Along with meteorological parameters other variables like precipitation distribution, snowdrift effect, albedo differences, and streamflow can also contribute to the spatial mass balance variability (Yang et al. 2013; Brun et al. 2015).

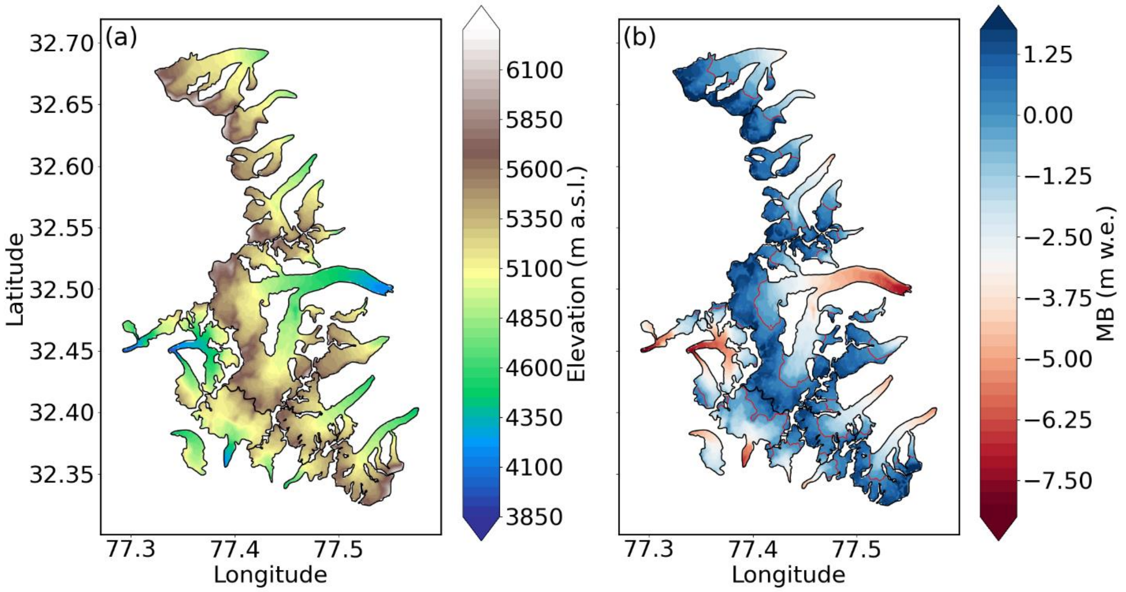

Figure 5.8. (a) Digital elevation model based on ASTER GDEM V2 and **(b)** distributed mean surface mass balance for the glaciers of the upper Chandra Basin for the period from October 2015 to September 2022. The red line indicates the equilibrium line altitude (ELA).

5.4.4 Non-climatic parameters and mass balance spatial variability

The upper Chandra Basin has varying topography, including differences in elevation, size, aspect, orientation and slope, as detailed in Table 5.3. Higher elevations (>5500 m a.s.l.) have lower temperatures, humidity, air pressure and different precipitation patterns. This leads to more positive or balanced mass balance at and above median elevations but increasing negative mass balance at lower elevations (Figure 5.8a and Table 5.3). For example, glaciers in the study area lost 31% of its mass balance within the 4700-5400 m a.s.l. elevation range and remaining mass balance loss over lower elevation. Furthermore, higher elevations receive more solid precipitation due to colder temperatures, resulting in more accumulation (Bhattacharya et al. 2023). However, meteorological conditions (season) can vary at different elevations at particular times, such as the onset or end of summer when snowfall may occur in upper accumulation zones while melt continues in lower ablation zones (Cuffey and Paterson 2010). The size and shape of a glacier influence its mass balance by affecting accumulation and ablation patterns. For example, the larger Samudra Tapu Glacier had a more negative mass balance compared to a smaller glacier (Figure 5.8). Glaciers with more extensive area coverage at higher elevations are likely to accumulate more mass from solid precipitation, while glaciers with greater area at lower elevations may experience higher ablation rates due to warmer temperatures (Racoviteanu et al. 2015).

Table 5.3. Topographic parameter characteristics for the selected glaciers of the upper Chandra Basin.

S. No	Lon	Lat	Zmax (m a.s.l.)	Zmin (m a.s.l.)	Zmean (m a.s.l.)	Zmed (m a.s.l.)	Area (km^2)	Slope (degree)	Aspect (degree)	Direction
1	77.378	32.671	6286	4707	5360	5299	31.02	14	126	NE
2	77.414	32.638	6162	4744	5408	5373	11.37	20	139	NE
3	77.423	32.605	5889	4782	5381	5410	10.3	14	122	NE
4	77.437	32.564	6349	4541	5293	5335	17.45	15	126	NE
5	77.472	32.566	5849	4772	5283	5279	5.65	15	133	N
6	77.484	32.545	5712	4615	5238	5264	2.28	20	83	E
7	77.460	32.532	5999	4680	5393	5420	5.49	19	128	SE
8	77.436	32.474	5900	4200	5186	5268	78.9	12	145	NE-SE
9	77.512	32.479	5761	4565	5206	5228	2.22	18	89	NE
10	77.507	32.449	5917	4743	5354	5398	14.04	14	121	E
11	77.479	32.395	5861	4465	5236	5264	26.93	13	139	NE
12	77.531	32.357	6000	4500	5302	5366	19.6	15	172	NE
13	77.321	32.466	5361	4022	4738	4776	5.74	16	214	SW
14	77.369	32.445	5500	3840	4832	4896	23.15	17	200	W
15	77.399	32.394	5721	4173	5106	5142	24.78	14	208	S
16	77.433	32.369	5696	4499	5155	5189	6.96	14	171	S
17	77.477	32.355	5625	4439	5187	5246	5.38	13	248	SW
18	77.360	32.369	5207	4421	4832	4854	6.22	14	179	NE

Further, the study indicates that southeast, south, southwest and west-facing aspects significantly contribute to the highest melting zones in the study area (Figure 5.9a). This is likely due to the effects of topographic shading on spatial variability in mass balance. Glaciers on northeast-facing slopes receive less direct solar radiation, and experience reduced ablation compared to southwest-facing glaciers (Figure 5.6b and 7a), which is consistent with findings by Olson and Rupper (2019). Mountain shadows can partially cover glaciers, limiting sunlight exposure and reducing melting, in agreement with previous studies (Klok and Oerlemans 2002; Wang et al. 2022). Spatial differences in incident radiation are predominantly attributable to shading, although cloud cover is crucial in reducing absolute radiation levels. Topographic shading directly alters the radiation budget at the glacier surface by obstructing incoming solar radiation. Our results indicate topographic shading is an important control of surface energy and mass balance estimates.

The slope of selected glaciers in the upper Chandra Basin ranges from 1° to 57° with a mean of 15° (Figure 5.9b and Table 5.3). However, most glaciers in the selected region have gentle slopes between 12° and 20° (Figure 5.9b and Table 5.3). This zone experiences the highest melting rates, agreeing with other findings (Fischer et al. 2015; Rabatel et al. 2016; R. Kumar et al. 2021). In the lower ablation zone of a glacier, the slope is gentle, resulting in a low temperature gradient (Zhang et al. 2022). Consequently, this area experiences higher rates of melting. In contrast, the accumulation zone of the glacier has a steeper slope, leading to a higher temperature gradient and lower rates of melting (Zhang et al. 2022). The steep slopes in upper accumulation zones are less susceptible to regional mass loss (Fischer et al. 2015; Rabatel et al. 2016; Davaze et al. 2020; R. Kumar et al. 2021). More gentle slopes correlate with more negative mass balance over lower ablation zones, as also reported by Davaze et al. (2020).

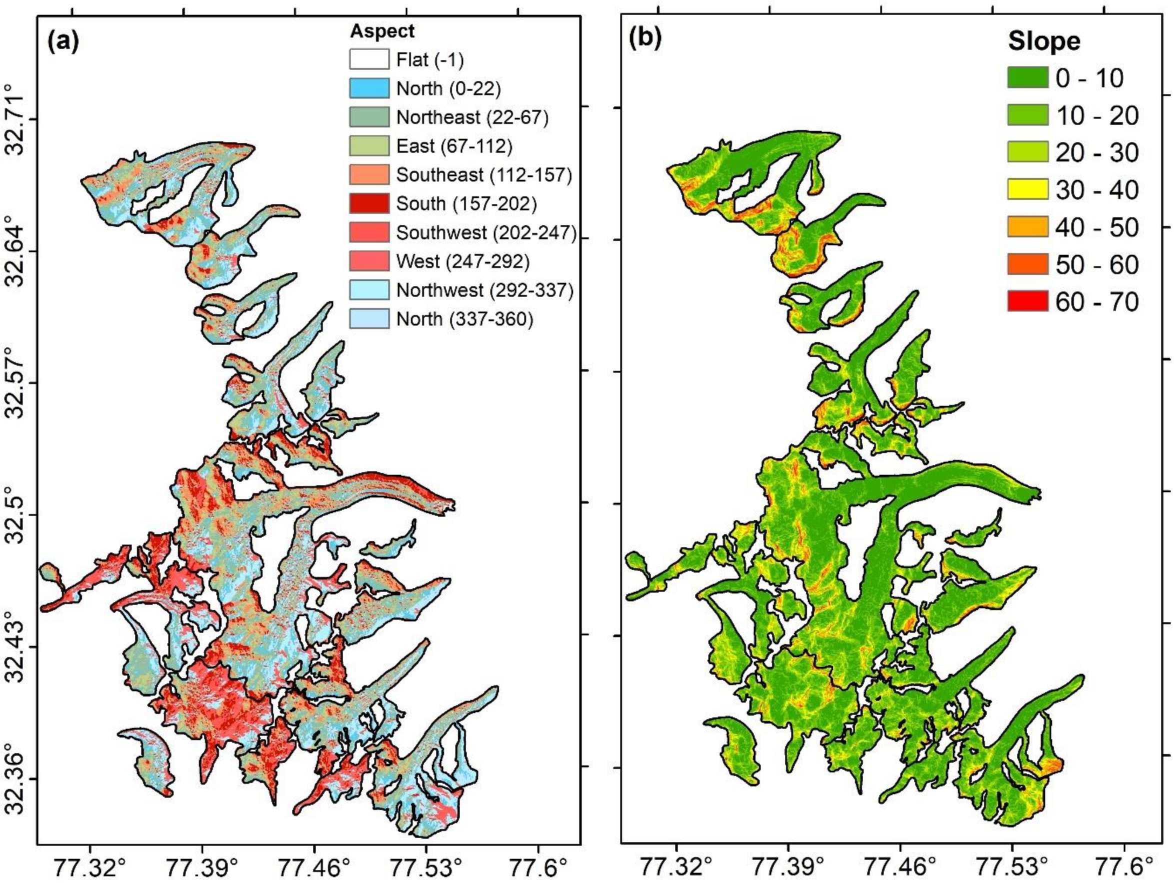

Figure 5.9. The upper Chandra Basin map showing **(a)** aspect and **(b)** slope.

The aspect, slope, size and elevation of the glacier contribute towards the spatial variability of mass balance within the selected region, consistent with previous studies that have examined the complex relationship between topography and glacier melt dynamics across the. However, the spatial resolution of DEM noticeably alters the accuracy of topographic factors on distributed surface energy and mass balance of glaciers. Further studies are needed to clarify the interactions between shading, radiation, and melt patterns in this region.

5.4.5 Mass balance sensitivity to climatic conditions

Variations in air temperature and precipitation play pivotal roles in driving glacier mass balance changes, as explored through simulations conducted to investigate their impact on the mass balance of the Sutri Dhaka Glacier (Oulkar et al. 2022). In order to evaluate the climate sensitivity of the upper Chandra Basin glacier mass balance, perturbation experiments of air temperature and precipitation were performed. During these simulations, other pertinent variables remained constant. Additionally, a coupled parameter perturbation approach employed, wherein alterations in both air temperature and precipitation are simultaneously introduced as forcings to the model. This approach mainly sought to address the extent to which changes in precipitation could compensate for the additional loss of glacier mass attributed to a 1 °C increase in air temperature.

To simulate temperature variations, the air temperature changed by a step of 0.5 °C from -2 °C to +2 °C, while keeping other input parameters constant (Figure 5.10). The results show that the temperature increase of 1 °C led to a 64% reduction in the total mass balance (an increase in mass loss). In contrast, a temperature reduction by 1 °C resulted in a 51% increase in the mass balance (a decrease in mass loss) (Figure 5.10). Moreover, when the temperature is increased by 2 °C, the total mass balance decreases by 136%. In contrast, a temperature decreases of 2 °C led to a 90% increase in the total mass balance. Similarly, simulations are conducted to explore the effects of precipitation changes using eight scenarios, where the precipitation is adjusted in 10% increments from -40% to +40%. Increasing the precipitation by 20% resulted in a 32% increase in the total mass balance, while a 20% decrease led to a 25% reduction in the total mass balance. Notably, at a 40% increase in precipitation, the total mass balance exhibited a slightly less negative equivalent to a 60% increase in glacier mass balance.

Further, the temperature and precipitation have different slopes, indicating that temperature and precipitation have different effects on glacier mass balance (Figure 5.10). Notably, augmenting precipitation yields a slightly positive effect compared to reducing precipitation (Figure 5.10). Across the upper Chandra basin, the mass balance sensitivity for air temperature and precipitation change is -0.29 m w.e. a^{-1} $°C^{-1}$ and 0.14

m w.e. a^{-1} $(10\%)^{-1}$, respectively. However, the impact of temperature changes on glacier mass balance is more pronounced than that of precipitation changes, as the temperature shows a steeper slope in comparison to the precipitation (Figure 5.10). This is consistent with the findings of previous studies that have shown that temperature is the dominant factor controlling glacier mass balance globally (MF Azam et al. 2018; S Singh et al. 2018; Fugger et al. 2022). However, precipitation can still influence glacier mass balance by affecting the amount and type of precipitation, snowpack density, albedo, and runoff.

Furthermore, it is observed that higher air temperatures accelerated the rate of glacier mass loss, while the compensatory effect of increased precipitation for change in glacier mass balance is not commensurate (Figure 5.10). The present study reveals that a 42% increase in precipitation is necessary to counteract the additional mass loss resulting from a 1 °C increase in air temperature for the upper Chandra Basin glaciers.

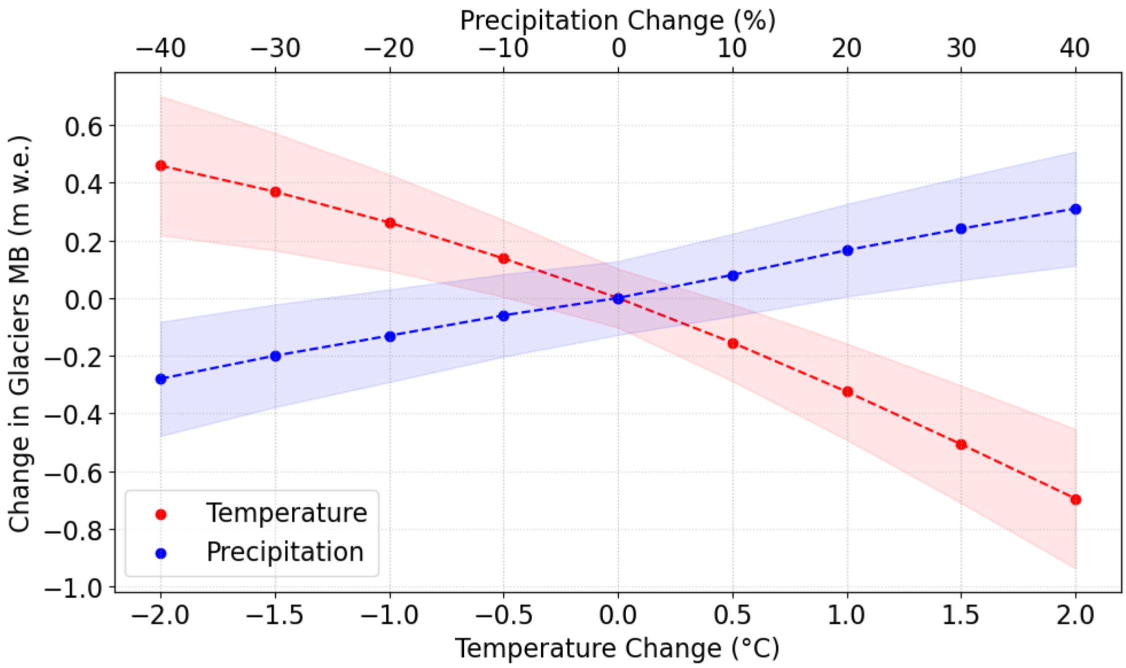

Figure 5.10. Sensitivity of mass balance in the upper Chandra Basin glaciers to air temperature and precipitation changes. The shaded area represents the uncertainty in the mass balance simulation.

Chapter 6

6 Summary and conclusions

Over the last two decades, elevation-dependent warming has become more prominent in the Himalayan region, contributing to increased warming trends and affecting regional climate and freshwater availability by impacting glacier ice and seasonal snow (Bolch et al. 2012; Immerzeel et al. 2020; Pepin et al. 2022; Nair et al. 2023). However, there are significant knowledge gaps regarding glacier-atmosphere interactions, energy balance, and mass balance processes in the data-scarce Himalaya (Mayewski et al. 2020). Therefore, this thesis is aimed to advance understanding of spatio-temporal variability in temperature lapse rate (TLR), surface energy balance and mass balance of glaciers in the Chandra Basin, western Himalaya, using an integrated approach combining in-situ observations and physically-based modeling work.

The overarching goal of this study is to improve the physical understanding of temperature variability, energy balance and mass balance in complex high mountain topography and its implications for glacio-hydrological modeling across the Himalaya. The key findings of this doctoral thesis are summarized in the following sections.

6.1 Temporal variability in air temperature lapse rate of the Chandra Basin

This study presents an analysis of the temporal variations of TLR over the Chandra Basin, in the western Himalaya. Here, in situ data from a network of AWS spread across elevation ranging from 4052 to 4904 m a.s.l is used. The observed air temperature data from AWSs are used to estimate the TLR. Over the Chandra Basin, the estimated mean annual TLR is 3.8 ± 0.3 °C km^{-1} with a strong seasonal variability. It is found that the TLR values are higher in the summer and lower in the winter. During summer, the maximum TLR is attributed to warm and humid conditions, while in winter, the minimum is due to inversions caused by radiative cooling. Inversion effect leads to negative TLR values during winter at lower elevations, indicating atmospheric instability. Strong diurnal variations are also observed in the TLR, with maximum values from 10:00 to 18:00 hrs and minimum values from 20:00 to 09:00 hrs. The temporal variability of observed TLR is site-specific and strongly correlated with wind speed, relative humidity, and radiation fluxes. Sensitivity analysis found that the modeled mean mass balance is highly sensitive to changes in TLR within the observed range of 3.0 to 7.5 °C km^{-1}. The modeled mean annual mass balance sensitivity is 0.3 m w.e. a^{-1} per °C km^{-1}. The study revealed that employing observed lapse rate is critical for accurately extrapolating air temperatures and reducing biases in mass balance modeling over glacierised regions. A strong spatio-temporal variability of the TLR in the basin highlights the need for locally determined TLR values instead of relying on standard environmental lapse rate for glacio-hydrological applications. Furthermore, the non-linear temperature gradient due to inversions needs to be considered in models while extrapolating the temperature distribution at a regional scale.

6.2 Energy fluxes, mass balance and climate sensitivity of Sutri Dhaka Glacier

This study derived the distributed surface energy and mass balance of Sutri Dhaka Glacier using a physically-based model (COSIMA) in response to atmospheric forcing, and compared the results with glaciological mass balance observations during two contrasting meteorological years (2015 to 2017). Firstly, surface energy and mass balance are simulated at the observed point location and then calibrated with the in-situ glaciological mass balance data. The model surface albedo, incoming longwave radiation, and surface temperature corresponded well with the in-situ data. Comparison of model output with the in-situ observation suggests that the model performed very well and is therefore reliable for simulating distributed surface energy and mass balance. Seasonal variations in energy fluxes were dominated by changes in S_{net} and L_{net} fluxes, which significantly governed the mass balance of Sutri Dhaka Glacier. The model-derived mean annual mass balances of -1.09 ± 0.31 and -0.62 ± 0.19 m w.e. for 2015/16 and 2016/17 are similar to the measured values of -1.16 ± 0.33 and -0.67 ± 0.33 m w.e., respectively. The sensitivity analysis shows that the mass balance is affected by air temperature (-0.21 m w.e. a^{-1} $°C^{-1}$) and precipitation (0.19 m w.e. a^{-1} $(10\%)^{-1}$) changes. The study suggests that the partitioning of precipitation into snow and rain is less sensitive to temperature changes for glacier mass balance because most precipitation falls as snow during the cold winters in the western Himalaya. The study provides an opportunity for improved prediction of the surface mass balance of western Himalayan glaciers in a future climate change scenario.

6.3 Distributed surface energy and mass balance for upper Chandra Basin glaciers in western Himalaya

This study investigated the distributed surface energy and mass balance of several glaciers in the upper Chandra Basin. It used a physically-based model (COSIPY) to estimate energy fluxes and mass balance for seven hydrological years from 2015 to 2022. Meteorological data from Himansh station AWS (A1 site) and ERA5-land data is employed as input for the model, and the parameters are calibrated using in-situ observations. The study addressed uncertainties inherent in the modeling process through a Monte Carlo simulation approach. The study highlighted the strong seasonality of energy fluxes, with net radiation being the dominant energy flux during summer months, while sensible and latent heat fluxes dominated in the winter. The results also revealed the spatial variability in energy fluxes and mass balance across the glaciers within the upper Chandra Basin, highlighting the influence of other factors like glacier geometry, shading effects, local topography, and orientations/aspect on mass balance. The estimated mass balance of the glaciers indicated an overall negative mean annual mass balance of –0.51 ± 0.28 m w.e. a^{-1} with a cumulative mass balance of -3.54 m w.e over the seven-year period. The study demonstrated that the glacier mass balance is highly sensitive to changes in air temperature and precipitation, with even small temperature variations causing significant shifts in the mass balance. The study reveals that a 42% increase in precipitation is necessary to counteract the additional mass loss resulting from a 1 °C increase in air temperature for the glaciers. The comparison of model results with other mass balance studies indicated consistency and validated the accuracy of the model. This study provides valuable insights on the energy and mass balance of glaciers in the Chandra Basin and can be used to better understand the impacts of climate variability on regional glacier mass balance.

6.4 Future perspectives

6.4.1 Research contributions

The temperature lapse rate (TLR) study findings contribute to an improved understanding of the spatio-temporal variability of lapse rates in high-altitude glacierised regions of the western Himalaya. It highlights the importance of considering topographic factors and local meteorological conditions when estimating lapse rates in complex mountainous terrains. This study will improve the accuracy of temperature distribution and downscaling techniques used in climate models and glacio-hydrological studies in the Himalayan region. While this study allowed for the characterization of seasonal and diurnal patterns in TLR variability across the basin, it needs to be further examined for a longer period. Further, the AWS network in this study covered only a limited elevation range (4052 to 4904 m a.s.l.) within the basin, and therefore may not represent all elevation zones, within the Himalayas. Extending the network to across different elevations may provide a more improved understanding of TLR variability across the Himalayan region. The study also highlighted substantially high values of TLR at certain AWS sites, indicating potential microclimate and local influences on the observations that needs consideration. Therefore, when computing TLR, it is crucial to consider the specific site characteristics and local factors that may influence temperature variability as TLR varies within the mountainous regions attributed to complex topography, diverse surface characteristics, microclimatic effects, and turbulent heat exchanges (Minder et al. 2010; Shen et al. 2016; Qin et al. 2018; Sun et al. 2022). Furthermore, the non-linear temperature gradient due to inversions needs to be considered in models while extrapolating the temperature distribution at a regional scale. Future studies may also include varied glacierised basins across the Himalayan region to investigate the spatio-temporal variability of lapse rates and identify potential regional patterns. It is also useful to investigate the impacts of climate change on lapse rate patterns, and integrate the findings into regional climate and glacio-hydrological models. Additionally, exploring the potential of machine learning techniques or data-driven approaches to improve lapse rate estimation and temperature distribution modeling in complex mountainous environments by incorporating multiple models and accounting for non-linear relationships could be beneficial.

The approach of employing a well-constrained physically based energy balance model discussed in Chapter 4 and 5 demonstrates its ability to realistically simulate the distributed surface energy and mass balance of glaciers in the western Himalaya. Since the model output corresponded well with the field measurements for contrasting meteorological years, it supports the robustness of the model for its extended application for other Himalayan glaciers. The study also revealed that sensitivity of glacier mass balance for precipitation partitioning (snow-to-rain) to changes in air temperature is low in western Himalaya. Although the model study suggests that Chandra Basin glaciers receives most of its precipitation during winters, any future change in Indian Summer Monsoon (ISM) and Western Disturbances (WD) in a changing climate scenario can adversely impact the precipitation amount/phase and glacier mass balance in the region.

The accuracy of the distributed surface energy and mass balance model simulation shown in Chapter 5 depends heavily on the quality of input data such as meteorological observations, DEM and initial conditions, because errors in the input data can propagate through the model and affect the simulation results and influence model performance, particularly in regions with complex terrain and microclimates. The model employs various parameterizations to represent complex physical processes, including turbulent heat fluxes, radiation exchanges, precipitation partitioning and albedo parameterizations amongst others. However, these parameterizations may not accurately capture the full complexity of the processes involved, especially under extreme and/or rapidly changing conditions, localized melting and precipitation redistribution due to blowing snow. Also, the parametrization may not hold true for glaciers in diverse Himalayan regions. Therefore, validating and calibrating the model parametrization against field observations or other reference data in different basins is crucial. Moreover, the model often assumes stationary conditions, neglecting long-term changes or trends in climate and varying topographical settings, which could lead to discrepancies between simulations and reality in rapidly changing climate.

6.4.2 Limitations of the study

The present study is limited in extent and restricted to a basin in western Himalaya, which is primarily influenced by the WD. Compared to this, the central and eastern Himalayan regions receive a significant amount of their precipitation from the ISM. Consequently, the glacier behavior and sensitivity to air temperature and precipitation partitioning (snow-to-rain conversion) may differ across these regions. Future studies need to examine representative sub-basins from the central and eastern Himalayan basins, for a reliable understanding of the regional variations in glacier response to climatic factors. Since future projection studies indicated increasing temperature and decreasing solid precipitation (Lutz et al. 2014; Panday et al. 2015; Sanjay et al. 2017; IPCC-SR 2019; Sabin et al. 2020), it is essential to extend the energy and mass balance studies across the Himalayan region to understand how these climatic shifts will impact glacier behavior and mass balance.

Most importantly, the current model approach and its parameterizations are limited to debris-free glaciers. However, about 13% of the glacierized area and ∼40% of the ablation area is debris-covered in Hindu Kush Himalaya (Bolch et al., 2012). The debris cover significantly influences the ablation rates and melt patterns of glaciers by altering the surface energy balance through its insulating and radiative properties (Brock et al. 2010; Reid et al. 2012; Lejeune et al. 2013; Steiner and Pellicciotti 2016; Azam and Srivastava 2020; Potter et al. 2021). Therefore, incorporating debris cover into the physically based models is a crucial step towards enhancing its applicability and accuracy in simulating the surface energy and mass balance dynamics of glaciers across the Himalaya. Future model development should focus on implementing a robust debris cover module that accounts for the spatially and temporally varying debris thickness, as well as the thermal and radiative properties of the debris layer. Furthermore, such model needs to be calibrated and validated against field observations and remote sensing data from debris-covered glaciers, ensuring that the parameterizations accurately represent the unique processes governing the energy and mass balance of these glaciers. Particular attention should be given to the albedo parameterizations, as the presence of debris can significantly alter the surface reflectivity and energy absorption. By addressing the challenges associated with debris cover, the enhanced energy and mass balance model can contribute to a better understanding of the evolving dynamics of debris-covered glaciers in the Himalayan region.

References

Aizen V. B., Aizen E. M. and Nikitin S. A. (2002) Glacier regime on the northern slope of the Himalaya (Xixibangma glaciers). *Quaternary International* 97-8, 27-39. https://doi.org/10.1016/s1040-6182(02)00049-6.

Anderson E. A. (1973) National weather service river forecast system/snow accumulation and ablation model. *NOAA, Technical Memorandum NWS HYDRO-17. Silver Spring, MD: US Department of Commerce, 217 pp*. https://doi.org/https://repository.library.noaa.gov/view/noaa/13507.

Arndt A., Scherer D. and Schneider C. (2021) Atmosphere Driven Mass-Balance Sensitivity of Halji Glacier, Himalayas. *Atmosphere* 12(4), 426.

Arndt A. and Schneider C. (2023) Spatial pattern of glacier mass balance sensitivity to atmospheric forcing in High Mountain Asia. *Journal of Glaciology*. https://doi.org/10.1017/jog.2023.46.

Azam, Ramanathan A., Wagnon P., Vincent C., Linda A., Berthier E., Sharma P., Mandal A., Angchuk T., Singh V. B. and Pottakkal J. G. (2016) Meteorological conditions, seasonal and annual mass balances of Chhota Shigri Glacier, western Himalaya, India. *Annals of Glaciology* 57(71), 328-338. https://doi.org/10.3189/2016AoG71A570.

Azam M., Wagnon P, Berthier E, Vincent C, Fujita K and JS K. (2018) Review of the status and mass changes of Himalayan-Karakoram glaciers. *Journal of Glaciology* 64(243), 61-74. https://doi.org/10.1017/jog.2017.86.

Azam M. F., Kargel J. S., Shea J. M., Nepal S., Haritashya U. K., Srivastava S., Maussion F., Qazi N., Chevallier P., Dimri A. P., Kulkarni A. V., Cogley J. G. and Bahuguna I. (2021) Glaciohydrology of the Himalaya-Karakoram. *Science* 373(6557), 869-+. https://doi.org/10.1126/science.abf3668.

Azam M. F., Ramanathan A, Wagnon P, Vincent C, Linda A, Berthier E, Sharma P, Mandal A, Angchuk T, Singh VB and GP P. (2016) Meteorological conditions, seasonal and annual mass balances of Chhota Shigri Glacier, western Himalaya, India. *Annals of Glaciology* 57(71), 328-338. https://doi.org/10.3189/2016AoG71A570.

Azam M. F. and Srivastava S. (2020) Mass balance and runoff modelling of partially debris-covered Dokriani Glacier in monsoon-dominated Himalaya using ERA5 data since 1979. *Journal of Hydrology* 590, 125432. https://doi.org/https://doi.org/10.1016/j.jhydrol.2020.125432.

Azam M. F., Wagnon P., Berthier E., Vincent C., Fujita K. and Kargel J. S. (2018) Review of the status and mass changes of Himalayan-Karakoram glaciers. *Journal of Glaciology* 64(243), 61-74. https://doi.org/10.1017/jog.2017.86.

Azam M. F., Wagnon P., Ramanathan A., Vinicent C., Sharma P., Arnaud Y., Linda A., Pottakkal J. G., Chevallier P., Singh V. B. and Berthier E. (2012) From balance to imbalance: a shift in the dynamic behaviour of Chhota Shigri glacier, western Himalaya, India. *Journal of Glaciology* 58(208), 315-324. https://doi.org/10.3189/2012JoG11J123.

Azam M. F., Wagnon P., Vincent C., Ramanathan A., Favier V., Mandal A. and Pottakkal J. G. (2014b) Processes governing the mass balance of Chhota Shigri Glacier (western Himalaya, India) assessed by point-scale surface energy balance measurements. *Cryosphere* 8(6), 2195-2217. https://doi.org/10.5194/tc-8-2195-2014.

Azam M. F., Wagnon P., Vincent C., Ramanathan A., Linda A. and Singh V. B. (2014a) Reconstruction of the annual mass balance of Chhota Shigri glacier, Western Himalaya, India, since 1969. *Annals of Glaciology* 55(66), 69-80. https://doi.org/10.3189/2014AoG66A104.

Azam M. F., Wagnon P., Vincent C., Ramanathan A. L., Kumar N., Srivastava S., Pottakkal J. G. and Chevallier P. (2019) Snow and ice melt contributions in a highly glacierized catchment of Chhota Shigri Glacier (India) over the last five decades. *Journal of Hydrology* 574, 760-773. https://doi.org/10.1016/j.jhydrol.2019.04.075.

Azam M. F. R., A., Wagnon P., Vincent C., Linda A., Berthier E., Sharma P., Mandal A., Angchuk T., Singh V. B. and Pottakkal J. G. (2016) Meteorological conditions, seasonal and annual mass balances of Chhota Shigri Glacier, western Himalaya, India. *Annals of Glaciology* 57(71), 328-338. https://doi.org/10.3189/2016AoG71A570.

Bamber J. L. and Rivera A. (2007) A review of remote sensing methods for glacier mass balance determination. *Global and Planetary Change* 59(1-4), 138-148. https://doi.org/10.1016/j.gloplacha.2006.11.031.

Benn D. I. and Evans D. J. A. (2010) Glaciers and glaciation. *2nd ed. London, Hodder Education*.

Bhattacharjee S., Chandra Pandey A. and Garg R. D. (2023) Long-term estimation of glacier mass balance using geospatial techniques in Western Himalayas, Ladakh, India. *Quaternary Science Advances* 12, 100118. https://doi.org/https://doi.org/10.1016/j.qsa.2023.100118.

Bhattacharya A., Mukherjee K., King O., Karmakar S., Remya S. N., Kulkarni A., Kropácek J. and Bolch T. (2023) Influence of climate and non-climatic attributes on declining glacier mass budget and surging in Alaknanda Basin and its surroundings. *Global and Planetary Change* 230. https://doi.org/10.1016/j.gloplacha.2023.104260.

Bhutiyani M. R., Kale V. S. and Pawar N. J. (2007) Long-term trends in maximum, minimum and mean annual air temperatures across the Northwestern Himalaya during the twentieth century. *Climatic Change* 85(1-2), 159-177. https://doi.org/10.1007/s10584-006-9196-1.

Biemans H., Siderius C., Lutz A. F., Nepal S., Ahmad B., Hassan T., von Bloh W., Wijngaard R. R., Wester P., Shrestha A. B. and Immerzeel W. W. (2019) Importance of snow and glacier meltwater for agriculture on the Indo-Gangetic Plain. *Nature Sustainability* 2(7), 594-601. https://doi.org/10.1038/s41893-019-0305-3.

Björnsson H., Pálsson F., Gudmundsson S., Magnússon E., Adalgeirsdóttir G., Jóhannesson T., Berthier E., Sigurdsson O. and Thorsteinsson T. (2013) Contribution of Icelandic ice caps to sea level rise: Trends and variability since the Little Ice Age. *Geophysical Research Letters* 40(8), 1546-1550. https://doi.org/10.1002/grl.50278.

Boike J., Juszak I., Lange S., Chadburn S., Burke E., Overduin P. P., Roth K., Ippisch O., Bornemann N., Stern L., Gouttevin I., Hauber E. and Westermann S. (2018) A 20-year record (1998-2017) of permafrost, active layer and meteorological conditions at a high Arctic permafrost research site (Bayelva, Spitsbergen). *Earth System Science Data* 10(1), 355-390. https://doi.org/10.5194/essd-10-355-2018.

Bolch T., Kulkarni A., Kaab A., Huggel C., Paul F., Cogley J. G., Frey H., Kargel J. S., Fujita K., Scheel M., Bajracharya S. and Stoffel M. (2012) The State and Fate of Himalayan Glaciers. *Science* 336(6079), 310-314. https://doi.org/10.1126/science.1215828.

Bookhagen B. and Burbank D. W. (2006) Topography, relief, and TRMM-derived rainfall variations along the Himalaya (vol 33, art no L08405, 2006). *Geophysical Research Letters* 33(13). https://doi.org/10.1029/2006gl026944.

Bookhagen B. and Burbank D. W. (2010) Toward a complete Himalayan hydrological budget: Spatiotemporal distribution of snowmelt and rainfall and their impact on river discharge. *Journal of Geophysical Research-Earth Surface* 115. https://doi.org/10.1029/2009jf001426.

Braithwaite R. J. (1984) Can the mass balance of a glacier be estimated from its equilibrium-line altitude. *Journal of Glaciology* 30(106), 364-368. https://doi.org/10.3189/s0022143000006237.

Braithwaite R. J. (2002) Glacier mass balance: the first 50 years of international monitoring. *Progress in Physical Geography* 26(1), 76-95. https://doi.org/10.1191/0309133302pp326ra.

Braun L. N. (1990) Modelling discharge of glacierized basins assisted by direct measurements of glacier mass balance. In.

Brock B. W., Mihalcea C., Kirkbride M. P., Diolaiuti G., Cutler M. E. J. and Smiraglia C. (2010) Meteorology and surface energy fluxes in the 2005-2007 ablation seasons at the Miage debris-covered glacier, Mont Blanc Massif, Italian Alps. *Journal of Geophysical Research-Atmospheres* 115. https://doi.org/10.1029/2009jd013224.

Brock B. W., Willis I. C. and Shaw M. J. (2006) Measurement and parameterization of aerodynamic roughness length variations at Haut Glacier d'Arolla, Switzerland. *Journal of Glaciology* 52(177), 281-297. https://doi.org/10.3189/172756506781828746.

Brohan P., Kennedy J. J., Harris I., Tett S. F. B. and Jones P. D. (2006) Uncertainty estimates in regional and global observed temperature changes: A new data set from 1850. *Journal of Geophysical Research-Atmospheres* 111(D12). https://doi.org/10.1029/2005jd006548.

Brun E., Martin E., Simon V., Gendre C. and Coleou C. (1989) An energy and mass model of snow cover suitable for operational avalanche forecasting. *Journal of Glaciology* 35(121), 333-342. https://doi.org/10.3189/s0022143000009254.

Brun F., Berthier E., Wagnon P., Kaab A. and Treichler D. (2017) A spatially resolved estimate of High Mountain Asia glacier mass balances from 2000 to 2016. *Nature Geoscience* 10(9), 668-+. https://doi.org/10.1038/ngeo2999.

Brun F., Dumont M., Wagnon P., Berthier E., Azam M. F., Shea J. M., Sirguey P., Rabatel A. and Ramanathan A. (2015) Seasonal changes in surface albedo of Himalayan glaciers from MODIS data and links with the annual mass balance. *Cryosphere* 9(1), 341-355. https://doi.org/10.5194/tc-9-341-2015.

Brun F., Wagnon P., Berthier E., Jomelli V., Maharjan S. B., Shrestha F. and Kraaijenbrink P. D. A. (2019) Heterogeneous Influence of Glacier Morphology on the Mass Balance Variability in High Mountain Asia. *Journal of Geophysical Research-Earth Surface* 124(6), 1331-1345. https://doi.org/10.1029/2018jf004838.

Chandrasekharan A. and Ramsankaran R. (2023) Reconstructing 32 years (1989-2020) of annual glacier surface mass balance in Chandra Basin, Western Himalayas, India. *Regional Environmental Change* 23(4). https://doi.org/10.1007/s10113-023-02112-4.

Che Y. J., Zhang M. J., Li Z. Q., Wei Y. Q., Nan Z. T., Li H. L., Wang S. J. and Su B. (2019) Energy balance model of mass balance and its sensitivity to meteorological variability on Urumqi River Glacier No.1 in the Chinese Tien Shan. *Scientific Reports* 9. https://doi.org/10.1038/s41598-019-50398-4.

Clarke G. K. C., Jarosch A. H., Anslow F. S., Radic V. and Menounos B. (2015) Projected deglaciation of western Canada in the twenty-first century. *Nature Geoscience* 8(5), 372-377. https://doi.org/10.1038/ngeo2407.

Cogley J. G. (2009) Geodetic and direct mass-balance measurements: comparison and joint analysis. *Annals of Glaciology* 50(50), 96-100. https://doi.org/10.3189/172756409787769744.

Cogley J. G., Hock R., Rasmussen L. A., Arendt A. A., Bauder A., Braithwaite R. J., Jansson P., Kaser G., Möller M., Nicholson L. and Zemp M. (2011) Glossary of glacier mass balance and related terms. Paris: UNESCO/IHP IHP-VII Technical Documents in Hydrology No. 86, IACS Contribution No. 2; UNESCO-IHP: Paris, France.

Cuffey K. M. and Paterson W. S. B. (2010) *The physics of glaciers*. Academic Press.

Cullen N. J. and Conway J. P. (2015) A 22 month record of surface meteorology and energy balance from the ablation zone of Brewster Glacier, New Zealand. *Journal of Glaciology* 61(229), 931-946. https://doi.org/10.3189/2015JoG15J004.

Cullen N. J., Mölg T., Kaser G., Steffen K. and Hardy D. R. (2007) Energy-balance model validation on the top of Kilimanjaro, Tanzania, using eddy covariance data. *Annals of Glaciology* 46, 227 - 233. https://doi.org/doi.org/10.3189/172756407782871224.

Cullen R. M. and Marshall S. J. (2011) Mesoscale Temperature Patterns in the Rocky Mountains and Foothills Region of Southern Alberta. *Atmosphere-Ocean* 49(3), 189-205. https://doi.org/10.1080/07055900.2011.592130.

Dai A. (2008) Temperature and pressure dependence of the rain-snow phase transition over land and ocean. *Geophysical Research Letters* 35(12). https://doi.org/10.1029/2008gl033295.

Davaze L., Rabatel A., Dufour A., Hugonnet R. and Arnaud Y. (2020) Region-Wide Annual Glacier Surface Mass Balance for the European Alps From 2000 to 2016. *Frontiers in Earth Science* 8. https://doi.org/10.3389/feart.2020.00149.

De Woul M. and Hock R. (2005) Static mass-balance sensitivity of Arctic glaciers and ice caps using a degree-day approach. In Dowdeswell J and Willis IC (eds), *Annals of Glaciology, Vol 42, 2005.* 217-224.

DeScally F. A. (1997) Deriving lapse rates of slope air temperature for meltwater runoff modeling in subtropical mountains: An example from the Punjab Himalaya, Pakistan. *Mountain Research and Development* 17(4), 353-362. https://doi.org/10.2307/3674024.

Dimri A. P., Niyogi D., Barros A. P., Ridley J., Mohanty U. C., Yasunari T. and Sikka D. R. (2015) Western Disturbances: A review. *Reviews of Geophysics* 53(2), 225-246. https://doi.org/10.1002/2014rg000460.

Ding B. H., Yang K., Qin J., Wang L., Chen Y. Y. and He X. B. (2014) The dependence of precipitation types on surface elevation and meteorological conditions and its parameterization. *Journal of Hydrology* 513, 154-163. https://doi.org/10.1016/j.jhydrol.2014.03.038.

Farinotti D., Immerzeel W. W., de Kok R. J., Quincey D. J. and Dehecq A. (2020) Manifestations and mechanisms of the Karakoram glacier Anomaly. *Nature Geoscience* 13(1), 8-+. https://doi.org/10.1038/s41561-019-0513-5.

Fator M. and Zomrawi N. (2015) Etrex Garmin GPS Receiver Accuracy Testing. *International Journal on Recent and Innovation Trends in Computing and Communication* 3(5). https://doi.org/doi.org/10.17762/ijritcc.v3i5.4328.

Fischer M., Huss M. and Hoelzle M. (2015) Surface elevation and mass changes of all Swiss glaciers 1980-2010. *Cryosphere* 9(2), 525-540. https://doi.org/10.5194/tc-9-525-2015.

Fugger S., Fyffe C. L., Fatichi S., Miles E., McCarthy M., Shaw T. E., Ding B. H., Yang W., Wagnon P., Immerzeel W., Liu Q. and Pellicciotti F. (2022) Understanding monsoon controls on the energy and mass balance of glaciers in the Central and Eastern Himalaya. *Cryosphere* 16(5), 1631-1652. https://doi.org/10.5194/tc-16-1631-2022.

Fujita K. (2008) Effect of precipitation seasonality on climatic sensitivity of glacier mass balance. *Earth and Planetary Science Letters* 276(1-2), 14-19. https://doi.org/10.1016/j.epsl.2008.08.028.

Fujita K. and Ageta Y. (2000) Effect of summer accumulation on glacier mass balance on the Tibetan Plateau revealed by mass-balance model. *Journal of Glaciology* 46(153), 244-252. https://doi.org/10.3189/172756500781832945.

Ganju A. and Gusain H. S. (2017) Six Years Observations ond Analysis of Radiation Parameters and Surface Energy Fluxes on Ice Sheet Near "Maitri" Research Station, East Antarctica. *P Indian Acad Sci* (83), 449–460.

Gardelle J., Berthier E., Arnaud Y. and Kaab A. (2013) Region-wide glacier mass balances over the Pamir-Karakoram-Himalaya during 1999-2011 (vol 7, pg 1263, 2013). *Cryosphere* 7(6), 1885-1886. https://doi.org/10.5194/tc-7-1885-2013.

Gardner A. S., Sharp M. J., Koerner R. M., Labine C., Boon S., Marshall S. J., Burgess D. O. and Lewis D. (2009) Near-Surface Temperature Lapse Rates over Arctic Glaciers and Their Implications for Temperature Downscaling. *Journal of Climate* 22(16), 4281-4298. https://doi.org/10.1175/2009jcli2845.1.

Georg W., Albin H., Georg N., Katharina S., Enrico T. and Peng Z. (2016) On the energy balance closure and net radiation in complex terrain. *Agricultural and Forest Meteorology* 226, 37-49. https://doi.org/10.1016/j.agrformet.2016.05.012.

Giesen R. H., Andreassen L. M., van den Broeke M. R. and Oerlemans J. (2009) Comparison of the meteorology and surface energy balance at Storbreen and Midtdalsbreen, two glaciers in southern Norway. *Cryosphere* 3(1), 57-74. https://doi.org/10.5194/tc-3-57-2009.

Gromke C., Manes C., Walter B., Lehning M. and Guala M. (2011) Aerodynamic Roughness Length of Fresh Snow. *Boundary-Layer Meteorology* 141(1), 21-34. https://doi.org/10.1007/s10546-011-9623-3.

Guo D. L., Pepin N., Yang K., Sun J. Q. and Li D. (2021) Local changes in snow depth dominate the evolving pattern of elevation-dependent warming on the Tibetan Plateau. *Science Bulletin* 66(11), 1146-1150. https://doi.org/10.1016/j.scib.2021.02.013.

Gurung T. R., Kayastha R. B., Fujita K., Joshi S. P., Sinisalo A. and Kirkham J. D. (2023) A long-term mass-balance reconstruction (1974-2021) and a decadal in situ mass-balance record (2011-2021) of Rikha Samba Glacier, central Himalaya. *Journal of Glaciology* 69(276), 723-736. https://doi.org/10.1017/jog.2022.93.

Harpold A. A., Kaplan M. L., Klos P. Z., Link T., McNamara J. P., Rajagopal S., Schumer R. and Steele C. M. (2017) Rain or snow: hydrologic processes, observations, prediction, and research needs. *Hydrology and Earth System Sciences* 21(1), 1-22. https://doi.org/10.5194/hess-21-1-2017.

Hayat H., Raup B., Muhammad S., Liu S. Y., Khan R., Baig S. U. and Tahir A. A. (2023) Heterogeneous mass balance of selected Glaciers in the Hindu Kush, Karakoram, and Himalaya between 2000 and 2018. *European Journal of Remote Sensing* 56(1). https://doi.org/10.1080/22797254.2023.2173086.

Hersbach H., Bell B., Berrisford P., Hirahara S., Horányi A., Muñoz-Sabater J., Nicolas J., Peubey C., Radu R., Schepers D., Simmons A., Soci C., Abdalla S., Abellan X., Balsamo G., Bechtold P., Biavati G., Bidlot J., Bonavita M., De Chiara G., Dahlgren P., Dee D., Diamantakis M., Dragani R., Flemming J., Forbes R., Fuentes M., Geer A., Haimberger L., Healy S., Hogan R. J., Hólm E., Janisková M., Keeley S., Laloyaux P., Lopez P., Lupu C., Radnoti G., de Rosnay P., Rozum I., Vamborg F., Villaume S. and Thépaut J. N. (2020) The ERA5 global reanalysis. *Quarterly Journal of the Royal Meteorological Society* 146(730), 1999-2049. https://doi.org/10.1002/qj.3803.

Heynen M., Miles E., Ragettli S., Buri P., Immerzeel W. W. and Pellicciotti F. (2016) Air temperature variability in a high-elevation Himalayan catchment. *Annals of Glaciology* 57(71), 212-222. https://doi.org/10.3189/2016AoG71A076.

Hock R. (2003) Temperature index melt modelling in mountain areas. *Journal of Hydrology* 282(1-4), 104-115. https://doi.org/10.1016/s0022-1694(03)00257-9.

Hock R. (2005) Glacier melt: a review of processes and their modelling. *Progress in Physical Geography-Earth and Environment* 29(3), 362-391. https://doi.org/10.1191/0309133305pp453ra.

Hock R., Bliss A., Marzeion B., Giesen R. H., Hirabayashi Y., Huss M., Radic V. and Slangen A. B. A. (2019) GlacierMIP - A model intercomparison of global-scale glacier mass-balance models and projections. *Journal of Glaciology* 65(251), 453-467. https://doi.org/10.1017/jog.2019.22.

Hock R. and Holmgren B. (2005) A distributed surface energy-balance model for complex topography and its application to Storglaciaren, Sweden. *Journal of Glaciology* 51(172), 25-36. https://doi.org/10.3189/172756505781829566.

Hock R., Rasul G., Adler C., Cáceres B., Gruber S., Hirabayashi and Y. e. a. (2019) IPCC Special Report on the Ocean and Cryosphere in a Changing Climate, Chap 2,in High mountain areas. (eds. Pörtner, H.-O. et al.), 131–202.

Huang S. L., Rich P. M., Crabtree R. L., Potter C. S. and Fu P. D. (2008) Modeling monthly near-surface air temperature from solar radiation and lapse rate: Application over complex terrain in Yellowstone National Park. *Physical Geography* 29(2), 158-178. https://doi.org/10.2747/0272-3646.29.2.158.

Hugonnet R., McNabb R., Berthier E., Menounos B., Nuth C., Girod L., Farinotti D., Huss M., Dussaillant I., Brun F. and Kääb A. (2021) Accelerated global glacier mass loss in the early twenty-first century. *Nature* 592(7856), 726-+. https://doi.org/10.1038/s41586-021-03436-z.

Huintjes E., Sauter T., Schroter B., Maussion F., Yang W., Kropacek J., Buchroithner M., Scherer D., Kang S. and Schneider C. (2015) Evaluation of a coupled snow and energy balance model for Zhadang glacier, Tibetan Plateau, using glaciological measurements and time-lapse photography. *Arctic Antarctic and Alpine Research* 47(3), 573-590. https://doi.org/10.1657/aaar0014-073.

Huss M. (2012) Extrapolating glacier mass balance to the mountain-range scale: the European Alps 1900-2100. *Cryosphere* 6(4), 713-727. https://doi.org/10.5194/tc-6-713-2012.

Immerzeel W. W., Lutz A. F., Andrade M., Bahl A., Biemans H., Bolch T., Hyde S., Brumby S., Davies B. J., Elmore A. C., Emmer A., Feng M., Fernández A., Haritashya U., Kargel J. S., Koppes M., Kraaijenbrink P. D. A., Kulkarni A. V., Mayewski P. A., Nepal S., Pacheco P., Painter T. H., Pellicciotti F., Rajaram H., Rupper S., Sinisalo A., Shrestha A. B., Viviroli D., Wada Y., Xiao C., Yao T. and Baillie J. E. M. (2020) Importance and vulnerability of the world's water towers. *Nature* 577(7790), 364-+. https://doi.org/10.1038/s41586-019-1822-y.

Immerzeel W. W., Petersen L., Ragettli S. and Pellicciotti F. (2014) The importance of observed gradients of air temperature and precipitation for modeling runoff from a glacierized watershed in the Nepalese Himalayas. *Water Resources Research* 50(3), 2212-2226. https://doi.org/10.1002/2013wr014506.

IPCC-SR (2019) IPCC SR ocean and cryosphere in a changing climate, Chap 2. In: Hock R et al (eds) High mountain areas. (In press.).

IPCC (2023) In: Climate Change 2023: Synthesis Report. Contribution of Working Groups I, II and III to the Sixth Assessment Report of the Intergovernmental Panel on Climate Change [Core Writing Team, H. Lee and J. Romero (eds.)]. IPCC, Geneva, Switzerland, pp. 1-34. https://doi.org/doi: 10.59327/IPCC/AR6-9789291691647.001.

Kaab A., Berthier E., Nuth C., Gardelle J. and Arnaud Y. (2012) Contrasting patterns of early twenty-first-century glacier mass change in the Himalayas. *Nature* 488(7412), 495-498. https://doi.org/10.1038/nature11324.

Kattel D. B., Yao T., Yang K., Tian L., Yang G. and Joswiak D. (2013) Temperature lapse rate in complex mountain terrain on the southern slope of the central Himalayas. *Theoretical and Applied Climatology* 113(3-4), 671-682. https://doi.org/10.1007/s00704-012-0816-6.

Kattel D. B., Yao T. D., Yang W., Gao Y. and Tian L. D. (2015) Comparison of temperature lapse rates from the northern to the southern slopes of the Himalayas. *International Journal of Climatology* 35(15), 4431-4443. https://doi.org/10.1002/joc.4297.

Kayastha R. B., Ohata T. and Ageta Y. (1999) Application of a mass-balance model to a Himalayan glacier. *Journal of Glaciology* 45(151), 559-567. https://doi.org/10.3189/s002214300000143x.

Kenzhebaev R., Barandun M., Kronenberg M., Chen Y. N., Usubaliev R. and Hoelzle M. (2017) Mass balance observations and reconstruction for Batysh Sook Glacier, Tien Shan, from 2004 to 2016. *Cold Regions Science and Technology* 135, 76-89. https://doi.org/10.1016/j.coldregions.2016.12.007.

Klok E. J. and Oerlemans J. (2002) Model study of the spatial distribution of the energy and mass balance of Morteratschgletscher, Switzerland. *Journal of Glaciology* 48(163), 505-518. https://doi.org/10.3189/172756502781831133.

Koul M. N. and Ganjoo R. K. (2010) Impact of inter- and intra-annual variation in weather parameters on mass balance and equilibrium line altitude of Naradu Glacier (Himachal Pradesh), NW Himalaya, India. 99(1), 119–139. https://doi.org/doi:10.1007/s10584-009-9660-9, 2010.

Kulkarni A., Patwardhan S., Kumar K. K., Ashok K. and Krishnan R. (2013) Projected Climate Change in the Hindu Kush-Himalayan Region By Using the High-resolution Regional Climate Model PRECIS. *Mountain Research and Development* 33(2), 142-151. https://doi.org/10.1659/mrd-journal-d-11-00131.1.

Kulkarni A. V. (1992) Mass balance of himalayan glaciers using aar and ela methods. *Journal of Glaciology* 38(128), 101-104. https://doi.org/10.3189/s0022143000009631.

Kulkarni A. V., Bahuguna I. M., Rathore B. P., Singh S. K., Randhawa S. S., Sood R. K. and Dhar S. (2007) Glacial retreat in Himalaya using Indian Remote Sensing satellite data. *Current Science* 92(1), 69-74. https://doi.org/jstor.org/stable/24096824.

Kulkarni A. V. and Karyakarte Y. (2014) Observed changes in Himalayan glaciers. *Current Science* 106(2), 237-244.

Kulkarni A. V., Shirsat T. S., Kulkarni A., Negi H. S., Bahuguna I. M. and Thamban M. (2021) State of Himalayan cryosphere and implications for water security. *Water Security* 14, 100101. https://doi.org/https://doi.org/10.1016/j.wasec.2021.100101.

Kumar A., Verma A., Gokhale A. A., Bhambri R., Misra A., Sundriyal S., Dobhal D. P. and Kishore N. (2018) Hydrometeorological assessments and suspended sediment delivery from a central Himalayan glacier in the upper Ganga basin. *International Journal of Sediment Research* 33(4), 493-509. https://doi.org/10.1016/j.ijsrc.2018.03.004.

Kumar L., Skidmore A. K. and Knowles E. (1997) Modelling topographic variation in solar radiation in a GIS environment. *International Journal of Geographical Information Science* 11(5), 475-497. https://doi.org/10.1080/136588197242266.

Kumar P., Saharwardi M. S., Banerjee A., Azam M. F. A., Dubey A. K. and Murtugudde R. (2019) Snowfall Variability Dictates Glacier Mass Balance Variability in Himalaya-Karakoram. *Scientific Reports* 9, 9. https://doi.org/10.1038/s41598-019-54553-9.

Kumar R., Singh S., Singh A., Kumar R., Singh S. and Randhawa S. S. (2021) Surface mass balance analysis at Naradu Glacier, Western Himalaya, India. *Scientific Reports* 11(1), 12710. https://doi.org/10.1038/s41598-021-91348-3.

Kumar R., Singh S., Singh A., Kumar R., Singh S. and Randhawa S. S. (2021) Surface mass balance analysis at Naradu Glacier, Western Himalaya, India. *Scientific Reports* 11(1). https://doi.org/10.1038/s41598-021-91348-3.

Laha S., Banerjee A., Singh A., Sharma P. and Thamban M. (2023) Climate sensitivity of the summer runoff of two glacierised Himalayan catchments with contrasting climate. *Hydrology and Earth System Sciences* 27(2), 627-645. https://doi.org/10.5194/hess-27-627-2023.

Li S. H., Yao T. D., Yu W. S., Yang W. and Zhu M. L. (2019) Energy and mass balance characteristics of the Guliya ice cap in the West Kunlun Mountains, Tibetan Plateau. *Cold Regions Science and Technology* 159, 71-85. https://doi.org/10.1016/j.coldregions.2018.12.001.

Li X. M., Zhang B., Ren R., Li L. H. and Simonovic S. P. (2022) Spatio-Temporal Heterogeneity of Climate Warming in the Chinese Tianshan Mountainous Region. *Water* 14(2). https://doi.org/10.3390/w14020199.

Li X. P., Wang L., Chen D. L., Yang K., Xue B. L. and Sun L. T. (2013) Near-surface air temperature lapse rates in the mainland China during 1962-2011. *Journal of Geophysical Research-Atmospheres* 118(14), 7505-7515. https://doi.org/10.1002/jgrd.50553.

Li X. Y., Long D., Scanlon B. R., Mann M. E., Li X. D., Tian F. Q., Sun Z. L. and Wang G. Q. (2022) Climate change threatens terrestrial water storage over the Tibetan Plateau. *Nature Climate Change* 12(9), 801-+. https://doi.org/10.1038/s41558-022-01443-0.

Lookingbill T. R. and Urban D. L. (2003) Spatial estimation of air temperature differences for landscape-scale studies in montane environments. *Agricultural and Forest Meteorology* 114(3-4), 141-151. https://doi.org/10.1016/s0168-1923(02)00196-x.

Lutz A. F., Immerzeel W. W., Shrestha A. B. and Bierkens M. F. P. (2014) Consistent increase in High Asia's runoff due to increasing glacier melt and precipitation. *Nature Climate Change* 4(7), 587-592. https://doi.org/10.1038/nclimate2237.

Machguth H., Purves R. S., Oerlemans J., Hoelzle M. and Paul F. (2008) Exploring uncertainty in glacier mass balance modelling with Monte Carlo simulation. *Cryosphere* 2(2), 191-204. https://doi.org/10.5194/tc-2-191-2008.

Mandal A., Ramanathan A., Azam M. F., Angchuk T., Soheb M., Kumar N., Pottakkal J. G., Vatsal S., Mishra S. and Singh V. B. (2020) Understanding the interrelationships among mass balance, meteorology, discharge and surface velocity on Chhota Shigri Glacier over 2002-2019 using in situ measurements. *Journal of Glaciology* 66(259), 727-741. https://doi.org/10.1017/jog.2020.42.

Marshall S. J. (2014) Meltwater run-off from Haig Glacier, Canadian Rocky Mountains, 2002-2013. *Hydrology and Earth System Sciences* 18(12), 5181-5200. https://doi.org/10.5194/hess-18-5181-2014.

Marshall S. J., Sharp M. J., Burgess D. O. and Anslow F. S. (2007) Near-surface-temperature lapse rates on the Prince of Wales Icefield, Ellesmere Island, Canada: implications for regional downscaling of temperature. *International Journal of Climatology* 27(3), 385-398. https://doi.org/10.1002/joc.1396.

Maurer J. M., Schaefer J. M., Rupper S. and Corley A. (2019) Acceleration of ice loss across the Himalayas over the past 40 years. *Science Advances* 5(6). https://doi.org/10.1126/sciadv.aav7266.

Maussion F., Scherer D., Mölg T., Collier E., Curio J. and Finkelnburg R. (2014) Precipitation Seasonality and Variability over the Tibetan Plateau as Resolved by the High Asia Reanalysis. *Journal of Climate* 27(5), 1910-1927. https://doi.org/10.1175/jcli-d-13-00282.1.

Mayewski P. A., Perry L. B., Matthews T. and Birkel S. D. (2020) Climate Change in the Hindu Kush Himalayas: Basis and Gaps. *One Earth* 3(5), 551-555. https://doi.org/10.1016/j.oneear.2020.10.007.

Meier M. F., Dyurgerov M. B., Rick U. K., O'Neel S., Pfeffer W. T., Anderson R. S., Anderson S. P. and Glazovsky A. F. (2007) Glaciers dominate Eustatic sea-level rise in the 21st century. *Science* 317(5841), 1064-1067. https://doi.org/10.1126/science.1143906.

Mihalcea C., Brock B. W., Diolaiuti G., D'Agata C., Citterio M., Kirkbride M. P., Cutler M. E. J. and Smiraglia C. (2008) Using ASTER satellite and ground-based surface temperature measurements to derive supraglacial debris cover and thickness patterns on Miage Glacier (Mont Blanc Massif, Italy). *Cold Regions Science and Technology* 52(3), 341-354. https://doi.org/10.1016/j.coldregions.2007.03.004.

Miles E., McCarthy M., Dehecq A., Kneib M., Fugger S. and Pellicciotti F. (2021) Health and sustainability of glaciers in High Mountain Asia. *Nature Communications* 12(1). https://doi.org/10.1038/s41467-021-23073-4.

Miles E. S., Willis I., Buri P., Steiner J. F., Arnold N. S. and Pellicciotti F. (2018) Surface Pond Energy Absorption Across Four Himalayan Glaciers Accounts for 1/8 of Total Catchment Ice Loss. *Geophysical Research Letters* 45(19), 10464-10473. https://doi.org/10.1029/2018gl079678.

Minder J. R., Mote P. W. and Lundquist J. D. (2010) Surface temperature lapse rates over complex terrain: Lessons from the Cascade Mountains. *Journal of Geophysical Research-Atmospheres* 115. https://doi.org/10.1029/2009jd013493.

Mishra R., Kumar A. and Singh D. (2014) Long term monitoring of mass balance of Hamtah Glacier, Lahaul and Spiti district, Himachal Pradesh. *Geolo Surv India* (147(pt 8):230–231).

Molg T., Cullen N. J., Hardy D. R., Winkler M. and Kaser G. (2009) Quantifying Climate Change in the Tropical Midtroposphere over East Africa from Glacier Shrinkage on Kilimanjaro. *Journal of Climate* 22(15), 4162-4181. https://doi.org/10.1175/2009jcli2954.1.

Molg T. and Scherer D. (2012) Retrieving important mass-balance model parameters from AWS measurements and high-resolution mesoscale atmospheric modeling. *Journal of Glaciology* 58(209), 625-628. https://doi.org/10.3189/2012JoG11J258.

Morice C. P., Kennedy J. J., Rayner N. A., Winn J. P., Hogan E., Killick R. E., Dunn R. J. H., Osborn T. J., Jones P. D. and Simpson I. R. (2021) An Updated Assessment of Near-Surface Temperature Change From 1850: The HadCRUT5 Data Set.

Journal of Geophysical Research-Atmospheres 126(3). https://doi.org/10.1029/2019jd032361.

Mukherjee K., Bhattacharya A., Pieczonka T., Ghosh S. and Bolch T. (2018) Glacier mass budget and climate reanalysis data indicate a climatic shift around 2000 in Lahaul-Spiti, western Himalaya. *Climatic Change* 148(1-2), 219-233. https://doi.org/10.1007/s10584-018-2185-3.

Nair V. S., Usha K. H. and S. Suresh Babu (2023) Elevation-dependence of warming due to aerosol-induced snow darkening over the Himalayan-Tibetan region. *Environmental Research Letters* 19. https://doi.org/doi.org/10.1088/1748-9326/ad1346.

Negi H. S., Kanda N., Shekhar M. S. and Ganju A. (2018) Recent wintertime climatic variability over the North West Himalayan cryosphere. *Current Science* 114(4), 760-770. https://doi.org/10.18520/cs/v114/i04/760-770.

Nigrelli G., Fratianni S., Zampollo A., Turconi L. and Chiarle M. (2018) The altitudinal temperature lapse rates applied to high elevation rockfalls studies in the Western European Alps. *Theoretical and Applied Climatology* 131(3-4), 1479-1491. https://doi.org/10.1007/s00704-017-2066-0.

Oerlemans J. (2000) Analysis of a 3 year meteorological record from the ablation zone of Morteratschgletscher, Switzerland: energy and mass balance. *Journal of Glaciology* 46(155), 571-579. https://doi.org/10.3189/172756500781832657.

Oerlemans J. (2001) Glaciers and Climate Change. Lisse: Swets & Zeitlinger. 148 pp.

Oerlemans J. (2005) Extracting a climate signal from 169 glacier records. *Science* 308(5722), 675-677. https://doi.org/10.1126/science.1107046.

Oerlemans J. and Knap W. H. (1998) A 1 year record of global radiation and albedo in the ablation zone of Morteratschgletscher, Switzerland. *Journal of Glaciology* 44(147), 231-238. https://doi.org/10.3189/s0022143000002574.

Oerlemans J. and Reichert B. K. (2000) Relating glacier mass balance to meteorological data by using a seasonal sensitivity characteristic. *Journal of Glaciology* 46(152), 1-6. https://doi.org/10.3189/172756500781833269.

Olson M. and Rupper S. (2019) Impacts of topographic shading on direct solar radiation for valley glaciers in complex topography. *Cryosphere* 13(1), 29-40. https://doi.org/10.5194/tc-13-29-2019.

Østrem G. and Brugman M. (1991) Glacier mass-balance measurements. A manual for field and office work. (NHRI Science Report 4) National Hydrology Research Institute, Environment Canada, Saskatoon, Sask.

Østrem G. and Stanley A. (1966) Glacier mass-balance measurements: A manual for field of work; Canadian Department of Energy, Mines and Resources: Ottawa, ON, Canada, . 66.

Oulkar S. N., Thamban M., Sharma P., Pratap B., Singh A. T., Patel L. K., Pramanik A. and Ravichandran M. (2022) Energy fluxes, mass balance, and climate sensitivity of the Sutri Dhaka Glacier in the western Himalaya. *Frontiers in Earth Science* 10. https://doi.org/10.3389/feart.2022.949735.

Palazzi E., Mortarini L., Terzago S. and von Hardenberg J. (2019) Elevation-dependent warming in global climate model simulations at high spatial resolution. *Climate Dynamics* 52(5-6), 2685-2702. https://doi.org/10.1007/s00382-018-4287-z.

Panday P. K., Thibeault J. and Frey K. E. (2015) Changing temperature and precipitation extremes in the Hindu Kush-Himalayan region: an analysis of CMIP3 and CMIP5 simulations and projections. *International Journal of Climatology* 35(10), 3058-3077. https://doi.org/10.1002/joc.4192.

Patel A., Goswami A., Dharpure J. K., Thamban M., Sharma P., Kulkarni A. V. and Oulkar S. (2021) Estimation of mass and energy balance of glaciers using a distributed energy balance model over the Chandra river basin (Western Himalaya). *Hydrological Processes*. https://doi.org/DOI: 10.1002/hyp.14058.

Pellicciotti F., Carenzo M., Helbing J., Rimkus S. and Burlando P. (2009) On the role of subsurface heat conduction in glacier energy-balance modelling. *Annals of Glaciology* 50(50), 16-24. https://doi.org/10.3189/172756409787769555.

Pellicciotti F., Helbing J., Rivera A., Favier V., Corripio J., Araos J., Sicart J. E. and Carenzo M. (2008) A study of the energy balance and melt regime on Juncal Norte Glacier, semi-arid Andes of central Chile, using melt models of different complexity. *Hydrological Processes* 22(19), 3980-3997. https://doi.org/10.1002/hyp.7085.

Pellicciotti F., Stephan C., Miles E., Herreid S., Immerzeel W. W. and Bolch T. (2015) Mass-balance changes of the debris-covered glaciers in the Langtang Himal, Nepal, from 1974 to 1999. *Journal of Glaciology* 61(226), 373-386. https://doi.org/10.3189/2015JoG13J237.

Pepin N., Bradley R. S., Diaz H. F., Baraer M., Caceres E. B., Forsythe N., Fowler H., Greenwood G., Hashmi M. Z., Liu X. D., Miller J. R., Ning L., Ohmura A., Palazzi E., Rangwala I., Schöner W., Severskiy I., Shahgedanova M., Wang M. B., Williamson S. N., Yang D. Q. and Mt Res Initiative E. D. W. W. G. (2015) Elevation-dependent warming in mountain regions of the world. *Nature Climate Change* 5(5), 424-430. https://doi.org/10.1038/nclimate2563.

Pepin N. C., Arnone E., Gobiet A., Haslinger K., Kotlarski S., Notarnicola C., Palazzi E., Seibert P., Serafin S., Schöner W., Terzago S., Thornton J. M., Vuille M. and Adler C. (2022) Climate Changes and Their Elevational Patterns in the Mountains of the World. *Reviews of Geophysics* 60(1). https://doi.org/10.1029/2020rg000730.

Petersen L. and Pellicciotti F. (2011) Spatial and temporal variability of air temperature on a melting glacier: Atmospheric controls, extrapolation methods and their effect on melt modeling, Juncal Norte Glacier, Chile. *Journal of Geophysical Research-Atmospheres* 116. https://doi.org/10.1029/2011jd015842.

Philippe B., Michael H. and Cameron A. P. (2021) Synoptic processes of winter precipitation in the Upper Indus Basin. *Weather and Climate Dynamics* 2, 1187–1207. https://doi.org/doi.org/10.5194/wcd-2-1187-2021.

Pratap B., Dobhal D. P., Bhambri R. and Mehta M. (2013) Near-surface temperature lapse rate in Dokriani Glacier catchment, Garhwal Himalaya, India. *Himalayan Geology* 34(2), 183-186.

Pratap B., Dobhal D. P., Bhambri R., Mehta M. and Tewari V. C. (2016) Four decades of glacier mass balance observations in the Indian Himalaya. *Regional Environmental Change* 16(3), 643-658. https://doi.org/10.1007/s10113-015-0791-4.

Pratap B., Sharma P., Patel L., Singh A. T., Gaddam V. K., Oulkar S. and Thamban M. (2019a) Reconciling High Glacier Surface Melting in Summer with Air Temperature in the Semi-Arid Zone of Western Himalaya. *Water* 11(8). https://doi.org/10.3390/w11081561.

Pratap B., Sharma P., Patel L. K., Singh A. T., Gaddam V. K., Oulkar S. and Thamban M. (2019b) Reconciling High Glacier Surface Melting in Summer with Air Temperature in the Semi-Arid Zone of Western Himalaya. *Water* 11(8). https://doi.org/10.3390/w11081561.

Pratap B., Sharma P., Patel L. K., Singh A. T., Oulkar S. N. and Thamban M. (2023) Differential surface melting of a debris-covered glacier and its geomorphological control - A case study from Batal Glacier, western Himalaya. *Geomorphology* 431. https://doi.org/10.1016/j.geomorph.2023.108686.

Pritchard H. D. (2019) Asia's shrinking glaciers protect large populations from drought stress. *Nature* 569(7758), 649-+. https://doi.org/10.1038/s41586-019-1240-1.

Qu B., Ming J., Kang S. C., Zhang G. S., Li Y. W., Li C. D., Zhao S. Y., Ji Z. M. and Cao J. J. (2014) The decreasing albedo of the Zhadang glacier on western Nyainqentanglha and the role of light-absorbing impurities. *Atmospheric Chemistry and Physics* 14(20), 11117-11128. https://doi.org/10.5194/acp-14-11117-2014.

Rabatel A., Dedieu J. P. and Vincent C. (2016) Spatio-temporal changes in glacier-wide mass balance quantified, by optical remote sensing on 30 glaciers in the French Alps for the period 1983-2014. *Journal of Glaciology* 62(236), 1153-1166. https://doi.org/10.1017/jog.2016.113.

Racoviteanu A. E., Arnaud Y., Williams M. W. and Manley W. F. (2015) Spatial patterns in glacier characteristics and area changes from 1962 to 2006 in the Kanchenjunga-Sikkim area, eastern Himalaya. *Cryosphere* 9(2), 505-523. https://doi.org/10.5194/tc-9-505-2015.

Radic V., Bliss A., Beedlow A. C., Hock R., Miles E. and Cogley J. G. (2014) Regional and global projections of twenty-first century glacier mass changes in response to climate scenarios from global climate models. *Climate Dynamics* 42(1-2), 37-58. https://doi.org/10.1007/s00382-013-1719-7.

Raman A., Kulkarni A. V. and Prasad V. (2022) Glacier mass balance estimation in Garhwal Himalaya using improved accumulation area ratio method. *Environmental Monitoring and Assessment* 194(8). https://doi.org/10.1007/s10661-022-10261-y.

Rasul G. and Molden D. (2019) The Global Social and Economic Consequences of Mountain Cryospheric Change. *Frontiers in Environmental Science* 7. https://doi.org/10.3389/fenvs.2019.00091.

Ravindra R., Kulkarni A. V., Dimri A. P., Sain K., Sharma M. C., Banerjee A., Sharma P., Meloth T., Rashid I. and Pant N. C. (2024) Recent Indian studies in Himalayan cryosphere. *Proceedings of the Indian National Science Academy*. https://doi.org/10.1007/s43538-024-00237-6.

Reid T. D., Carenzo M., Pellicciotti F. and Brock B. W. (2012) Including debris cover effects in a distributed model of glacier ablation. *Journal of Geophysical Research-Atmospheres* 117. https://doi.org/10.1029/2012jd017795.

Reijmer C. H. and Oerlemans J. (2002) Temporal and spatial variability of the surface energy balance in Dronning Maud Land, East Antarctica. *Journal of Geophysical Research-Atmospheres* 107(D24). https://doi.org/10.1029/2000jd000110.

Reijmer C. H., van den Broeke M. R., Fettweis X., Ettema J. and Stap L. B. (2012) Refreezing on the Greenland ice sheet: a comparison of parameterizations. *Cryosphere* 6(4), 743-762. https://doi.org/10.5194/tc-6-743-2012.

RGI6.0 (2017) RGI Consortium, 2017. Randolph Glacier Inventory - A Dataset of Global Glacier Outlines, Version 6. [Indicate subset used]. Boulder, Colorado USA. NSIDC: National Snow and Ice Data Center. https://doi.org/https://doi.org/10.7265/4m1f-gd79.

Richard C. and Gratton D. J. (2001) The importance of the air temperature variable for the snowmelt runoff modelling using the SRM. *Hydrological Processes* 15(18), 3357-3370. https://doi.org/10.1002/hyp.1031.

Rolland C. (2003) Spatial and seasonal variations of air temperature lapse rates in Alpine regions. *Journal of Climate* 16(7), 1032-1046. https://doi.org/doi.org/10.1175/1520-0442(2003)016<1032:SASVOA>2.0.CO;2.

Ruelland D. (2020) Should altitudinal gradients of temperature and precipitation inputs be inferred from key parameters in snow-hydrological models? *Hydrology and Earth System Sciences* 24(5), 2609-2632. https://doi.org/10.5194/hess-24-2609-2020.

Sabin T. P., Krishnan R., Vellore R., Priya P., Borgaonkar H. P., Singh B. B. and Sagar A. (2020) Climate Change Over the Himalayas. In Krishnan R, Sanjay J, Gnanaseelan C, Mujumdar M, Kulkarni A and Chakraborty S (eds), *Assessment of Climate Change over the Indian Region: A Report of the Ministry of Earth Sciences (MoES), Government of India.* Singapore: Springer Singapore, 207-222.

Sakai A. and Fujita K. (2017) Contrasting glacier responses to recent climate change in high-mountain Asia. *Scientific Reports* 7, 8. https://doi.org/10.1038/s41598-017-14256-5.

Sanjay J., Krishnan R., Shrestha A. B., Rajbhandari R. and Ren G. Y. (2017) Downscaled climate change projections for the Hindu Kush Himalayan region using CORDEX South Asia regional climate models. *Advances in Climate Change Research* 8(3), 185-198. https://doi.org/10.1016/j.accre.2017.08.003.

Sauter T., Arndt A. and Schneider C. (2020) COSIPY v1.3-an open-source coupled snowpack and ice surface energy and mass balance model. *Geoscientific Model Development* 13(11), 5645-5662. https://doi.org/10.5194/gmd-13-5645-2020.

Sharma P., Patel L. K., Ravindra R., Singh A., Mahalinganathan K. and Thamban M. (2016) Role of debris cover to control specific ablation of adjoining Batal and Sutri Dhaka glaciers in Chandra Basin (Himachal Pradesh) during peak ablation season. *Journal of Earth System Science* 125(3), 459-473.

Sharma P., Patel L. K., Singh A. T., Meloth T. and Ravindra R. (2020) Glacier response to climate in Arctic and Himalaya during last seventeen years: A case study of Svalbard, Arctic and Chandra Basin, Himalaya. *In P. S. Goel, R. Ravindra, & S. Chattopadhyay (Eds.), Climate change and the white world (Springer)*, pp. 139–156.

Shean D. E., Bhushan S., Montesano P., Rounce D. R., Arendt A. and Osmanoglu B. (2020) A Systematic, Regional Assessment of High Mountain Asia Glacier Mass Balance. *Frontiers in Earth Science* 7. https://doi.org/10.3389/feart.2019.00363.

Shekhar M. S., Chand H., Kumar S., Srinivasan K. and Ganju A. (2010) Climate-change studies in the western Himalaya. *Annals of Glaciology* 51(54), 105-112. https://doi.org/10.3189/172756410791386508.

Shen Y. J., Shen Y. J., Goetz J. and Brenning A. (2016) Spatial-temporal variation of near-surface temperature lapse rates over the Tianshan Mountains, central Asia. *Journal of Geophysical Research-Atmospheres* 121(23), 14006-14017. https://doi.org/10.1002/2016jd025711.

Sheridan P., Smith S., Brown A. and Vosper S. (2010) A simple height-based correction for temperature downscaling in complex terrain. *Meteorological Applications* 17(3), 329-339. https://doi.org/10.1002/met.177.

Singh N., Singhal M., Chhikara S., Karakoti I., Chauhan P. and Dobhal D. P. (2018) Radiation and energy balance dynamics over a rapidly receding glacier in the central Himalaya. *International Journal of Climatology*, 21. https://doi.org/10.1002/joc.6218.

Singh S., Kumar R. and Dimri A. P. (2018) Mass Balance Status of Indian Himalayan Glaciers: A Brief Review. *Frontiers in Environmental Science* 6. https://doi.org/10.3389/fenvs.2018.00030.

Singh V., Jain S. K. and Nagale D. S. (2023) A comparative analysis of glacier and glacier-melt runoff changes in western and eastern Himalayan river basins. *Cold*

Regions Science and Technology 214. https://doi.org/10.1016/j.coldregions.2023.103965.

Soheb M., Ramanathan A., Angchuk T., Mandal A., Kumar N. and Lotus S. (2020) Mass-balance observation, reconstruction and sensitivity of Stok glacier, Ladakh region, India, between 1978 and 2019. *Journal of Glaciology* 66(258), 627-642. https://doi.org/10.1017/jog.2020.34.

Song W. Y., Tang H. D., Sun X. Y., Xiang Y. X., Ma X. F. and Zhang H. B. (2022) Developing a New Parameterization Scheme of Temperature Lapse Rate for the Hydrological Simulation in a Glacierized Basin Based on Remote Sensing. *Remote Sensing* 14(19). https://doi.org/10.3390/rs14194973.

Steiner J. F. and Pellicciotti F. (2016) Variability of air temperature over a debris-covered glacier in the Nepalese Himalaya. *Annals of Glaciology* 57(71), 295-307. https://doi.org/10.3189/2016AoG71A066.

Stiegler C., Johansson M., Christensen T. R., Mastepanov M. and Lindroth A. (2016) Tundra permafrost thaw causes significant shifts in energy partitioning. *Tellus Series B-Chemical and Physical Meteorology* 68. https://doi.org/10.3402/tellusb.v68.30467.

Sun C. J., Chen W. and Shen Y. J. (2022) Unraveling the distribution patterns of near-surface temperature lapse rates in the Northwestern Kunlun Mountains. *Journal of Mountain Science* 19(4), 1168-1181. https://doi.org/10.1007/s11629-021-6983-0.

Sun W. J., Qin X., Du W. T., Liu W. G., Liu Y. S., Zhang T., Xu Y. T., Zha Q. D., Wu J. K. and Ren J. W. (2014) Ablation modeling and surface energy budget in the ablation zone of Laohugou glacier No. 12, western Qilian mountains, China. *Annals of Glaciology* 55(66), 111-120. https://doi.org/10.3189/2014AoG66A902.

Sun W. J., Qin X., Wang Y. T., Chen J. Z., Du W. T., Zhang T. and Huai B. J. (2018) The response of surface mass and energy balance of a continental glacier to climate variability, western Qilian Mountains, China. *Climate Dynamics* 50(9-10), 3557-3570. https://doi.org/10.1007/s00382-017-3823-6.

Sunako S., Fujita K., Sakai A. and Kayastha R. B. (2019) Mass balance of Trambau Glacier, Rolwaling region, Nepal Himalaya: in-situ observations, long-term reconstruction and mass-balance sensitivity. *Journal of Glaciology* 65(252), 605-616. https://doi.org/10.1017/jog.2019.37.

Tachikawa T. (2011) Characteristics of ASTER GDEM version 2 International geoscience and remote sensing symposium (IGARSS).

Tak S. and Keshari A. K. (2020) Investigating mass balance of Parvati glacier in Himalaya using satellite imagery based model. *Scientific Reports* 10(1), 12211. https://doi.org/10.1038/s41598-020-69203-8.

Tawde S. A., Kulkarni A. V. and Bala G. (2017) An estimate of glacier mass balance for the Chandra basin, western Himalaya, for the period 1984-2012. *Annals of Glaciology* 58(75), 99-109. https://doi.org/10.1017/aog.2017.18.

Thibert E., Blanc R., Vincent C. and Eckert N. (2008) Glaciological and volumetric mass-balance measurements: error analysis over 51 years for Glacier de Sarennes, French Alps. *Journal of Glaciology* 54(186), 522-532. https://doi.org/10.3189/002214308785837093.

Van den Broeke M., Reijmer C., Van As D. and Boot W. (2006) Daily cycle of the surface energy balance in Antarctica and the influence of clouds. *International Journal of Climatology* 26(12), 1587-1605. https://doi.org/10.1002/joc.1323.

Van den Broeke M., Reijmer C., Van As D., De Wal R. V. and Oerlemans J. (2005) Seasonal cycles of Antarctic surface energy balance from automatic weather stations. In Hamilton G (ed), *Annals of Glaciology, Vol 41, 2005.* 131-139.

van den Broeke M., Smeets P., Ettema J. and Munneke P. K. (2008) Surface radiation balance in the ablation zone of the west Greenland ice sheet. *Journal of Geophysical Research-Atmospheres* 113(D13). https://doi.org/10.1029/2007jd009283.

van der Veen C. J. (2002) Polar ice sheets and global sea level: how well can we predict the future? *Global and Planetary Change* 32(2-3), 165-194. https://doi.org/10.1016/s0921-8181(01)00140-0.

Vijay S. and Braun M. (2016) Elevation Change Rates of Glaciers in the Lahaul-Spiti (Western Himalaya, India) during 2000-2012 and 2012-2013. *Remote Sensing* 8(12). https://doi.org/10.3390/rs8121038.

Vincent C., Ramanathan A., Wagnon P., Dobhal D. P., Linda A., Berthier E., Sharma P., Arnaud Y., Azam M. F., Jose P. G. and Gardelle J. (2013) Balanced conditions or slight mass gain of glaciers in the Lahaul and Spiti region (northern India, Himalaya) during the nineties preceded recent mass loss. *Cryosphere* 7(2), 569-582. https://doi.org/10.5194/tc-7-569-2013.

Vishwakarma B. D., Ramsankaran R. A. A. J., Azam M., Bolch T., Mandal A., Srivastava S. and al. e. (2022) Challenges in understanding the variability of the cryosphere in the Himalaya and its impact on regional water resources. *Frontiers in Water* 4. https://doi.org/https://doi.org/10.3389/frwa.2022.909246.

Wagnon P., Vincent C., Arnaud Y., Berthier E., Vuillermoz E., Gruber S., Menegoz M., Gilbert A., Dumont M., Shea J. M., Stumm D. and Pokhrel B. K. (2013) Seasonal and annual mass balances of Mera and Pokalde glaciers (Nepal Himalaya) since 2007. *Cryosphere* 7(6), 1769-1786. https://doi.org/10.5194/tc-7-1769-2013.

Wang R. J., Ding Y. J., Shangguan D. H., Guo W. Q., Zhao Q. D., Li Y. J. and Song M. (2022) Influence of Topographic Shading on the Mass Balance of the High Mountain Asia Glaciers. *Remote Sensing* 14(7). https://doi.org/10.3390/rs14071576.

Wang R. J., Ding Y. J., Shangguan D. H., Liu S. Y., Guo W. Q., Han H. D., Li Y. J., Song M. and Zheng Z. Q. (2023) Spatial differences of ice volume across High Mountain Asia. *Advances in Climate Change Research* 14(4), 511-521. https://doi.org/10.1016/j.accre.2023.08.004.

Wang S. H., Liu J. T., Pritchard H. D., Ke L. H., Qiao X., Zhang J., Xiao W. H. and Zhou Y. Y. (2023) Characterizing 4 decades of accelerated glacial mass loss in the west Nyainqentanglha Range of the Tibetan Plateau. *Hydrology and Earth System Sciences* 27(4), 933-952. https://doi.org/10.5194/hess-27-933-2023.

Wang S. J., Zhang M. J., Wang B. L., Sun M. P. and Li X. F. (2013) Recent changes in daily extremes of temperature and precipitation over the western Tibetan Plateau, 1973-2011. *Quaternary International* 313, 110-117. https://doi.org/10.1016/j.quaint.2013.03.037.

Wani J. M., Thayyen R. J., Ojha C. S. P. and Gruber S. (2021) The surface energy balance in a cold and arid permafrost environment, Ladakh, Himalayas, India. *Cryosphere* 15(5), 2273-2293. https://doi.org/10.5194/tc-15-2273-2021.

WGMS (2019) Fluctuations of Glaciers Database. Zurich, Switzerland: World Glacier Monitoring Service. https://doi.org/https://doi.org/10.5904/wgms-fog-2019-12.

Whiteman C. D. (2000) Mountain Meteorology: Fundamentals and Applications. In.: Oxford University Press.

Wu X. J., He J. Q., Jiang X. and Wang N. L. (2016) Analysis of surface energy and mass balance in the accumulation zone of Qiyi Glacier, Tibetan Plateau in an ablation season. *Environmental Earth Sciences* 75(9). https://doi.org/10.1007/s12665-016-5591-8.

Xu J. C. and Grumbine R. E. (2014) Building ecosystem resilience for climate change adaptation in the Asian highlands. *Wiley Interdisciplinary Reviews-Climate Change* 5(6), 709-718. https://doi.org/10.1002/wcc.302.

Yadav J. S., Pratap B., Gupta A. K., Dobhal D. P., Yadav R. B. S. and Tiwari S. K. (2019) Spatio-temporal variability of near-surface air temperature in the Dokriani glacier catchment (DGC), central Himalaya. *Theoretical and Applied Climatology* 136(3), 1513-1532. https://doi.org/10.1007/s00704-018-2544-z.

Yang W., Guo X. F., Yao T. D., Yang K., Zhao L., Li S. H. and Zhu M. L. (2011) Summertime surface energy budget and ablation modeling in the ablation zone of a maritime Tibetan glacier. *Journal of Geophysical Research-Atmospheres* 116. https://doi.org/10.1029/2010jd015183.

Yang W., Yao T. D., Guo X. F., Zhu M. L., Li S. H. and Kattel D. B. (2013) Mass balance of a maritime glacier on the southeast Tibetan Plateau and its climatic sensitivity. *Journal of Geophysical Research-Atmospheres* 118(17), 9579-9594. https://doi.org/10.1002/jgrd.50760.

Yao T. D., Bolch T., Chen D. L., Gao J., Immerzeel W., Piao S., Su F. G., Thompson L., Wada Y., Wang L., Wang T., Wu G. J., Xu B. Q., Yang W., Zhang G. Q. and Zhao P. (2022) The imbalance of the Asian water tower. *Nature Reviews Earth & Environment* 3(10), 618-632. https://doi.org/10.1038/s43017-022-00299-4.

Yu W., Yao T., Kang S., Pu J., Yang W., Gao T., Zhao H., Zhou H., Li S., Wang W. and Ma L. (2013) Different region climate regimes and topography affect the changes in area and mass balance of glaciers on the north and south slopes of the same glacierized massif (the West Nyainqentanglha Range, Tibetan Plateau). *Journal* *of Hydrology* 495, 64-73. https://doi.org/https://doi.org/10.1016/j.jhydrol.2013.04.034.

Zeitz M., Reese R., Beckmann J., Krebs-Kanzow U. and Winkelmann R. (2021) Impact of the melt-albedo feedback on the future evolution of the Greenland Ice Sheet with PISM-dEBM-simple. *Cryosphere* 15(12), 5739-5764. https://doi.org/10.5194/tc-15-5739-2021.

Zemp M., Huss M., Thibert E., Eckert N., McNabb R., Huber J., Barandun M., Machguth H., Nussbaumer S. U., Gartner-Roer I., Thomson L., Paul F., Maussion F., Kutuzov S. and Cogley J. G. (2019) Global glacier mass changes and their contributions to sea-level rise from 1961 to 2016. *Nature* 568(7752), 382-+. https://doi.org/10.1038/s41586-019-1071-0.

Zhang G. S., Kang S. C., Fujita K., Huintjes E., Xu J. Q., Yamazaki T., Haginoya S., Wei Y., Scherer D., Schneider C. and Yao T. D. (2013) Energy and mass balance of Zhadang glacier surface, central Tibetan Plateau. *Journal of Glaciology* 59(213), 137-148. https://doi.org/10.3189/2013JoG12J152.

Zhang Z., Gu Z. N., Hu K. H., Xu Y. Y. and Zhao J. B. (2022) Spatial variability between glacier mass balance and environmental factors in the High Mountain Asia. *Journal of Arid Land* 14(4), 441-454. https://doi.org/10.1007/s40333-017-0014-z.

Zhao K. K., Peng D. Z., Gu Y., Luo X. Y., Pang B. and Zhu Z. F. (2022) Temperature lapse rate estimation and snowmelt runoff simulation in a high-altitude basin. *Scientific Reports* 12(1). https://doi.org/10.1038/s41598-022-18047-5.

Zhu M. L., Yao T. D., Yang W., Maussion F., Huintjes E. and Li S. H. (2015) Energy- and mass-balance comparison between Zhadang and Parlung No. 4 glaciers on the Tibetan Plateau. *Journal of Glaciology* 61(227), 595-607. https://doi.org/10.3189/2015JoG14J206.

Zhu M. L., Yao T. D., Yang W., Xu B. Q., Wu G. J. and Wang X. J. (2018) Differences in mass balance behavior for three glaciers from different climatic regions on the Tibetan Plateau (vol 50, pg 3457, 2018). *Climate Dynamics* 51(1-2), 769-769. https://doi.org/10.1007/s00382-017-3915-3.

List of Publications

Publications from the thesis

- **Oulkar S. N.,** Sharma P*****., Laha S., Pratap B., and Thamban M. (2024), "Temporal variability in air temperature lapse rates across the glacierised terrain of the Chandra basin, western Himalaya", *Theoretical and Applied Climatology*, https://doi.org/10.1007/s00704-024-05003-8.

- **Oulkar S. N.*,** Thamban M., Sharma P., Pratap B., Singh A. T., Patel L., Pramanik A., and Ravichandran M. (2022), "Energy fluxes, mass balance, and climate sensitivity of the Sutri Dhaka Glacier in the western Himalaya", *Frontiers in Earth Science*, https://doi.org/10.3389/feart.2022.949735.

- Patel A.*, Goswami A., Dharpure J. K., Thamban M., Sharma P., Kulkarni A. V., and **Oulkar S. N.,** (2021). "Estimation of mass and energy balance of glaciers using a distributed energy balance model over the Chandra River basin (Western Himalaya)", *Hydrological Processes*, https://doi.org/10.1002/hyp.14058.

Manuscript(s) under review

- **Oulkar S. N.,** Sharma P., Pratap B., Thamban M., Laha S., Patel L.K. and Sing A. T. "Energy and Mass Balance Modeling of Glaciers in the Upper Chandra Basin, Western Himalaya" (*Under review in Annals of Glaciology*).

Other publications

- Pratap, B., Sharma, P., Patel, L.K., Singh, A.T., **Oulkar, S.N**., and Thamban, M. (2023). Differential surface melting of a debris-covered glacier and its geomorphological control - A case study from Batal Glacier, western Himalaya. *Geomorphology*, 431, https://doi.org/10.1016/j.geomorph.2023.108686.

- Patel, L.K., Sharma, P., Singh, A.T., Pratap, B., **Oulkar, S.N.**, and Thamban, M. (2022). Spatial surface velocity pattern in the glaciers of Chandra Basin, Western Himalaya. *Geocarto International*, 37 (18): 5327-5344, https://doi.org/10.1080/10106049.2021.1920627.

- Singh, A.T., Laluraj, C.M., Sharma, P., Redkar, B.L., Patel, L.K., Pratap, B., **Oulkar, S.N.**, and Thamban, M. (2021). Hydrograph apportionment of the Chandra River draining from a semi-arid region of the Upper Indus Basin, western Himalaya. *Science of the Total Environment*, 780, https://doi.org/10.1016/j.scitotenv.2021.146500.

- Patel, L.K., Sharma, P., Singh, A., **Oulkar, S.N.**, Pratap, B., and Thamban, M. (2021). Influence of Supraglacial Debris Thickness on Thermal Resistance of the Glaciers of Chandra Basin, Western Himalaya. Frontiers in Earth Science, 9, https://doi.org/10.3389/feart.2021.706312.

- Singh, A.T., Sharma, P., Sharma, C., Laluraj, C.M., Patel, L., Pratap, B., **Oulkar, S.N.**, and Thamban, M. (2020). Water discharge and suspended sediment dynamics in the Chandra River, Western Himalaya. *Journal of Earth System Science*, 129 (1), https://doi.org/10.1007/s12040-020-01455-4.

- **Oulkar, S.N.**, Singh, D., Saha, U., and Kamra, A.K. (2019). Distribution of lightning in relation to topography and vegetation cover over the dry and moist regions in the Himalayas. *Journal of Earth System Science*, 128 (7), https://doi.org/10.1007/s12040-019-1203-9.

- Pratap, B., Sharma, P., Patel, L., Singh, A.T., Gaddam, V.K., **Oulkar, S.N.**, and Thamban, M. (2019). Reconciling High Glacier Surface Melting in Summer with Air Temperature in the Semi-Arid Zone of Western Himalaya. *Water*, 11 (8), https://doi.org/10.3390/w11081561.

Conference Presentations

- **Oulkar S. N.**, Sharma P., Pratap B., Patel L., and Thamban M., "Surface meteorological characteristics and climatology in the Chandra Basin, western Himalaya", *3rd Triennial Congress of Federation of Indian Geosciences Association on Geosciences (FIGA) of Himalaya for Sustainable Development, Wadia Institute of Himalayan Geology, Dehradun, Uttarakhand* (November 18, 2022) (**Poster presentation**).

- **Oulkar S. N.**, Sharma P., Pratap P., Patel L., Laha S. and Thamban M., "Variability of near-surface air temperature lapse rate in the glacierised catchment of the Chandra basin, western Himalaya", *Biodiversity and Climate Change (BDCC) - Sustainable Development Perspective, IIT Kharagpur, West Bengal* (February 18, 2023) (**Oral presentation**).

- **Oulkar S. N.**, Sharma P., Pratap P., Patel L., Laha S. and Thamban M., "Spatio-temporal variability of air temperature lapse rate in the glacierised catchment of the Chandra basin, western Himalaya using in-situ measurements", *European Geosciences Union (EGU) General Assembly 2023, Vienna, Austria* (April 26, 2023) (**Oral presentation**).

- **Oulkar S. N.**, Sharma P., Pratap P., Laha S., Patel L., and Thamban M., "Distributed surface energy and mass balance modeling of Chandra Basin glaciers in the semi-arid zone of Western Himalaya" *National Conference on Polar Sciences, NCPOR, Goa* (May 18, 2023) (**Poster presentation**).